Karlsruhe Institute of Technology

Optical properties of artificially generated carbon-related quantum emitters in hexagonal boron nitride

Zur Erlangung des akademischen Grades einer

Doktorin der Naturwissenschaften (Dr. rer. nat.)

von der KIT-Fakultät für Physik des
Karlsruher Instituts für Technologie (KIT)

angenommene

Dissertation

von

M.Sc. Safa Lamia Ahmed

aus Dhaka (Bangladesch)

Tag der mündlichen Prüfung: 01. August 2025
1. Referent: Prof. Dr. Wolfgang Wernsdorfer
2. Referent: Prof. Dr. David Hunger

Abstract

Hexagonal boron nitride (hBN), a two-dimensional wide-bandgap material, has emerged as a promising host for optically stable quantum emitters (QEs) suitable for quantum photonic and sensing applications. This dissertation investigates the controlled fabrication, optical characterization, and robustness of carbon-related single-photon emitters (SPE) in hBN, with an emphasis on their integration into chip-scale quantum devices.

In this work, several previously reported fabrication methods have been studied, which include focused ion beam (FIB), Reactive Ion Etching (RIE), Inductively Coupled Plasma (ICP) RIE, liquid exfoliation, and sputtered carbon. However, each method lacks one or more key attributes required for realizing an ideal, chip-integrable quantum emitter. Thus, a reproducible, contamination minimizing fabrication method is developed using atomic force microscopy (AFM) nanoindentation with diamond-like carbon-coated tips, introducing carbon impurities into the hBN lattice in a spatially controlled manner. The resulting emitters exhibit deterministic positioning and strong spectral similarity, indicating the successful and repeatable creation of a specific emitter class. Extensive photophysical analysis of over 300 emitters reveals a narrow distribution of zero-phonon lines (ZPLs), primarily in between 565 nm to 590 nm range. The emitters are attributed to carbon-trimer defects, specifically the C_2C_N configuration, supported by theoretical comparisons.

The environmental stability of these emitters is assessed through molecular deposition of $TbPc_2$, a single-molecule magnet. The emitters remain optically active and show enhanced ZPL intensity upon molecular deposition, demonstrating their robustness against external perturbation—an essential criterion for quantum sensing.

Furthermore, advanced spectroscopic techniques including photoluminescence excitation (PLE) spectroscopy and room-temperature optically detected magnetic resonance (ODMR) are employed to probe the electronic structure of the emitters. While limited spin contrast is observed under ODMR, PLE measurements reveal lifetime-limited linewidths for selected emitters, confirming their high optical quality.

This work lays the foundation for the scalable integration of hBN-based quantum emitters into hybrid quantum technologies by addressing key challenges in emitter creation, stability, and spectral purity.

Contents

List of Figures

List of Tables

1. Introduction

Using quantum emitters in hexagonal boron nitride (hBN) as sensors such as for magnetic field, electric field, temperature or strain sensing, is a promising and rapidly growing research direction that combines the robustness of two-dimensional (2D) materials with the quantum sensitivity of surface single-photon sources (SPS). hBN hosts optically stable quantum emitters at room temperature, which can detect local environmental changes—such as magnetic fields [1, 2], electric fields, strain, and temperature [3]. This positions hBN emitters as compelling candidates for nanoscale sensing applications in biology, materials science, and quantum technologies. However, this concept must compete with other well-established quantum sensors, such as nitrogen-vacancy (NV) centres in diamond, which already offer mature protocols for magnetometry and thermometry [4–7]. To make hBN-based sensing viable and competitive, several challenges need to be addressed: emitter reproducibility and control (e.g., deterministic positioning and spectral stability), integration with photonic and electronic platforms, and the development of sensing protocols that harness the emitter's spin or optical properties. Overcoming these obstacles can reveal the distinct benefits of hBN, such as its atomically thin structure, compatibility with various substrates, and capability to function in different environments, establishing it as a versatile foundation for future quantum sensing technologies.

The prospects of quantum emitters in multilayer hBN for quantum applications have garnered significant interest across multiple disciplines. As a 2D material, hBN is inherently compatible with on-chip device integration. Furthermore, optically active defects in hBN are known for their brightness and are often generated near the surface, which enhances the photon extraction and sensitivity. Some exceptionally bright emitters [8], with high quantum efficiency, have shown great promise for quantum information processing. Additionally, hBN defects typically exhibit a high zero phonon line (ZPL) to phonon sideband (PSB) ratio (i.e. a high Debye-Waller factor), making them highly suitable for quantum optical applications [9–11].

However, a big challenge in creating and controlling these color centres is that the defects are very sensitive to their environment. And since contaminants are a common hindrance while handling van der Waals hetero-structures like hBN, a reliable and clean fabrication technique is crucial to creating stable emitters that can be used for coherent control measurements as well [2]. Being a wide-bandgap semiconductor, the electronic states of the light-emitting defects in hBN are located deep within the bandgap, ensuring high stability. However, charge buildup from contaminants can introduce additional mixed states into the electronic structure of atomic light-emitting defects, potentially causing instabilities such as blinking, bleaching, and spectral diffusion [12–14].

However, with the appropriate fabrication techniques, it is possible to create emitters with prolonged photo-stability [15]. Despite the challenges, significant research efforts have made important strides toward establishing coherent control of color centres in hBN. When spin-active, such defects are excellent candidates for quantum coherent manipulation and sensing [16–19]. There has also been progress in Stark effect studies by integrating optically active defects into device with tunable electric fields [20–22]. Several advanced fabrication techniques have successfully demonstrated the deterministic creation of emitters in hBN [23–27], yet there is still much to be understood about the electronic structure of these defects. Many of these fabrication techniques have an SPE yield no higher than 40 % and give a wide distribution of defect type. The reproducible generation of identical defects across multiple samples, particularly in the wavelength range of 532 nm to 650 nm, has motivated numerous research works. However, nanoscale-positioned and identical class emitters in this range which have high quantum efficiency remain a challenge.

With the motivation of using hBN quantum emitters as quantum sensors this research work has been motivated by the following questions:

1. How to fabricate quantum emitters such that they are :
    - Stable
    - Spatially and spectrally deterministic
    - Spin active defect type
2. Are these emitters robust against external molecules?
3. What measurement techniques would confirm their electronic energy level structure

These questions have been answered in the results chapter as follows:

1: How to fabricate quantum emitters that are stable, deterministic and spin active?

We have tested several fabrication methods to create stable quantum emitters in hBN: focused ion beam (FIB), Reactive Ion etching (RIE), Inductively Coupled Plasma (ICP) RIE, sputtering carbon on hBN flakes and also liquid exfoliation of hBN ultra-fine powder onto Si substrate. Each method is followed by high temperature annealing which activates the emitters. Annealing removes adsorbed molecules or contamination and stabilizes the charge state of defects, an essential condition for optical activity, that is, the ability to facilitate light–matter interaction in a two-level system through photon absorption and emission. We show that each of these methods successfully produces quantum emitters albeit they are either unstable, have poor quality, produce a low yield of emitters or are not transferrable to be integrated onto a chip for further sensing measurements. The possible reasons for the fabrication techniques are individually assessed and a general suggestion is proposed in section 4.1. Our experience with developing these fabrication techniques have guided us to explore an additional method, which we have chosen to be our final fabrication method that is Atomic force microscopy (AFM) nanoindentation.

This mechanical method for inducing defects is optimal for preventing charge accumulation during the fabrication process. This technique creates indents using individual force curves at each point. The holes are meant to take up the diameter of the AFM tip (30 nm). The indent is made through only the first several layers of hBN ($\approx$ 2.5 nm). This controlled mechanical approach of creating defect by breaking boron-nitrogen bonds result in smaller lattice destruction as compared to focused helium ion beam (>250 nm) [24] or laser fabrication (2.5 µm) [23].

The AFM tip used is a diamond like carbon coated (DLC) AFM tip which corrodes at each force curve made. This technique introduces carbon particles into the indents promoting formation of carbon defects localized around the indentation which are activated by high temperature annealing. Carbon defects are among the most energetically favorable defects to form in hBN, and theoretical studies expect many to be spin active. Thus this fabrication method is aimed at producing repetitive carbon emitter in hBN, creating emitters which are both spatially and spectrally deterministic. The theory section goes more into detail about defect formation in hBN.

Using AFM and fluorescence measurements, it is shown that this method creates deterministic emitters. Chapters 4.2 and 4.3 discuss the topography changes that occur in hBN because of each fabrication step of indentation, contact AFM scanning and annealing and how this influences defect formation. Chapters 4.4 and 4.5 shows that confirmed single photon sources (SPS) which are stable appear near indentation sites with a 80 % yield and that they consist of good quality emitter features we seek in our emitters. Chapter 4.6 presents the photophysical properties of a large dataset comprising 305 emitters, demonstrating that the majority of isolated single emitters exhibit zero-phonon lines (ZPLs) within the narrow spectral range of 560 nm to 590 nm. This consistent spectral signature indicates the successful and repeatable creation of a specific class of quantum emitters. The data, collected from multiple samples fabricated using the same method, confirms the reproducibility of the process. It further compares the results to existing theoretical work which indicates to the chemical origin of these defects to be carbon-related, specifically, the C_2C_N defect. The spectral features are compared with existing theoretical predictions, providing strong support for this assignment. The energy level structure of this emitter proposed in the theoretical work is reported in details in section 4.6.1.

2. Are these emitters robust against external molecules?

The optical and electrical behavior of a defect is strongly governed by its interaction with the surrounding lattice environment. However, for quantum sensing applications, it is essential that the single-photon emitter (SPE) remains stable when the sensing target is introduced. Since studies have shown that the performance of SPEs in hBN can degrade due to surface contamination, we investigated how our chosen sensing target—single molecular magnet—affect emitter stability. For this purpose, we selected the bis(phthalocyaninato)terbium(III) ($TbPc_2$) molecule due to its well-established magnetic properties [28]. If the emitter remains robust after molecular deposition, it would provide a solid basis for developing hBN-based quantum sensors, an area that is still in its early stages.

Indeed, in Chapter 4.7 we show that addition of molecules do not make the emitters unstable or lose its quantum emitting properties. Remarkably, the introduction of molecules has led to an improved spectral quality of the emitter ZPL and heightened SPE visibility (see A.4 in Appendix) on the hBN flake. The Raman peak of the evaporated molecules from fluorescence data is compared to the Raman peaks of the crystalline form of the molecules (for both $TbPc_2$ and YPc_2) from Raman spectroscopy, to confirm that the emission band from 560 nm and 580 nm are indeed Raman peaks of the Pc ligand. This confirmation

was important because some transition energy level structures of the Tb overlap within the 560 nm to 580 nm range. A recurrent peak around ~ 680 nm is visible when a higher coverage of $TbPc_2$ molecules are deposited. This peak coincides with the fluorescence signal of $Si(IV)tbPc(OH)_2$ reported in an earlier work [29].

3. What measurement techniques would confirm their electronic energy level system?

The fabrication method developed in this work was specifically designed to enable on-chip device integration with quantum emitters in hBN. Elaborate steps were taken to ensure that the hBN flake was transferred onto a coplanar waveguide (CPW) with minimal surface contamination introduced during the transfer, as such impurities can negatively impact the quality of the SPEs. Room-temperature optically detected magnetic resonance (ODMR) measurements were performed on approximately 60 emitters, but only one showed any measurable ODMR contrast (Appendix A.6). Chapter 4.6 presents low-temperature measurements that examine the spectral stability of several emitters under 532 nm excitation laser. Although, low-temperature ODMR did not yield any significant results, photoluminescence excitation (PLE) spectroscopy was successful for one emitter, allowing extraction of its lifetime and natural linewidth. PLE with external vector magnetic field in both the XY and YZ plane revealed no Zeeman splitting indicating spin neutrality for this particular emitter.

This is how the content of the results section have been presented as we have tried to approach the research questions above.

An overview of the thesis is as follows: it starts with the theory section which consists of three main parts. First it focuses on the hBN structure which enables it to have optically active defects with spin properties, many of which are carbon related. We discuss spin active defects due to our interest in sensing.

The second and third parts of the theory section present theoretic concepts in quantum optics that help us analyze and understand our data. The theory section ends with reporting different instabilities that give rise to linewidth broadening of the ZPL in SPS. In the methods section, the optimized fabrication recipe is presented step by step, with reasoning as to why each step was necessary. This is then followed by the results which have already been introduced above. Some extra details are put in Appendix and this is referred to within the main text wherever applicable.

2. Theoretical Background

This chapter is structured to address the following key points:

1. The properties of the materials used, which are crucial to this research.
2. A proposed theoretical model for the defect, its comparison with existing literature, and its implications.
3. Central theoretical concepts in quantum optics relevant to our investigation.
4. Potential limitations in formulating and validating the theoretical framework.

2.1. Hexagonal Boron Nitride

hBN is industrially synthesized, commercially available, inexpensive, and highly versatile, offering a broad range of application possibilities[11]. It is widely used in both industry and research due to its exceptional thermal stability, electrical insulation, and chemical inertness, making it ideal for applications such as protective coatings, electronic substrates, and lubricants [30, 31]. In research, its wide bandgap, high transparency, and ability to host stable quantum emitters make hBN a promising platform for next-generation photonic and quantum technologies. To fully comprehend and further exploit these properties, understanding its structure and chemical composition is essential [32].

2.1.1. Structural Properties

hBN is a layered crystal with strong sp^2 chemical bonds forming hexagonal rings of boron and nitrogen within its two-dimensional layers. Boron has lower electro-negativity than nitrogen, leading to polar covalent bonding; the resulting partial charges create electric dipoles. Between the layers, weak van der Waals forces allow exfoliation into thinner flakes

from the bulk crystal which are then used for experiment. The stacking configuration refers to the relative arrangement of atoms in adjacent layers of a layered material. In AA′ stacking—the most stable configuration for hBN—the layers are aligned such that boron atoms in one layer sit directly above nitrogen atoms in the adjacent layer, and vice versa. This arrangement results in an alternating vertical alignment of boron and nitrogen atoms, with every second layer repeating the same atomic positions. This structure is energetically favorable due to the electrostatic attraction between the partially positive boron and partially negative nitrogen atoms. Consequently, hBN exhibits weaker interlayer bonding compared to few-layer graphite, which has AB (Bernal) stacking, leading to greater thermal expansion and more pronounced thermal puckering at high temperatures in hBN [33]. Figure 2.1 shows the structure of hBN showing the bond length of 1.44 Å and distance between layers as 3.33 Å.

hBN flakes exhibit distinct colors under optical microscopy due to thin-film interference, which aids in pre-selecting flakes for fabrication after exfoliation. When light reflects off the interfaces between air, hBN, and the underlying Si/SiO_2 substrate, the reflected waves interfere based on flake thickness, light wavelength, and hBN's refractive index (typically ~1.8–2.1) [37, 38]. Owing to the high refractive index contrast with air and SiO_2, even slight variations in hBN thickness result in strong interference effects. The altered intensity and phase of the reflected light produce visible color changes, enabling easy, non-destructive thickness estimation [39].

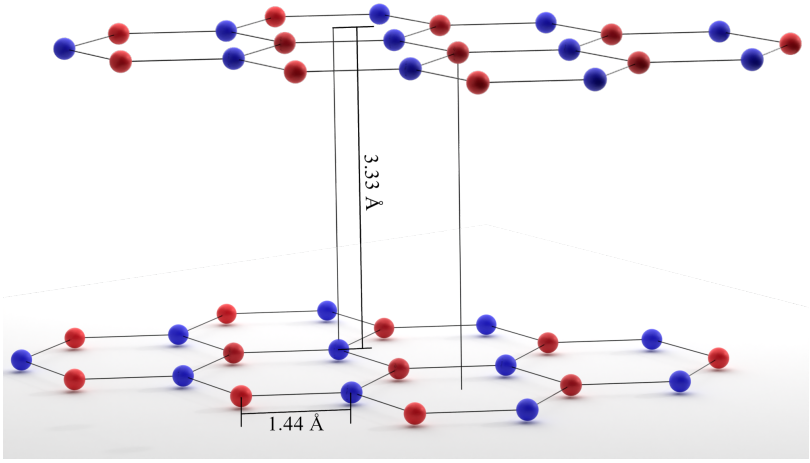

Figure 2.1.: 3D model representing two layers of hBN, with in-plane bond lengths of h-BN: 1.44 Å and plane to plane bond lengths of: 3.33 Å. The red sphere is boron and blue sphere is nitrogen or vice versa. [34–36].

Unlike graphene, which consists of identical carbon atoms and shows no bandgap, (hBN) exhibits a wide bandgap due to the difference in electronegativity between boron and nitrogen [40]. A simple nearest-neighbor tight-binding model accounts for this by introducing a potential difference E_g between the two atomic sites, resulting in the energy dispersion relation:

$$E(\vec{k}) = E_0 \pm \frac{1}{2}\sqrt{E_g^2 + 4|f(\vec{k})|^2},$$

where E_0 is the average site potential and $f(\vec{k})$ is a function of the wavevector $\vec{k}$ [41]. The valence and conduction bands are symmetrically placed around E_0, and the bandgap opens at the K points in the Brillouin zone where $f(\vec{k}) = 0$, giving a gap of exactly E_g. Using the first ionization energies of nitrogen (14.5 eV) and boron (8.3 eV) as a rough estimate for the site potentials gives $E_g \approx 6.2$ eV, which closely matches the experimentally observed optical bandgap of hBN (around 6 eV). This is portrayed in the schematic of a two-level system in figure 2.2. This model illustrates how the broken sub-lattice symmetry in hBN leads to insulating behavior, in contrast to the semi-metallic character of graphene, where both sites are equivalent and $E_g = 0$.

The wide optical bandgap of multilayer hBN results in exceptional transparency, with transmission reaching up to 90 % across a broad spectral range from 250 nm to 900 nm. This high level of transparency makes hBN an ideal encapsulating material for optoelectronic and quantum devices, as it introduces minimal interference with light–matter interactions in the active layers [42].

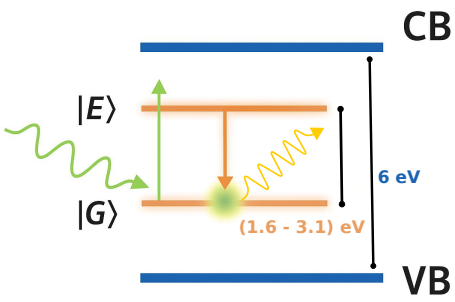

Figure 2.2.: Illustrates a simplified energy level diagram of a two level system for an hBN defect. The $|G\rangle$ is ground state and $|E\rangle$ is the excited state of the defect. CB and VB are conduction band and valence band respectively. Its placement within the 6 eV bandgap of hBN allows it to be optical active.

hBN's wide bandgap enables it to host deep-level defect states within the visible range (1.6 eV to 3.1 eV), which lie well within the bandgap and remain thermally isolated from the valence and conduction bands at room temperature. As a result, many of the color centers formed by such defects in hBN exhibit exceptional thermal stability, making them highly promising candidates for room-temperature quantum technologies [43].

2.1.2. Defects in hBN

Color centres in hBN may arise from vacancies, anti-sites, and carbon substitutions [43–47]. Consider, for example, a boron or nitrogen vacancy, V_B or V_N created by the absence of a boron or nitrogen atom respectively, which results in three broken bonds. The neighboring atoms' σ and π orbitals become de-localized in their environment based on their energy differences. Some may merge into the conduction or valence band, or form deep-level defect states within the bandgap as shown in figure 2.2. Determining the essential electronic states of a defect involves populating its six orbitals with electrons, a process that varies with the defect's chemical composition and charge which will significantly impact its spectral characteristics and spin properties [48].

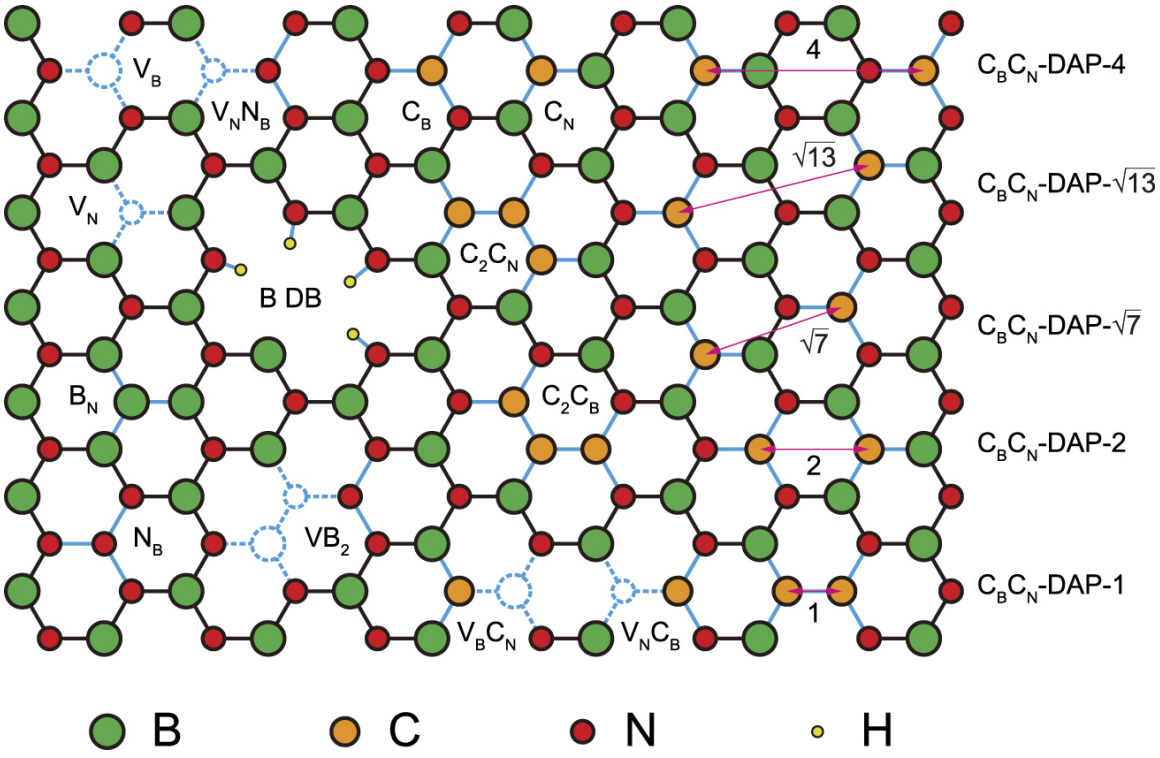

Figure 2.3.: Common defects found in hBN [49].

Energetically favorable defects which are optically active have been reported over several theoretical papers [50, 51]. In their theoretical investigations, they mostly use a combination of first-principles methods to study spin-active defects in hBN, focusing on their structural, electronic, and spin-related properties. Density functional theory (DFT), particularly with hybrid functionals like HSE06, is used to accurately describe defect levels within hBN's wide bandgap. HSE06 is a screened hybrid functional that mixes a portion of exact Hartree–Fock exchange with DFT exchange-correlation [52], improving the accuracy of bandgap and defect level predictions in semiconductors and insulators. The calculations rely on the Born–Oppenheimer approximation, which separates electronic and nuclear motion to simplify the problem, and use pseudopotentials to exclude core electrons and reduce computational cost. Commonly utilized techniques encompass these above mentioned calculations: density functional theory (DFT), Hartree–Fock (HF) approaches, and post-HF methods. A summary of the defects is provided in table 2.1, which were proposed in earlier studies, with references listed next to the defect information. As they may be using combination of different calculation schemes their derived defect electronic structure for each defect may also vary.

Some common defects in hBN are illustrated in Figure 2.3 [49]. These defects are paramagnetic, and several of them exhibit multiple charge state configurations. For instance, the defects shown on the left side of the figure—V_N, V_NN_B, B_N, and N_B—can exist in positive, negative, and neutral charge states, each of which influences their ground-state spin. For example, V_N has a neutral spin when positively charged, whereas B_N and N_B exhibit neutral spins in their neutral charge states. In contrast, V_NN_B shows a neutral spin when either positively or negatively charged. These examples demonstrate that the spin state of single-photon emitters (SPEs) is determined by their ionization state.

The defects depicted near the center of the hBN lattice in Figure 2.3—C_B, C_N, C_2C_N, C_2C_B, V_BC_N, and V_NC_B—are among the most frequently studied carbon-related defects in experimental research [46, 53]. These defects are considered potential origins of many experimentally observed quantum emitters. Notably, the neutral charge states of V_BC_N and V_NC_B are theoretically predicted to possess a spin-triplet ground state, while the remaining carbon-related defects are primarily associated with spin-doublet ground states [54]. The charge and spin states of these well-studied defects, as presented in figure 2.3, are summarized in table 2.1. Due to their potential to form stable spin-active centers in hBN, carbon defects—particularly carbon trimers—have received significant research attention. In table 2.1, the zero-phonon line (ZPL) values for the carbon trimers C_2C_N and C_2C_B are reported by both Auburger et al. [55] and Li et al. [56]. This is further discussed in the

results section, where we propose that the most frequently observed defects in our study are C_2C_N carbon trimers.

Table 2.1.: Key properties of widespread spin-active defects in hBN from theoretical investigations. Charge states, ZPL energies (in eV), ground-state spins (S_{gs}), and zero-field splittings (ZFS in GHz) are included. This is nicely summarized in [49] and some additional data is added to the existing table.

Defect	**Charge state**	**ZPL (eV)**	S_{gs}	**ZFS (GHz)**
V_B	−	1.65 [57]	1 [58]	3.467 [57]
	0	/	3/2	/
V_N [51]	−	/	/	/
	0	/	1/2	/
	+	/	0	/
B_N [51]	−	/	1	/
	0	/	0	/
	+	/	1	/
N_B [51]	0	/	0	/
	+	/	1/2	/
$V_N N_B$ [48]	−	/	0	2.0
	0	/	1/2	/
	+	/	0	1.74
Boron DBs		2.0 [47]	0 [59]	0.84 [59]
VB_2 [60]		/	1	$D = -1.1$, $E = -76.8$ MHz
C_N [55]	0	2.468	1/2	/
C_B [55]	0	1.695	1/2	/
$C_B C_N$-DAPs (4, $\sqrt{13}$, $\sqrt{7}$, 2, 1) [55]	−	1.525–0.442	1/2	/
	0	1.547–4.131	0	/
	+	2.229–1.055	1/2	/
C_2C_N	0	2.13 [56]	1/2	/
		1.62 [55]	1/2	
C_2C_B		1.42 [56]	1/2	/
		1.36 [55]		
$V_N C_B$	− [61]	/	1/2	/
	0 [62]	1.95	1	8.6
	+ [61]	/	1/2	/
$V_B C_N$ [62]	0	/	1	−7.15

Carbon Defects in hBN

Carbon defects in hBN are commonly found as unintentional impurities introduced during synthesis. In bulk hBN crystals grown via high-temperature, high-pressure (HTHP) methods using barium boron nitride as a solvent [63], carbon has been detected in exfoliated samples using annular dark-field electron microscopy [64]. Similarly, in chemical vapour deposition (CVD) of hBN thin films using precursors such as ammonia borane (NH_3BH_3) and borazine ($B_3N_3H_6$), carbon incorporation is frequently observed [65, 66]. These precursors thermally decompose and react with the substrate (typically copper), facilitating hBN growth and the introduction of carbon-related defects.

Carbon's tendency to be incorporated into the hBN lattice arises from its position in the periodic table—between boron and nitrogen—which allows it to substitute for either element due to similar atomic sizes and electronic configurations. Simple substitutional defects such as C_B (carbon on a boron site) and C_N (carbon on a nitrogen site) exhibit low formation energies and thus can occur in relatively high concentrations compared to more complex configurations [46, 55, 67].

Grain boundaries and Stone–Wales (SW) defects further enhance the likelihood of carbon incorporation by distorting the ideal hBN lattice and creating energetically favorable sites for impurity trapping [68]. A Stone–Wales defect is a type of topological defect that occurs in 2D materials like graphene and hBN. It involves a 90° rotation of a bond between two adjacent atoms, transforming four hexagons into two pentagons and two heptagons. These structurally perturbed regions can host substitutional or interstitial carbon atoms, which are of particular interest due to their distinctive optical and quantum properties [69, 70].

Figure 2.3 illustrates several well-known carbon-related defects, including donor–acceptor pairs (C_BC_N-DAPs). In such pairs, C_B acts as an acceptor and C_N as a donor. Radiative recombination occurs when an electron from the donor recombines with a hole at the acceptor, resulting in photon emission. The defect can undergo charge-state transitions, altering both its electronic and magnetic properties. The recombination energy depends on the donor–acceptor separation (e.g., 1, 2, 4, $\sqrt{7}$, $\sqrt{13}$ lattice units in the neutral state), with shorter separations yielding higher-energy emission, as summarized in Table 2.1.

2.2. Quantized Emission of Light

The quantum nature of light emerges when classical electromagnetic theory fails to explain phenomena such as single-photon emission, antibunching, and photon number quantization. In quantum optics, the electromagnetic field is quantized, and its excitations—photons—are described using quantum states. A fundamental class of such states are the Fock states [71].

2.2.1. Fock States and Photon Number Quantization

A **Fock state** (or number state) is a quantum state with a well-defined number of photons. Denoted as $|n\rangle$, it contains exactly n photons in a given mode of the field. It is an eigenstate of the photon number operator $\hat{n} = \hat{a}^\dagger \hat{a}$:

$$\hat{n}\,|n\rangle = n\,|n\rangle \tag{2.1}$$

where $\hat{a}^\dagger$ and $\hat{a}$ are the photon creation and annihilation operators satisfying $[\hat{a}, \hat{a}^\dagger] = 1$.

Fock states exhibit no photon number uncertainty; that is, when measuring the number of photons in such a state, the result is exactly n photons. This deterministic nature makes Fock states inherently non-classical. In contrast, classical light—such as that emerging from a laser—always exhibits some degree of photon number fluctuation. Among Fock states, the single-photon state $|1\rangle$ is particularly important for quantum technologies, including quantum communication and quantum key distribution [72]. It enables quantum-secure transmission by eliminating multi-photon vulnerabilities and allows for deterministic encoding and transfer of quantum information.

The Poisson distribution describes the probability of a certain number of independent events occurring within a fixed time or space interval, assuming a constant average rate. For photons in a laser beam (a coherent light source), the photon number distribution follows this Poisson distribution function:

$$P(n) = \frac{\lambda^n e^{-\lambda}}{n!}$$

where $P(n)$ is the probability of detecting an integer number of n photons, and λ is the average photon number. When the average is set to $\lambda = 1$, most detection events result in 0 or 1 photon, although higher photon numbers are still possible.

This randomness, and the fact that photons are independent, means that laser light cannot be truly antibunched—even if attenuated—because there is always a nonzero probability of two or more photons arriving together as shown in figure 2.5(a) and figure 2.5(d) represented by the red bar. Lasers are sources of coherent light, meaning the photons maintain a fixed phase and amplitude across time and space.

In contrast, thermal light (e.g., sunlight or blackbody radiation) tends to emit photons in bunches, leading to a higher likelihood of detecting either zero photons or multiple photons per event as portrayed in figure 2.5(b). The photon distribution in this case follows a Bose–Einstein distribution, which favors clustering as shown in figure 2.5(d) represented by the black bar.

SPS, on the other hand, emit photons in an antibunched manner—meaning photons are well-separated in time as shown in figure 2.5(c). This results in a sub-Poissonian distribution, where the probability of detecting exactly one photon is high, and the chance of multi-photon events is negligible as visible in figure 2.5(d).

A critical factor in measuring these statistics is the sampling or detection time interval. To observe the true distribution (especially antibunching), the detection time bins must be smaller than the average time between photons. Otherwise, time averaging can mask the actual statistical behavior.

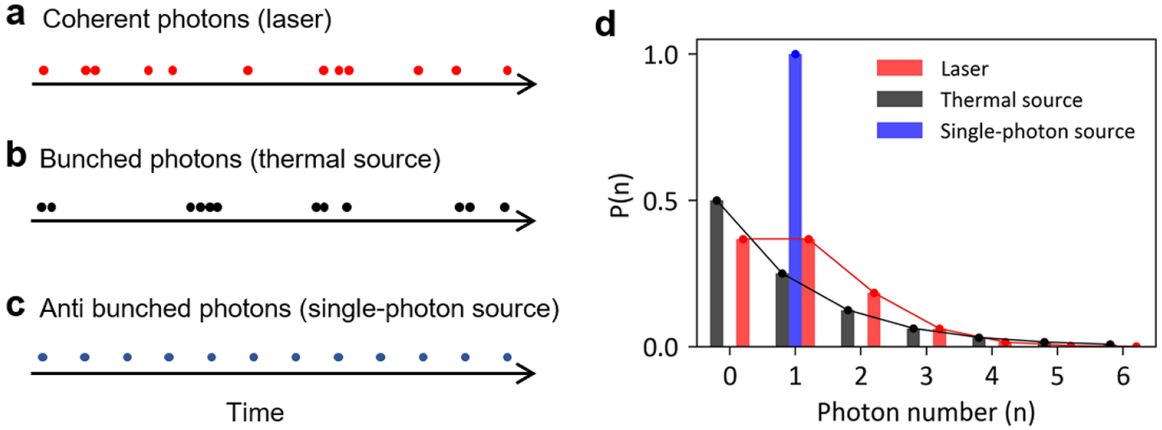

Figure 2.4.: (a)-(c) show schematic comparing the photon incidents of different light sources under the same intensity. (d) shows probability distribution of the photon number from the three sources where the average photon is $\langle n \rangle = 1$. These are the calculated probability values of detecting "n" photons at a given time. Schematic taken from Ref [11].

2.2.2. First-Order Coherence

In quantum optics, correlation functions are used to characterize the statistical and coherence properties of an electromagnetic field. The first order coherence of light refers to the degree of correlation between field amplitudes at different points in space or time. It is defined as:

$$g^{(1)}(\tau) = \frac{\langle \mathcal{E}^*(t)\mathcal{E}(t+\tau)\rangle}{\langle |\mathcal{E}(t)|^2\rangle} \tag{2.2}$$

The angled brackets denote the statistical averaging operator. Here, $\mathcal{E}(t)$ represents the electric field at time (t), and τ is the time delay between two field measurements. The $\mathcal{E}^*(t)$ is the complex conjugate of the electric field. The nominator gives a quantity that reflects both amplitude correlation and phase difference between the field at time (t) and (t + τ). This formulation applies directly to interference phenomena—such as the fringe patterns observed in a Michelson interferometer or thin-film interference—where the overall intensity results from the constructive and destructive interference of two overlapping electric field amplitudes [73]. This quantity is linked to classical interference phenomena. Perfectly coherent light (e.g., from a laser) has $|g^{(1)}(\tau)| = 1$, while thermal or incoherent light exhibits a decaying $|g^{(1)}(\tau)|$ with increasing τ.

2.2.3. Second-Order Correlation and Photon Statistics

While first-order coherence describes the wave-like interference properties of light fields, the quantum statistical nature of photons is revealed through the second-order correlation

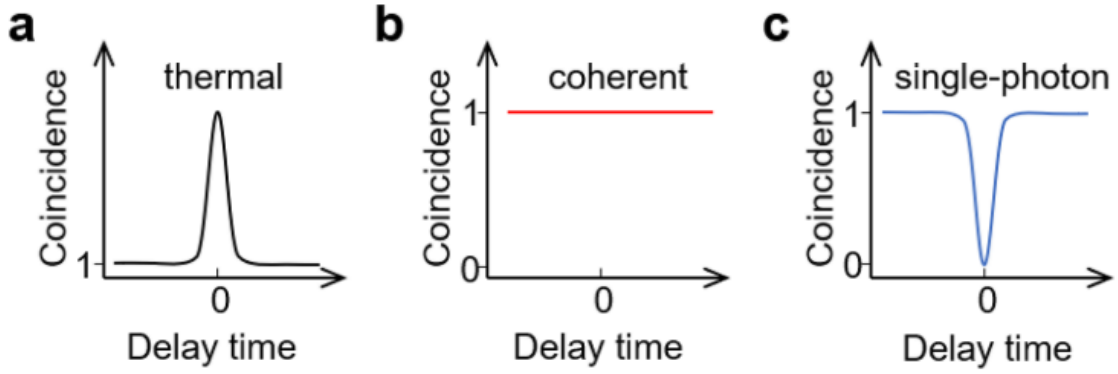

Figure 2.5.: Shows $g^{(2)}$ profile for the three light sources shows in figure 2.4 [11].

function, which characterizes intensity–intensity correlations at different times. This function is particularly useful in distinguishing classical light from quantum light, and is directly measurable in photon-counting experiments.

In classical electrodynamics, field intensity (or energy density) is proportional to the square of the electric field amplitude which is given by (2.2). Based on this, the second-order correlation function is defined as:

$$g^{(2)}(\tau) = \frac{\langle \mathcal{E}^*(t)\mathcal{E}^*(t+\tau)\mathcal{E}(t+\tau)\mathcal{E}(t)\rangle}{\langle \mathcal{E}^*(t)\mathcal{E}(t)\rangle \langle \mathcal{E}^*(t+\tau)\mathcal{E}(t+\tau)\rangle} = \frac{\langle I(t)I(t+\tau)\rangle}{\langle I(t)\rangle\langle I(t+\tau)\rangle} \tag{2.3}$$

Here, $I(t)$ and $I(t+\tau)$ denote the field intensities at times t and $t+\tau$, respectively, and τ represents the time delay between detection events. This expression captures the normalized probability of detecting two photons separated by time τ. A value of $g^{(2)}(\tau) > 1$ indicates that photons tend to arrive together (bunching), whereas $g^{(2)}(\tau) < 1$ indicates that photons avoid each other (antibunching), which is a purely quantum effect. Bunched and anti-bunched sources of light are introduced in section 2.2.1.

In photon-counting experiments—particularly those using a Hanbury Brown and Twiss (HBT) interferometer (figure A.4)—the second-order correlation function is expressed in terms of photon number counts from two detectors:

$$g^{(2)}(\tau) = \frac{\langle n_1(t)n_2(t+\tau)\rangle}{\langle n_1(t)\rangle \langle n_2(t+\tau)\rangle} \tag{2.4}$$

Here, $n_1(t)$ and $n_2(t+\tau)$ represent the photon counts at two detectors, separated by a time delay τ. This expression gives the conditional probability of detecting a photon at detector 4 given that one was detected at detector 3 at an earlier time.

To describe these processes fully quantum mechanically, we replace the photon number operators with their operator equivalents. The photon number operator is defined as $\hat{n} = \hat{a}^\dagger\hat{a}$, where $\hat{a}^\dagger$ and $\hat{a}$ are the creation and annihilation operators (also called ladder operators), respectively. Substituting this into Equation (2.4) yields the following quantum optical definition:

$$g^{(2)}(\tau) = \frac{\left\langle \hat{a}^\dagger(t)\hat{a}^\dagger(t+\tau)\hat{a}(t+\tau)\hat{a}(t)\right\rangle}{\left\langle \hat{a}^\dagger(t)\hat{a}(t)\right\rangle \left\langle \hat{a}^\dagger(t+\tau)\hat{a}(t+\tau)\right\rangle} \tag{2.5}$$

In this formulation, the ladder operators serve as quantum field operators that describe the absorption and emission of photons. The annihilation operator $\hat{a}$ removes a photon from the field, while the creation operator $\hat{a}^\dagger$ adds one. These operators obey the canonical commutation relation $[\hat{a}, \hat{a}^\dagger] = 1$, for bosons and act on Fock (number) states according to:

$$\hat{a}\,|n\rangle = \sqrt{n}\,|n-1\rangle\,, \quad \hat{a}^\dagger\,|n\rangle = \sqrt{n+1}\,|n+1\rangle$$

This operator-based formulation is essential for analyzing quantum optical systems, as it allows the computation of expectation values for different quantum states of light—such as coherent states, thermal states, and Fock states. It also provides a natural way to incorporate field quantization into photon statistics.

The value of $g^{(2)}(0)$, i.e., at zero time delay, is particularly important as it reveals the nature of the photon statistics of the light source:

- Thermal (chaotic) light: $g^{(2)}(0) = 2$, indicating photon bunching.
- Coherent light (e.g., laser): $g^{(2)}(0) = 1$, characteristic of Poissonian statistics.
- Fock state $|n\rangle$: $g^{(2)}(0) = \frac{n(n-1)}{n^2}$, which approaches 1 as $n \to \infty$, and equals 0 for $n = 1$.

In particular, for a single-photon Fock state $|1\rangle$, the second-order correlation at zero delay is:

$$g^{(2)}(0) = 0 \tag{2.6}$$

This behavior, known as photon antibunching, is a hallmark of non-classical light and cannot be explained by classical electromagnetic theory. Antibunching is a clear signature of single-photon emission and is typically measured using an HBT interferometer (figure A.4). An experimentally observed value of $g^{(2)}(0) < 0.5$ is considered a definitive indicator of an SPE. Figure 2.4 demonstrates $g^{(2)}(0)$ for different light sources.

2.3. Possible Emission Scheme of Defects

In experiments, this emission is typically observed via a photoluminescence (PL) spectrum, which records the intensity of emitted photons as a function of wavelength or energy. A

typical PL spectrum of a quantum emitter in hBN features a sharp, intense peak known as the ZPL, corresponding to a purely electronic transition between the ground and excited states. This peak is often accompanied by a broader, red-shifted spectral feature called the PSB, which arises due to the coupling of electronic transitions with lattice vibrations (phonons). Together, the ZPL and PSB form the characteristic spectral fingerprint of an emitter.

Quantized photon emission from defects in hexagonal boron nitride (hBN) can be understood through the schematic shown in Figure 2.6. This illustration depicts a direct optical transition, which is the most commonly used model to describe defect-related emission in hBN. The emission process can be described as follows: an incoming photon excites the system from the ground-state equilibrium to a point above the excited-state equilibrium, requiring an energy input of ΔE_v^{A}. The system then undergoes an *adiabatic relaxation* to the excited-state equilibrium by dissipating excess energy λ^{A} into phonon modes.

The system then relaxes to the ground-state equilibrium by emitting a photon with energy ΔE_v^{E}, followed by a second adiabatic relaxation in which vibrational energy λ^{E} is released. This is the Franck-Condon principle for electronic excitations in molecules where the excitation/relaxation are much faster than the vibronic relaxation. The energy difference between the equilibrium positions of the excited and ground states defines the adiabatic transition energy ΔE_0.

The vertical transitions—ΔE_v^{A} during excitation and ΔE_v^{E} during emission—are referred to as vertical excitation and relaxation, respectively. Their energy difference, $\lambda^{\mathrm{A}} + \lambda^{\mathrm{E}}$, is

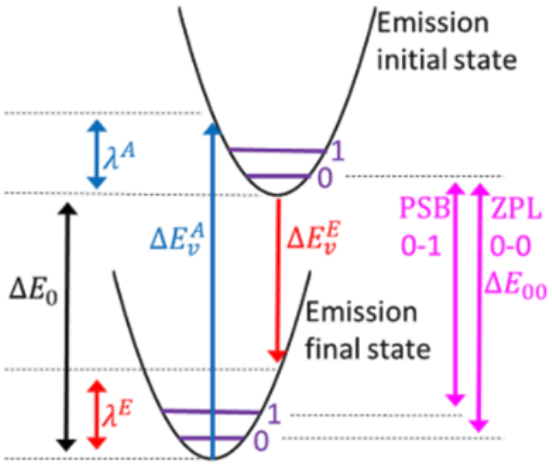

Figure 2.6.: Schematic of the potential well structure showing light matter interaction that results in photon emission and phonon vibrations [48].

called the Stokes shift, and it quantifies the energy lost to phonon interactions during the emission cycle.

To improve accuracy, the adiabatic transition energy ΔE_0 can be corrected by including the zero-point energy of each vibrational state, resulting in the corrected ZPL energy ΔE_{00}. The remaining emission, associated with phonon-assisted relaxation, forms the PSB. This occurs due to the mismatch in lattice geometry between the excited and ground states, causing the system to relax by emitting phonons with various characteristic vibrational energies. The superposition of these vibrational transitions makes up the PSB, which appears red-shifted from the ZPL due to the lower energy of phonons. In PL spectra, this manifests as a broad tail extending toward longer wavelengths; in some cases, it may be partially obscured by the detection limit or signal noise.

The absorption counterpart, denoted ΔE_{10}, the energy difference marked as 'PSB 0-1', corresponds to the energy involving phonon-assisted excitation. The direct transition model described here is widely used to calculate and simulate the optical response of hBN defects. Additional parameters, such as the Huang–Rhys (HR) factor and Debye–Waller (DW) factor, are also employed to characterize the strength of electron–phonon coupling and the fraction of emission in the ZPL, respectively. These are discussed in the following section.

2.3.1. Huang-Rhys Factor and Debye-Waller Factor

The HR factor serves as a measure of electron-phonon interaction strength during optical transitions, indicating the average quantity of phonons engaged when a system transitions between distinct electronic states, which results in equilibrium geometry changes. For emission, the HR factor S_E is defined as:

$$S_E = \sum_i S_i^E = \sum_i \frac{(\delta_i^E)^2}{2}, \tag{2.7}$$

where δ_i^E is the mass-weighted displacement between excited and ground-state potential energy geometries along mode i, summed over all vibrational modes. A higher S_E denotes stronger coupling and a more noticeable PSB, whereas a lower S_E implies weaker coupling

with a predominant ZPL. The DW factor, α_E, represents the ratio of the ZPL intensity to the total emission intensity, defined by:

$$\alpha_E = \frac{I_{\text{ZPL}}}{I_{\text{total}}} = e^{-S_E}, \tag{2.8}$$

where I_{ZPL} is the zero-phonon line's integrated intensity, and $I_{\text{total}} = I_{\text{ZPL}} + I_{\text{PSB}}$ is the sum total of integrated emissions. A larger DW factor ($\alpha_E \longrightarrow 1$) signifies that emission mainly occurs through the ZPL, which is highly advantageous for quantum optics applications requiring indistinguishable photons [74, 75]. It is important to recognize that obtaining precise values for S_E and α_E from experimental data is often challenging due to spectral overlap among the ZPL, PSB, and Raman features of the material, limitations in detection equipment, and the need to accurately convert intensity data from wavelength to energy with appropriate scaling.

2.3.2. Photo-instabilities

Defects in hBN are highly sensitive to their local environment and often deviate significantly from the idealized two-level system typically used to model SPE. In realistic conditions, additional charges and nearby defects can perturb the electronic structure of the optically active defect, resulting in a more complex energy level scheme [76, 77].

Spectral diffusion in hBN emitters mainly comes from fluctuations in local charges that change the surrounding electric field of the defect. One common cause is the Stark effect, where nearby charges—such as mobile carriers or photogenerated electrons—shift the energy levels of the emitter and lead to changes in the emission energy over time [78]. For instance, a focused laser may unintentionally excite surrounding systems in addition to the target emitter. This can induce electric dipoles in nearby defects or impurities, leading to a local electric field and thereby causing a Stark shift in the emission energy of the main emitter [79]. Another factor is charge trapping and detrapping, where charges get temporarily caught in nearby defect sites or impurities and then released again. These events alter the local potential landscape, causing the emission energy to fluctuate [80, 81]. On top of that, surface-related effects such as adsorbed molecules, charge patches, or nearby conductive layers like graphene can also disturb the emitter by introducing additional electric noise [82, 83]. This is especially relevant for 2D materials like hBN, where the emitters are very close to surfaces and interfaces. Altogether, these effects

result in spectral wandering, linewidth broadening, or even blinking, which can reduce the spectral stability of the emitter.

In other cases, nearby charges can also give rise to metastable states that act as non-radiative decay channels [14, 84], resulting in intermittent fluorescence or blinking [85]. Blinking refers to the reversible switching between emissive and non-emissive states, in contrast to photobleaching, where the emitter becomes permanently non-emissive due to irreversible chemical or structural changes.

Therefore, engineering a stable and clean local environment through advanced fabrication techniques is critical for controlling the photophysical properties of hBN quantum emitters, and ultimately for their successful integration into quantum photonic devices.

Linewidth broadening The natural linewidth of an optical transition is connected to the time energy uncertainty principle as follows, where Γ is the natural linewidth:

$$\Gamma = \frac{\Delta v}{2} = \frac{\Delta E}{2h} > \frac{1}{2\pi\Delta t} \tag{2.9}$$

Here, Δv is the full spectral width in frequency units, ΔE is the energy uncertainty of the transition, h is Planck's constant, and Δt is the lifetime of the excited state. It relates the spectral linewidth to the lifetime of the excited state which is also knows as the Fourier transfer limited (FTL) linewidth. This inequality reflects that a shorter excited-state lifetime (smaller Δt) leads to a broader linewidth Γ. This fundamental limit is rooted in the Heisenberg uncertainty principle, which states that energy and time cannot both be precisely defined simultaneously. Hence, the faster a photon is emitted, the less well-defined its energy, leading to a wider spectral line.

However, in practice, the observed linewidth often exceeds the natural linewidth due to additional broadening mechanisms. These are typically categorized as homogeneous and inhomogeneous broadening. Homogeneous broadening, which results in a Lorentzian lineshape, arises from processes that affect all emitters equally, such as phonon coupling and interactions with the environment that limit the coherence time. In contrast, inhomogeneous broadening leads to a Gaussian lineshape and originates from emitter-to-emitter variations, such as local strain or charge fluctuations in the surrounding environment [71, 86].

3. Methods

3.1. Fabrication Recipe

Each fabrication step is carefully designed to support the formation of stable, isolated quantum emitters. A critical factor in achieving this is maintaining a clean local environment. By 'clean' I am referring to the following conditions:

- minimal surface or inter-layer contamination that could degrade emitter quality.
- absence of charge accumulation.
- a well-defined, structured physical topography. Thus many extra steps within the fabrication procedure are taken to maintain this clean environment. Once formed, the SPEs are stable with a long shelf life.

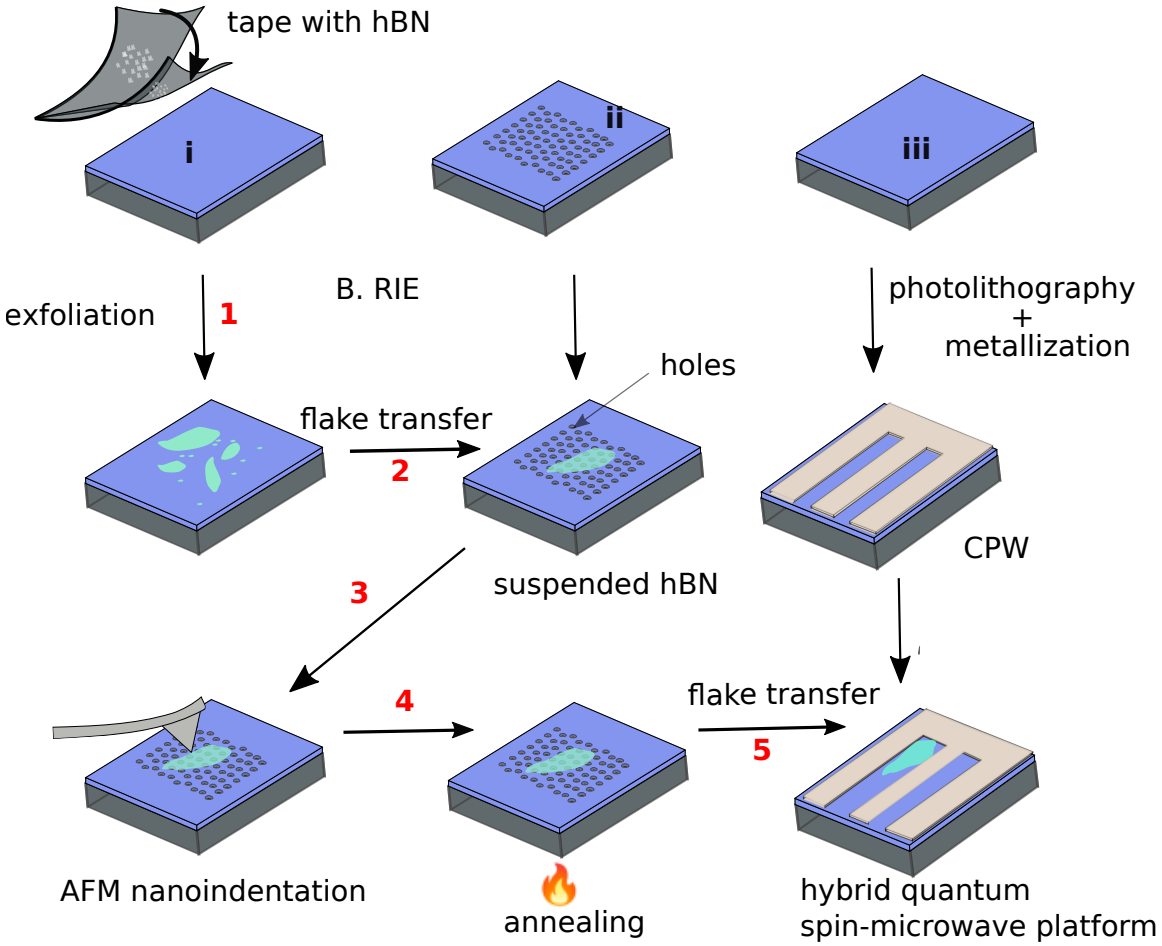

Figure 3.1.: Fabrication steps to creating deterministic quantum emitters in hBN that is compatible for chip device integration. The process requires three chips: exfoliation is done on chip (i), holes are patterned using RIE in chip (ii) and CPW is fabricated on chip (iii). All fabrication steps on the three chips are required to create the final chip that is the hybrid quantum spin-microwave platform.

Figure 3.1 presents a schematic of the fabrication process. Intrinsic silicon wafer, coated with a 300 nm thermal oxide layer and 500 µm) in thickness, is diced into smaller than 5 mm × 5 mm square chips and cleaned thoroughly. The cleaning protocol involves sequential treatment with hot acetone, ethanol, isopropanol (IPA), and plasma cleaning. All freshly diced chips undergo this procedure prior to device fabrication.

To fabricate the final hybrid quantum spin–microwave platform, three separate chips are used. On the first chip, hBN flakes are exfoliated. The second chip is patterned with micrometer-scale holes via etching, and the third chip is used to define a CPW through photolithography.

Selected hBN flakes from the first chip are transferred onto the second chip such that the flake is suspended over the etched holes. AFM nanoindentation is then performed on the

suspended flake, followed by annealing at 1000 °C. Subsequently, the flake is transferred once more onto the CPW on the third chip.

The resulting SPE in hBN from AFM nanoindentation are characterized via both room-temperature and cryogenic confocal microscopy to assess their photophysical properties. Further experiments are carried out to investigate the spin properties of the emitters. The motivation behind each fabrication step is discussed in this section, and fabrication step is further summarized in labeled boxes in the Appendix.

3.1.1. Exfoliation

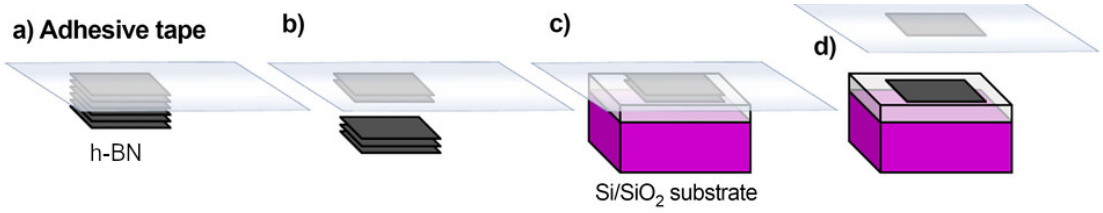

Figure 3.2.: Schematic of mechanical cleavage of hBN powdered crystals into thin flakes and final exfoliation onto target substrate.

The hBN powdered crystals used for exfoliation are sourced from Micromasch. Exfoliation is performed using acrylic adhesive tape (Nitto SPV 224PR-MJ, thickness: 75 µm). Although this tape is typically used as a protective film, its low adhesive strength makes it suitable for exfoliation, minimizing the transfer of adhesive contaminants to the flakes.

Given that the hBN crystals are initially several micrometers thick, they are cleaved four to six times using a fresh piece of tape each time in order to obtain thinner flakes. After several cleaving cycles, the flakes become thinner and sparser, appearing barely visible on the tape. The tape is then pressed uniformly onto a chip that has just been removed from a hotplate, applying orthogonal pressure for several seconds before peeling it off. Exfoliation steps is illustrated in figure 3.2.

The chips are kept warm during exfoliation to enhance the adhesion of flakes, thereby increasing yield. However, exfoliation is not performed directly on a 200 °C hotplate, as such high temperatures would degrade the tape and risk depositing adhesive residues onto the chip surface.

Applying uniform pressure without twisting is essential to avoid introducing adhesive contaminants or air bubbles beneath the hBN flakes. This process constitutes a final "on-chip" exfoliation rather than a "transfer"—meaning the top and bottom surfaces of the flake on the chip are both freshly cleaved layers of hBN. Ideally, this ensures that the exfoliated flakes on the chip are free from adhesive contamination.

Following exfoliation, the flakes are optically inspected to determine their positions and thicknesses in preparation for further fabrication steps [39]. Flakes with thicknesses between 40 nm and 100 nm are preferred. On average, exfoliated flakes from powdered crystals are approximately 40 µm in lateral size. Exfoliation from bulk hBN single crystals follow the same method, beginning with a large crystal piece several hundred micrometers in size. Flakes obtained from single crystals are often larger than those derived from powdered sources. The cleaning and exfoliation is summarized and listed in colorbox titled "Cleaning and exfoliation" in A.1.

If reusing a chip that was previously used for exfoliation, the sample is first wiped with a lint-free wipe—such as those commonly used in cleanroom environments—to remove any optically visible debris accumulated over time. This step effectively removes residual flakes from prior exfoliations that are not efficiently eliminated by alcohol or plasma cleaning alone. After wiping, the standard cleaning procedure and exfoliation process can be repeated.

3.1.2. Patterning Holes into Si/SiO_2

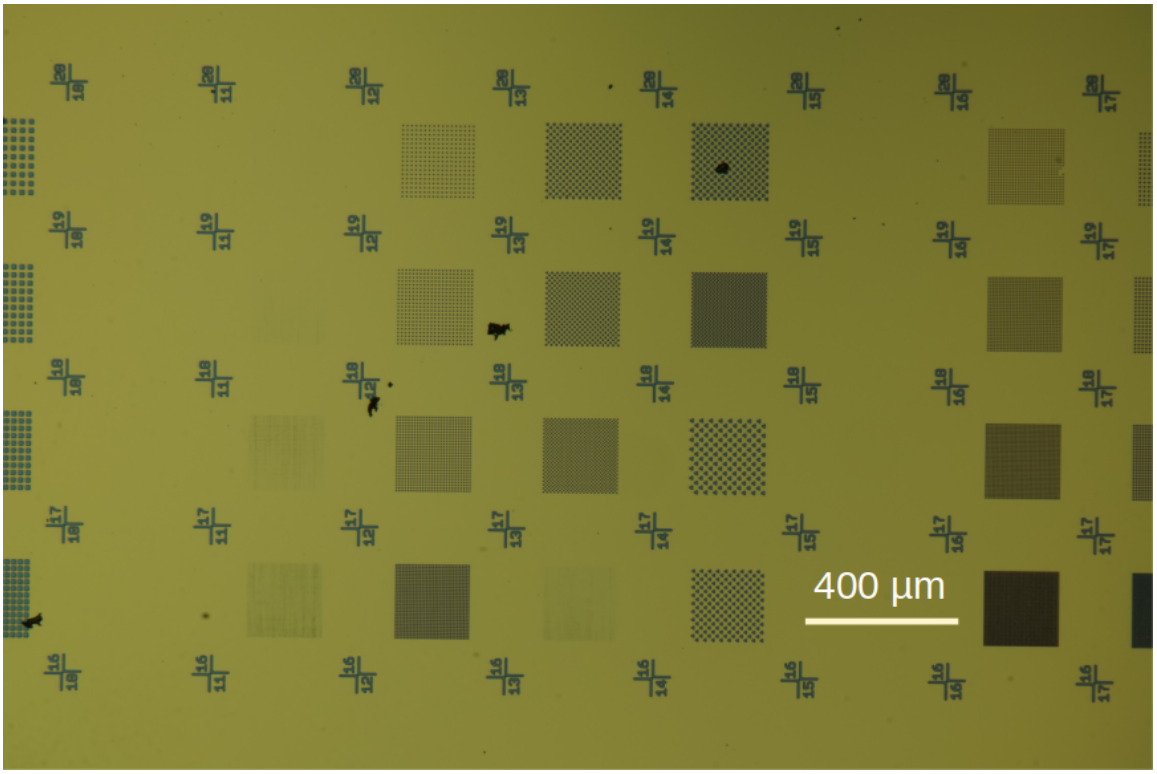

Figure 3.3.: Patterned holes in different sizes in Si/SiO_2 with markers.

This step aims to exfoliate or transfer hBN flakes onto etched holes, allowing them to become suspended. During emitter fabrication, high-temperature annealing strengthens the bond between the flake and the SiO_2 substrate, making later transfer difficult. In contrast, suspended flakes experience weaker van der Waals interactions with the substrate, enabling easier pickup via our dry transfer method. Moreover, substrate changes during annealing have less effect on suspended flakes.

Figure 3.3 shows an optical image of the chip after the etching process. Alignment markers assist in quickly locating flakes during measurements. The etched holes vary in size (2, 4, 8, and 12 µm), shape, and spacing (2 µm to 12 µm) between the centre of consecutive holes, allowing for the exploration of optimal conditions for flake adhesion. Among these, the 2 µm circular holes with 6 µm spacing yielded the highest number of suspended flakes after exfoliation. The complete etching process is summarized in colorbox "Patterning holes into Si/SiO_2" in A.1.

When post-annealing transfer is unnecessary, that is, if the flakes are not going to be moved to a waveguide (chip 3), the flakes can be indented and annealed directly on the exfoliated chip (chip 1) to activate color centres in hBN. Although exfoliating directly onto a pre-etched chip (chip 2) is also possible, flake placement becomes random and uncontrollable. Hence the desired flake is preselected and transferred from chip 1 to chip 2 to be suspended, and then finally transferred to chip 3 after annealing. Annealing chip with the waveguide (chip 3) might destroy the waveguide so this is also avoided.

The pattern is made using photolithography and then etched using Reactive Ion Etching (RIE) with SF_6 and C_4F_8 gases. The Bosch process [87] is used to achieve deep anisotropic etching in silicon through alternating cycles of etching and passivation. In the etch step, SF_6 is introduced into the plasma, generating fluorine radicals (F•) which chemically react with silicon and silicon dioxide to form volatile SiF_4:

$$SiO_2 + 4F\bullet \rightarrow SiF_4\ (\text{gas}) + O_2\ (\text{gas})$$

$$\text{Si (solid)} + 4F\bullet \rightarrow SiF_4\ (\text{gas}) \tag{3.1}$$

During the passivation step, C_4F_8 is flowed into the chamber, leading to the deposition of a fluorocarbon-based polymer on all exposed surfaces:

$$C_4F_8 \rightarrow C_xF_y\ (\text{polymer}) \tag{3.2}$$

Ion bombardment in the subsequent etch cycle removes the polymer from the trench bottom, enabling further vertical etching while the sidewalls remain protected. Repeating these cycles allows for high aspect ratio structures with vertical sidewalls in silicon.

The following figures show suspended flake on etched sample. Suspending flake is required for on chip device integration so that they are are still transferrable after annealing. Owing to hBN's high heat resistance, the Si holes that are covered with hBN stay protected and unchanged from destruction via annealing.

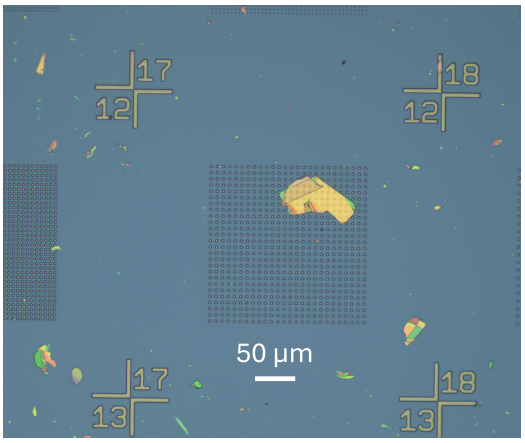

Figure 3.4.: Large exfoliated flake on an etched block, the distance between the numbered markers is 400 µm.

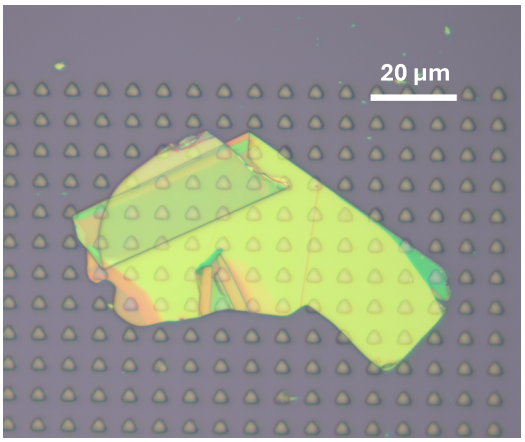

Figure 3.5.: Suspended flake on triangular holes which are etched into the Si substrates. The flake has less attraction to the substrate when suspended and hence it becomes possible to transfer them after annealing.

3.1.3. PDMS Microdome and Dry Transfer

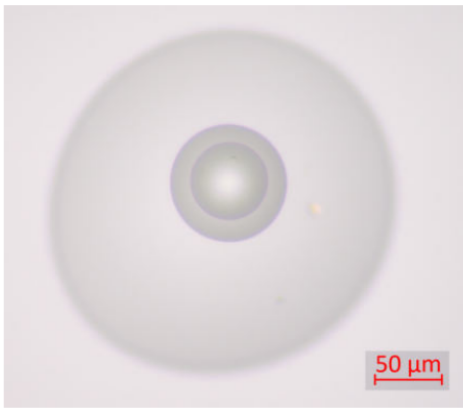

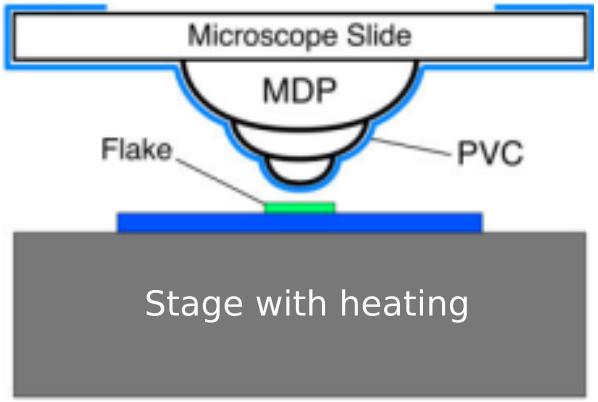

Figure 3.6.: Top view of an exemplary PDMS microdome stamp (left) and PVC film wrapped over the PDMS microdome stamp (right).

hBN flakes are transferred onto target substrates with micrometer precision using a dry transfer technique involving microdome stamps [88]. Microdome stamps are fabricated from Polydimethylsiloxane (PDMS) with an array of tiny domes in a microdome shape. A layer of polyvinyl chloride (PVC) film is then wrapped around the PDMS stamp before it is installed into the transfer setup. These domes have micron-scale curvature, which allows localized contact with a flake or substrate. The contact point can be adjusted by controlling pressure or alignment, enabling precise flake pickup or release. This enables transfer of

pre-selected flakes with desired thickness onto etched holes or CPW which cannot be achieved with exfoliation as the position of the flake on the chip during exfoliation is uncontrolled. Figure 3.6 shows one of the stamps made on the left with the last spherical drop being around 50 µm diameter. On the right, a side view schematic of the stamp with PVC cover is shown, it is not drawn to scale.

Figure 3.7 shows the transfer setup. The stamp holder is positioned to the right of the tube lens, while the target sample substrate is fixed onto a sample stage below the lens using PMMA. The sample stage also serves as a heating plate. Both the stamp holder and the sample stage are equipped with micrometer screws, allowing precise mechanical control.

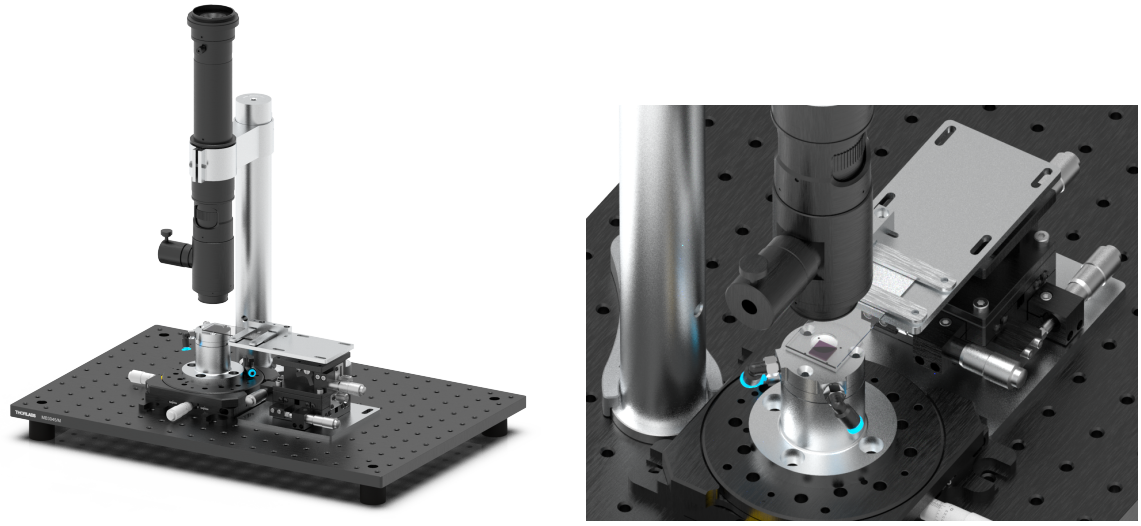

Figure 3.7.: Transfer setup for dry transfer of hBN flakes (left) and close up on its sample stage (right) [89]. The setup consists of three sections: tube lens with camera, sample stage XY micro-manipulator and stamp holder XYZ micro-manipulator.

The effectiveness of the transfer relies on the temperature-dependent contact force between the hBN flake and the PVC film. The pickup and drop off is illustrated in figure 3.8. At 70 °C, the PVC adheres strongly enough to pick up the hBN flake. At 120 °C, the van der Waals interaction between the hBN and the SiO_2 substrate exceeds the PVC contact force, enabling the flake to be released onto the substrate [88]. Once again, a clean contact surface should be maintained, for example, cleaning the stamp with IPA and the substrates with acetone prior to transfer. Dirt on surface affects the success of the transfer due to poor contact. The detailed fabrication recipe of the PDMS stamp and the transfer protocol is summarized in box "PDMS Microdome and dry transfer" in A.1.

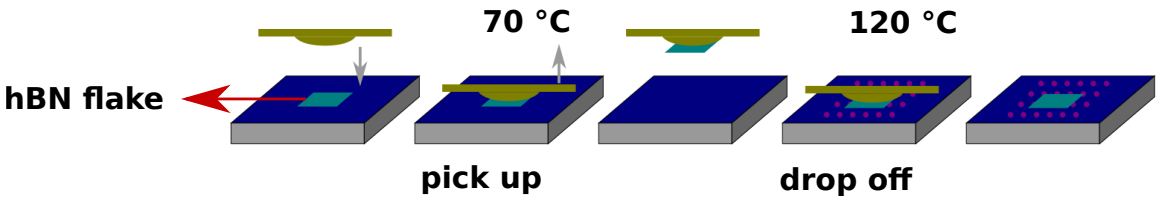

Figure 3.8.: From the left, the stamp is brought closer to the flake and picked up at 70 °C, after pickup the substrate is changed to target sample which is heated to 120 °C for placing the flake.

The smallest contact area between the stamp and the hBN flake is approximately 15 µm. This allows the transfer of relatively large flakes without the entire flake coming into contact with the PVC surface, thereby maintaining its cleanliness. Due to the rigidity of hBN flakes, they can extend over the edge of the chip and form cantilevered structures during transfer or positioning, without sagging or adhering to the rest of the microdome surface.

When the flake size approaches the stamp apex diameter, the entire flake may contact the PVC film thereby creating chances of contact contamination. The transfer setup allows full 3D manipulation, as illustrated in Appendix figure A.1. In this example, a 120 µm hBN flake was folded multiple times and still successfully picked up and transferred. Overall, this method enables micrometer-precision control over flake handling, including intentional cracking, encapsulation, and the transfer of both thin and thick hBN flakes. Using this approach, we have also successfully exfoliated thick flakes with PDMS stamps.

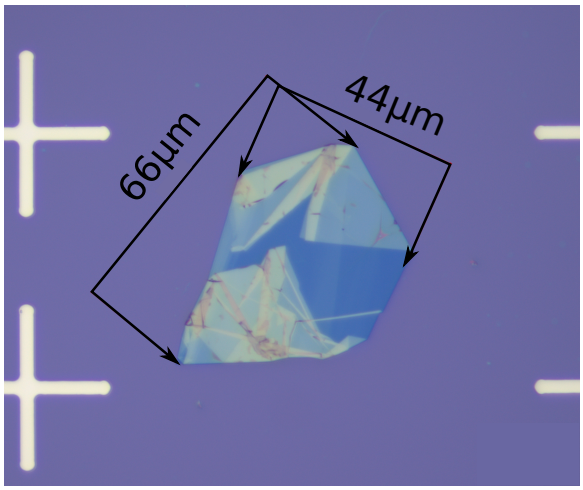

Figure 3.9.: hBN flake which has been folded several times as seen from the thicker (light green and orange colors) top and bottom sides of the flake using the 3D manipulation technique using microdome stamps. On the edge of the image are Platinum cross markers for directing around the substrate.

3.1.4. AFM Nanoindentation

After the flake has been transferred or exfoliated onto an annealing-compatible substrate, the substrate is cleaned again using acetone and IPA. To avoid displacing the flake, cleaning is performed by gently swirling the chip in the solvents, followed by careful nitrogen drying.

AFM topography scans and nanoindentation were performed using a Bruker Dimension Icon AFM, located in an ISO 8 cleanroom and mounted on an anti-vibration table.

I have always started with a higher set-point for the full flake scan and gradually went to lower setpoint values while optimizing the trace and retrace lines. Atomically flat structures (like hBN) needed to be scanned with a lower setpoint to get a scan a with a good trace and retrace signal. Tuning these parameters such as setpoint, integral gain and scan speed are key for accurate imaging of hBN. Also, these parameters become important in trying to get high resolution images of the indents made.

Pre-selected flakes are first scanned to inspect their thickness and surface topography. This characterization is done in tapping mode. If the flakes have bubbles or have too many adsorbates, they do not go further fabrication processes. When there is only minimal debris, then sections of the flake where indentation are to be made are scanned in AFM contact mode such that the tip pushes the debris outward. During contact mode scanning, a feedback setpoint voltage of 1 V was employed. Setting the voltage too low might allow surface contaminants to persist, whereas a higher voltage could lead to wrinkling from excess strain on the flake.

Figure 3.10 shows as an example of a flake region where strain was applied with an excess trigger voltage of 1.6 V during contact scanning. Consequent scans in tapping mode revealed wrinkling features as has been reported in other 2D materials such as MoS_2 and graphene [90, 91]. For flakes without any debris or adsorbates proceed to indentation without this extra cleaning step with contact mode AFM contact cleaning.

Each indentation corresponds to a force curve, where the tip presses into the sample and records its mechanical response. A force curve reflects the interaction between the tip and the sample during the approach and retraction cycle, providing insights into mechanical properties such as stiffness, elasticity, and adhesion. From the curve, one can extract parameters like indentation depth, contact point, and adhesion force. Since the objective here is to simply create indentations for crack formation and carbon contamination from the tip, the force–distance data were not further analyzed.

Typical indentations are approximately 2 nm deep and 35 nm wide, as shown in the Results section. Markers are placed within the scanned frame of the selected indentation region, with 1 µm or 1.5 µm spacing. This minimum spacing ensures that defects at the borders of adjacent indents remain separated by more than the confocal volume (260 nm), reducing the likelihood of multiple emitters overlapping and forming ensemble emission. The AFM nanoindentation procedure is summarized in colorbox titles "D. AFM nanoindentation" in A.1.

The tip needs to be changed multiple times depending on its requirements. The first tip which is an Al/BS tip is generally works quite well for tapping mode scans. However for indentation, we change the tip to a harder tip which is carbon coated, in hopes of facilitating carbon defects from the debris of the tip from indentation. This indenting tip becomes blunt after around 200 indents and fail to clearly see any indents formed. The resolution of a scan is limited by several factors. The lateral resolution is limited by the radius of the curvature of the AFM tip,

$$\delta \approx \sqrt{R \cdot h} \tag{3.3}$$

where δ is the lateral resolution limit, R is the tip radius and h is the height of the surface features. The vertical sensitivity Δz is defined as:

$$\Delta z = \sqrt{\frac{4k_b T}{3k}} \tag{3.4}$$

where k is the spring constant, Boltzmann factor $k_B = 1.38 \times 10^{-23} \frac{\mathrm{J}}{\mathrm{K}}$ and temperature T. Thus a high force constant, low thermal noise and a sharp tip with small r give higher resolution. And hence, in order to probe the indents size and depth we use a fresh AFM tip with less than 1 nm radius. As will be shown in results section 4.2, Tap 300 DLC, with 15 nm radius, is too blunt after indentations to make reliable scans.

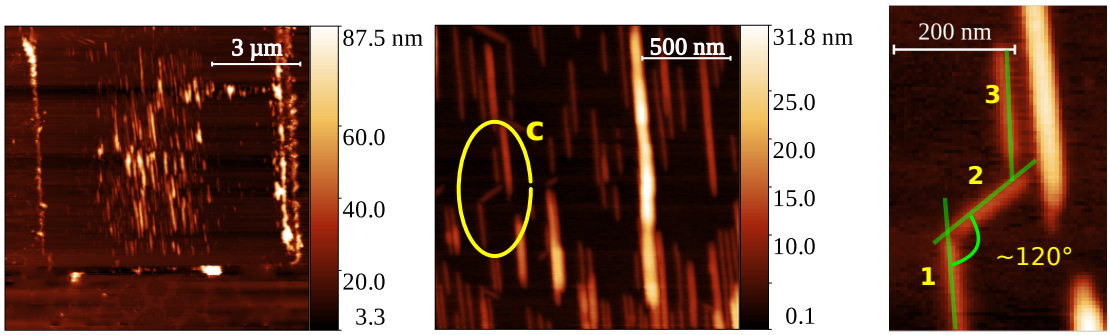

a. wrinkling in the centre

b. homogeneous lines perpendidular to strain

c. strain induced wrinkling

Figure 3.10.: Figure (a) shows AFM scan in tapping mode showing structures in the centre of the area which was scanned with a high contact scanning threshold voltage. b. shows a higher resolution of the structure showing uniform wrinkling perpendicular to the scanning direction. Figure (c) is the circled spot in figure (b), revealing that some structures correspond to the hBN lattice structure, 120 ° is the hexagonal ring edge angle.

The Point and Shoot program automates the process: the tip moves to each marker, engages, performs a force curve, retracts, and proceeds to the next point. The required trigger voltage depends on the flake thickness, as it defines the force at which the tip stops approaching and begins to retract. For flakes between 40 nm and 70 nm thick, a trigger voltage of 1.4 V typically yields successful indentations. We found 1.6 V to be optimal for achieving consistent and well-defined indentations. Higher trigger voltages lead to larger indent sizes. The retract time is 2 s, representing how long the tip takes to withdraw after reaching the trigger point. The dwell time, also set to 2 s, is the delay during which the tip remains in contact with the surface before retraction. Analysis on AFM nanoindentation results are discussed in further detail in Results, section 4.2.

3.1.5. Annealing

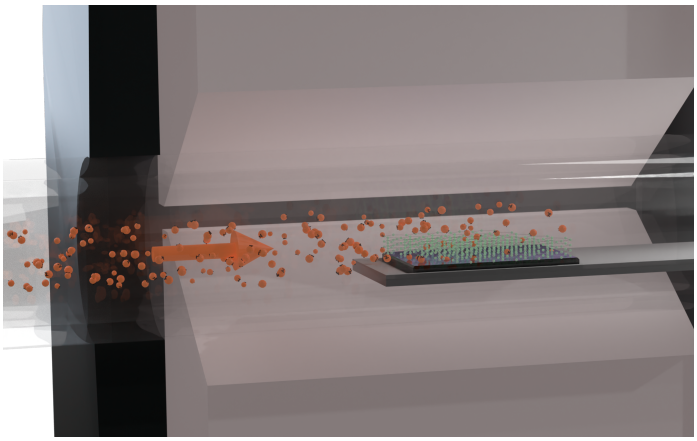

Figure 3.11.: Schematics of sample (green) placed on a quartz sample holder inside a quartz tube being annealed in an Ar flow (orange).

Defect activation in hBN requires high-temperature annealing [92, 93]. Figure 3.11 shows a schematic of the annealing setup, in which the substrate is placed inside a quartz tube connected to a mass flow controller on the left and vacuum pumps on the right. A photograph of the actual experimental setup is shown in figure 3.12.

The annealing is carried out using a Verder Scientific Carbolite Gero TS1-1200 ceramic furnace, capable of reaching temperatures up to 1200 °C. The furnace features programmable temperature ramping and naturally slow cooling to room temperature. Argon gas flow is regulated using a Vögtlin Instruments mass flow controller in combination with a TetraTec Instruments PCU10 unit. The vacuum system consists of an Edwards TIC Pumping Station, which includes both a scroll pump and a turbo-molecular pump. Between the furnace and the pumps, a pressure control valve is installed to allow precise pressure tuning during annealing.

A base vacuum of 2×10^{-5} mbar is first achieved before the annealing begins. The sample is then degassed at 400 °C for 15 min to 30 min until the pressure stabilizes. Following this, the temperature is ramped up to 1000 °C, the argon flow rate is set to 10 ml/min, and the turbo pump is turned off while the roughing pump remains active. The temperature ramp takes approximately 45 minutes. During this time, the pressure valve is adjusted to maintain a chamber pressure of 13 mbar or higher. The sample is annealed at 1000 °C for 30 minutes. After annealing, the oven, argon flow, and pump are switched off, and the system is allowed to cool down gradually in a closed argon environment. The ceramic furnace takes about 4 hours to reach 50 °C.

This standard annealing procedure was used for most samples. Some flakes were subjected to double annealing, with an initial treatment at 850 °C, which was found to be insufficient for stabilizing the emitters.

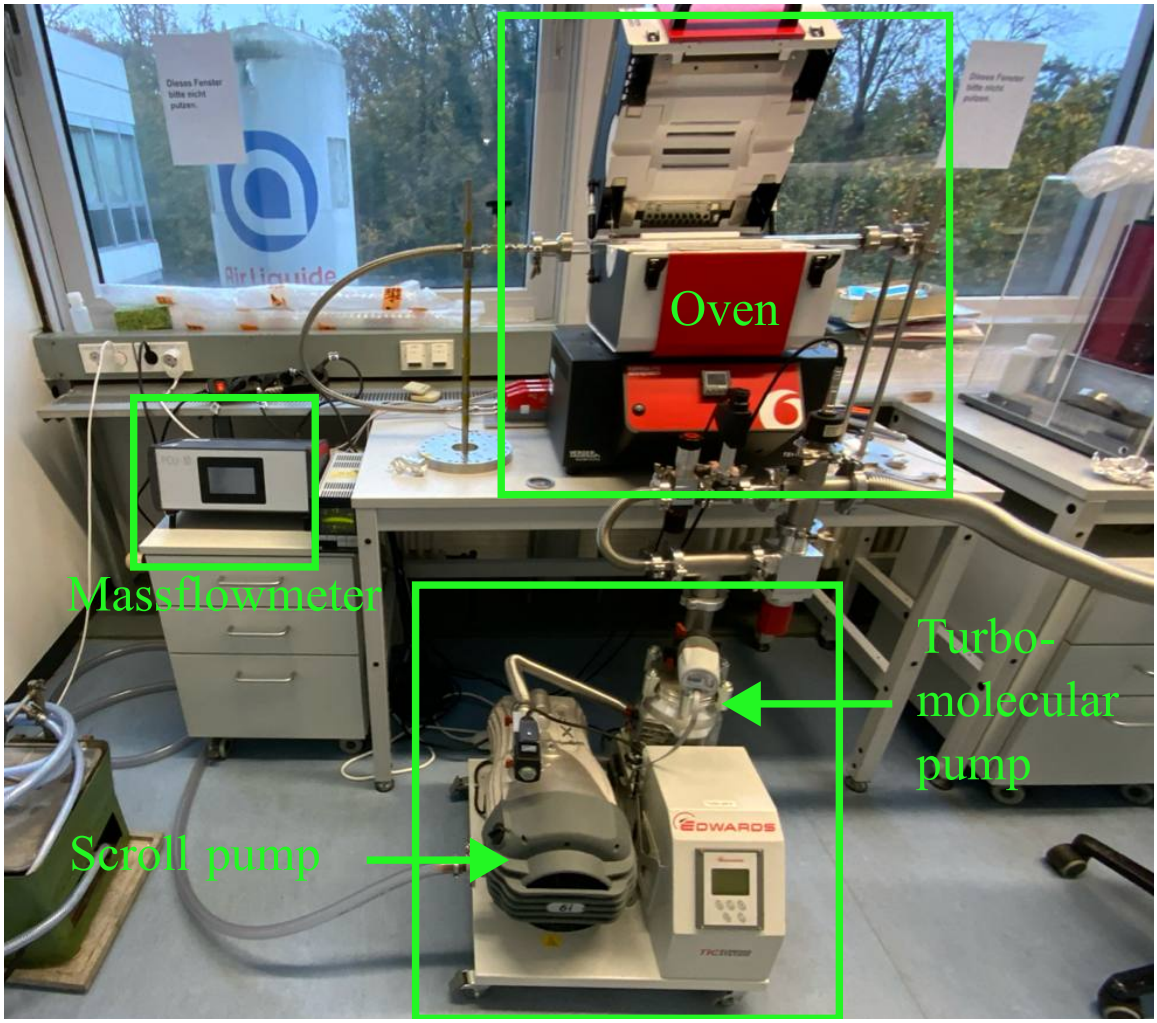

Figure 3.12.: The complete setup of high temperature annealing.

3.1.6. Coplanar Waveguide (CPW)

The lithographic recipe for fabricating the CPW is provided in the colorbox titled "CPW" in A.1. The CPW was designed by Ioannis Karapatzakis and consists of three parallel, equally spaced conducting lines patterned on the surface of the sample substrate. This geometry confines the microwave field between the signal line and the adjacent ground planes, ensuring that the field remains largely in-plane with the substrate. hBN flakes

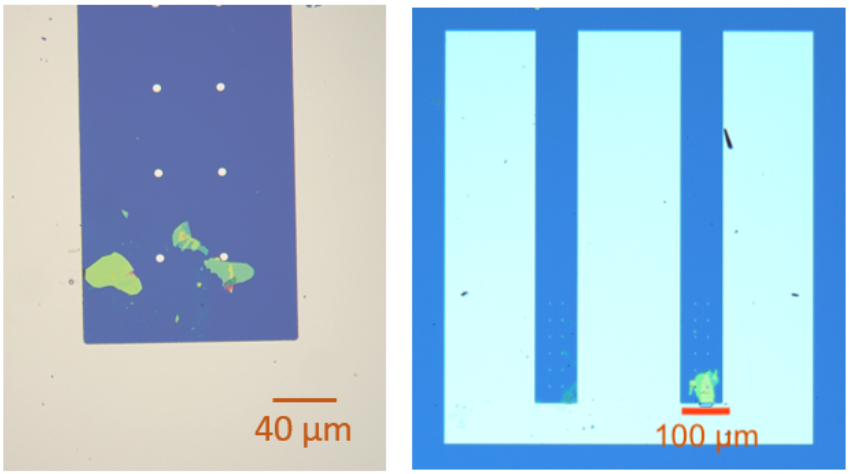

Figure 3.13.: Microscope image on the left shows hBN flakes (green) transferred on to a chip in between the CPW conducting lines. Image on the right shows the full view of an exemplary CPW.

are then positioned at the region of maximum microwave field concentration—near the central gap at the base of the CPW structure—as illustrated in Figure 3.13.

The conductors are made of platinum with a thickness of 100 nm, a spacing of 100 µm between the lines, a total length of 1000 µm, and a width of 890 µm. One of the key advantages of using a CPW is its ability to tightly confine the signal to the substrate surface, which enables efficient coupling to nearby quantum emitters. Additionally, when the structure is impedance-matched (typically to 50 Ω), it minimizes signal reflection and ensures low transmission loss across a broad range of microwave frequencies.

4. Results

The Results chapter is divided into nine sections. Section 4.1 presents the outcomes of various fabrication techniques that were explored, along with a discussion of their respective advantages and limitations. These efforts ultimately led to the development of our primary fabrication method—AFM nanoindentation—the results of which are introduced in Section 4.2. Section 4.3 examines the topographical changes in the hBN flakes induced by high-temperature annealing, a process that plays a critical role in emitter formation and quality. Sections 4.4, 4.5, and 4.6 assess the photophysical properties of the resulting SPEs, providing evidence of their stability, reproducibility, and spectral purity, and together addressing our first research question (see Figure 1). Section 4.7 investigates the interaction of the emitters with molecular adsorbates, while Section 4.8 evaluates their behavior under low-temperature conditions. Finally, the chapter concludes with Section4.9, which outlines the remaining challenges associated with working with quantum emitters in hBN.

4.1. Fabrication techniques

Before choosing AFM nanoindentation as our primary fabrication method, we experimented with a variety of other more commonly used techniques. As this section will show, compared to AFM nanoindentation the yield of stable single isolated SPEs was not as abundant. Despite the success of these fabrication methods in producing single photon emitters, the emitters often lack stability and, in certain instances, mainly consist of ensembles. The stability of these emitters might be enhanced by refining the annealing and exfoliation parameters. However, even then, what sets AFM nanoindentation apart is that, this fabrication technique creates emitters which are spatially and spectrally deterministic as will be shown in the following sections. The emitters from AFM nanoindentation stay stable for a long period of time. In addition, the SPEs from AFM nanoindentation are robust against dry transfer with a microdome stamp (section 3.1.3) which involves coming

into direct contact with the emitter. These are all criteria that fit our requirements for an ideal sample.

This chapter offers an overview of these various techniques alongside their outcomes: FIB, RIE, ICP RIE, liquid exfoliation, and sputtered carbon on hBN flakes. Each method is assessed to explain why they were not selected as the main fabrication approach. This section presents valuable insights from fluorescence and spectral properties of the emitters, which help guide the direction for optimal fabrication technique.

The fluorescence images are taken with room temperature confocal setup, explained in section A.4, with less than 100 µW power of green laser. The spectra are recorded with one minute integration time.

The smallest detectable region in a confocal microscope is limited by the confocal volume, which is governed by the optical resolution of the system. Based on the Rayleigh criterion for point sources, the lateral and axial resolution limits are given by:

$$\begin{aligned} \Delta r &= \frac{0.44\lambda}{n\sin(\theta)} \\ \Delta z &= \frac{1.5n\lambda}{(NA)^2} \end{aligned} \tag{4.1}$$

where λ is the excitation wavelength, n is the refractive index of the medium (assumed to be 1 for air), θ is the half-angle of the objective's aperture, and $NA = n\sin(\theta)$ is the numerical aperture. In our system, we use an objective with $NA = 0.9$ and an excitation wavelength of $\lambda = 532\,\text{nm}$, which yields:

$$\Delta r = 260\,\text{nm}, \quad \Delta z = 985\,\text{nm}$$

These values define the lateral and axial dimensions of the confocal detection region, within which both excitation and collection are optimized for spatially resolved single-photon emission.

An SPE, which is effectively a point source of light (like a tiny dipole), typically appears with a Gaussian spatial intensity profile, and its brightness is confined to this focal volume of the objective lens. This behavior arises from the diffraction-limited nature of optical focusing, which results in a point spread function (PSF) that closely resembles a Gaussian distribution in both lateral and axial directions. When scanning across an SPE, the detected

fluorescence intensity peaks when the emitter is aligned with the focal point and gradually decreases away from it, producing a Gaussian-shaped brightness map.

Thus in the fluorescence images on hBN flakes, bright Gaussian-distributed spots limiting brightness to 260 nm are checked for antibunching behaviour to confirm their quantum nature. If a point source is much bigger than 250 nm, they are most likely to be dirt or other sources of photoluminescence on the sample surface.

When doing a large confocal scan on the entire flake, a resolution pixel size of 250 nm is enough to detect possible SPEs on the substrate. The bright points are then scanned individually with 100 nm resolution in 2 µm × 2 µm size to locate the bright centre of the emitter and the Z scan is taken to optimize the Z focal point. For the XY scan the piezo moves in the X and Y axis collecting fluorescence data in a given fixed Z point. For the Z scan the piezo moves in the X or Y while changing Z piezo while keeping Y or X fixed respectively. Positioned at the centre of the gaussian in the the XY confocal scan of the emitter and the appropriate Z focal point, the HBT experiment is carried out to confirm single photon emission, for more information on HBT experiment see sections 2.2.3 and A.4. A flip mirror is used to change light path from the APDs to the spectrometer where the spectra is collected with one minute of integration time.

4.1.1. Focused Ion Beam

FIB is a precise nanofabrication and characterization technique that employs a finely focused beam of energetic ions (Ga^+)—to enable site-specific material modification, removal, and analysis at sub-micrometer to nanometer length scales. Operating on principles analogous to those of a scanning electron microscope (SEM), FIB systems utilize ion–solid interactions to induce localized sputtering, implantation, or amorphization of the target material. The FIB patterns were done in dots with 1 µm spacing and a dose of 0.02 s/d on 12 flakes. The dose gives the exposure time for each pixel spot which is 20 ms. The ion dose (C/cm^2) can be calculated $\text{Dose} = \frac{I \times t}{A}$, where I is the ion beam current (A), t is the total dwell time (s), and A is the area (cm^2). The dose is set by the system used for FIB. The flakes were annealed in Ar at 850 °C after FIB patterning.

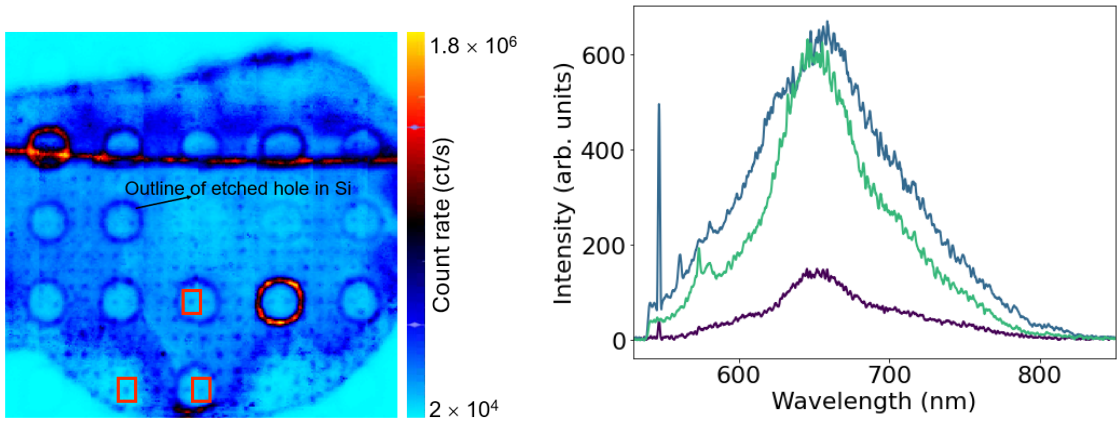

Figure 4.1.: (a) FIB pattern on a suspended hBN flake. The larger circles edged with higher counts correspond to etched holes in Si, and the smaller dark blue spots on the flake are FIB-exposed regions, though not all produce SPEs. Scan size: x × y = 25 µm × 24 µm Spectral data from the regions marked with a red rectangle are shown in (b). (b) Spectra showing a sharp Si Raman peak at 547 nm and broad peak around 650 nm, a feature often observed in FIB-exposed spots.

Figure 4.1a shows fluorescence scan of region of a flake which has been patterned with FIB. The FIB exposed pattern is clearly visible in deterministic spots with higher photon count rate, however most of these spots did not show any anti-bunching dips in HBT experiment, meaning they were not quantum emitters but rather bright spots on the flake.

The PL spectra of the three FIB spots on suspended region on the flake in 4.1a which are marked in red rectangles is given in figure 4.1b. As seen on figure 4.1b the spectra are broad and are not the characteristic spectral shape belonging to quantum emitters in hBN [10]. The sharp peaks around 547 nm are Si Raman peak observed in all our spectral data in this work generates from our Si substrate. The intensity of the Si Raman is depended on the thickness of the hBN flake, thicker flakes would give a weaker Si Raman. The PL spectra show low intensity characteristic of ensemble photoluminescent particles within the confocal volume (see figure 4.18) . High energy Ga^+ ions can result is broad photoluminescence peaks owing to amorphized regions, vacancies, or substrate debris. These luminescent centers are often broad and unstable, distinguishing them from true SPEs [25]. There were SPEs found on the line crack on the flake on the top region of the flake which might be resulting from natural defects in hBN. The yield of SPE resulting from the FIB patterned spots themselves were therefore low and the emitters found on this FIB exposed sample were mostly blinking.

Similar work with FIB to produce SPE on hBN [94] investigated how high-energy Ga^+ focused ion beam (FIB) milling affects the morphology of hexagonal boron nitride (hBN)

and its ability to host stable, room-temperature single-photon emitters (SPEs). They reported stable and bright emitters with no particular reference to the number of total yield of the SPE except for being referred to as 'non-zero' SPE yield. However, they annealed the samples in a carbon rich environment after the FIB exposure at 1000 °C which is a standalone method for creating quantum emitters[95]. This makes it uncertain whether the stable SPE were generated by the FIB process, or if the carbon-rich atmosphere was the significant factor in their formation. From our results from FIB, it is indicative that FIB accompanied by annealing in an inert environment does not produce a reasonable yield of high quality stable quantum emitters; and that, the presence of carbon in the fabrication steps to create single isolated bright SPE has a certain positive influence. The last statement will be repeatedly demonstrated and established from all the fabrication methods examined in this work.

4.1.2. Reactive Ion Etching

In RIE, a low-pressure gas mixture is ionized in a radio-frequency-powered chamber, generating reactive ions and neutral species that simultaneously engage in physical sputtering and chemical reactions at the surface. The gas mixture we have used for etching hBN is CHF_3 and O_2. The entire sample was exposed to the etchant followed by Ar annealing at 850 °C.

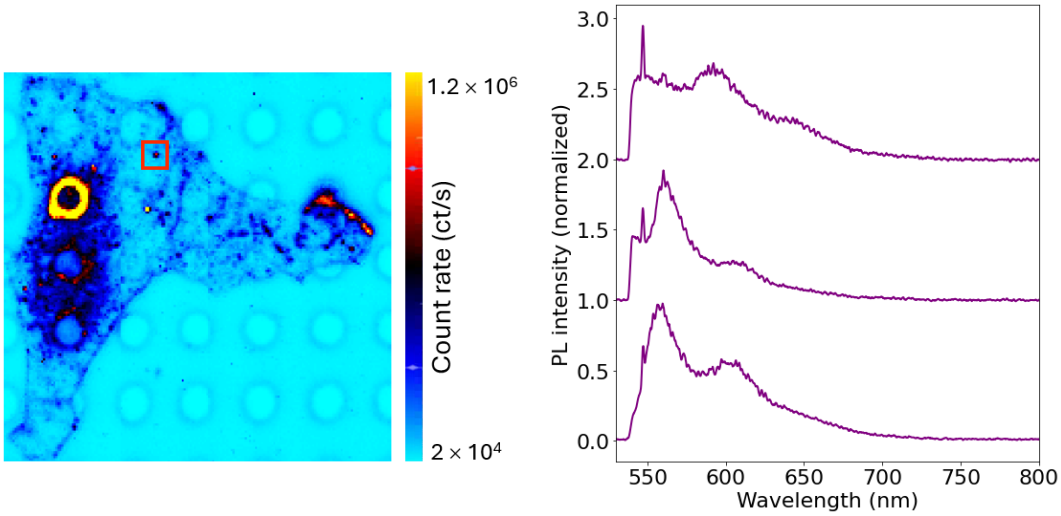

Figure 4.2.: (a) Fluorescence map of a suspended hBN flake after RIE and annealing, showing many optically active defects. Scan size: x × y = 32 µm × 27 µm. Edges and cracks exhibit higher fluorescence count rate, aiding defect retracing. (b) Exemplary spectrum of emitters created using CHF_3 etching, showing broad linewidths and low spectral counts due to instability.

Figure 4.2a shows typical fluorescence features of emitters on an hBN flake fabricated using RIE. The figure shows that SPEs are distributed across the flake surface with no evident spatial preference. Many of the bright spots—such as the one highlighted by a red rectangle—exhibit antibunching behavior, confirming single-photon emission. The yield of SPEs in these samples was higher than that obtained from FIB processing. However, the emitters typically exhibited blinking. The fluorescence image shows that the background count of SiO_2 substrate and the hBN flake is generally no more than 20 kcts/s to 25 kcts/s and SPE typically reaching several hundred kilo counts per second to over a million counts per second, covering only a few pixels in this image which has a resolution is 212 nm per pixel.

With measurement steps and reasoning explained in the beginning of this chapter we confirm that as seen in figure 4.2a, the spot inside the red rectangle and other similar

spots have been confirmed to be an SPE, albeit most of them were blinking. Figure 4.2b presents three representative photoluminescence spectra from different emitter locations on RIE-processed flakes which showed antibunching. They are normalized and have one unit spacing to show individual shapes more clearly. They have ZPLs in the range between 550 nm to 620 nm. They exhibited broad linewidths and with strong first PSB (section 2.3.1 for definition). Other research groups have already reported SPE spectra to have narrow linewidth with high DW factor [48] and hence we deduced the results from RIE to be lacking. The instability and poor spectral quality make the RIE-generated emitters unsuitable for our purposes.

Notably, SPEs were generally absent from the central suspended regions of the flake over the etched holes and were observed only near the edges of the holes which create strain. Additionally, detecting emitters in the suspended region is more challenging due to reduced photon collection contrast.

With RIE fabrication method, there is no deterministic formation of patterns on hBN, similar to that seen in FIB. However, patterning is also possible using RIE: it requires electron beam lithography with PMMA (Polymethylmethacrylate) as a photoresist. In addition to RIE we also tried patterned RIE. Substrate is coated with PMMA, exposed to e-beam for lithography, and developed of the PMMA the sample was exposed to etchant gases for RIE. However, residual PMMA on the surface proved to be a persistent contaminant which was difficult to completely remove during the lift-off process. The results obtained from patterned RIE were not sufficiently promising for detailed presentation in this work. From patterned RIE it was obvious that PMMA residues and other hydrocarbon byproducts which persist—post annealing—lead to unstable SPEs.

4.1.3. Inductively-Coupled Plasma Reactive Ion Etching

In ICP-RIE, a high-power RF coil inductively generates a dense plasma of reactive species (radicals and ions) from feed gases such as SF_6, CHF_3, O_2, or Cl_2. Simultaneously, a separate RF bias applied to the substrate electrode accelerates ions toward the surface, enhancing physical sputtering and anisotropic etching. This decoupled control over plasma density and ion energy allows for higher etch rates than normal RIE, excellent sidewall profiles, and minimal damage to sensitive materials. A mixture of gases with CH_4: Ar: H_2 = (20: 4: 8) ml/min ratio, with 100 HV was used for 1 min for the fabricating emitters. This was followed by annealing in Ar flow at 850 °C. One of the flakes from this batch of etching showed some stable isolated single photon emitters with ZPL peaks around 625 nm and also many ensembles. These exemplary spectra of emitters from this sample are shown in figure 4.3. They are normalized and have one unit spacing to show individual spectral shapes more clearly. The sample exhibited emitters in the 580 nm to 650 nm range. The second and third spectra are exemplary of what we are looking for in our emitters, high ZPL:PSB intensity, isolated and a narrow linewidth at RTP, our goal has been to find a fabrication technique that will reproduce a high yield of such emitter that are reproducible. Although this fabrication technique was not extensively optimized, it already yielded more promising results on the first attempt than those obtained using FIB or global RIE. The superior performance compared to FIB may be attributed to hBN's energetically favorable interaction with carbon-related defects originating from CH_4. In high plasma environments, methane dissociates into various hydrocarbon radicals such as CH_3, CH_2, CH, and C.

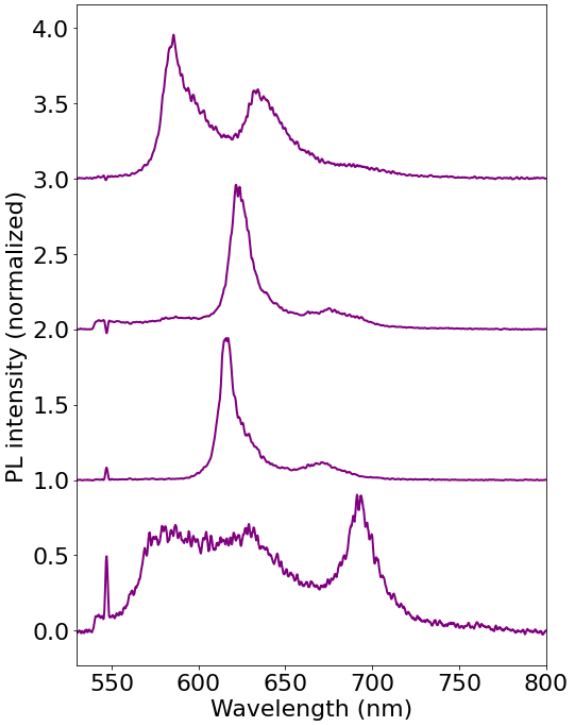

Figure 4.3.: Shows spectra of three different emitters, two of them at around 625 nm have comparatively sharper ZPL, the dark purple spectrum is less bright and has a stronger PSB weight (at 630 nm) than the other two emitters.

Nonetheless, all three methods FIB, RIE and ICP-RIE produced a high number of blinking emitters, likely due to charge buildup during ion bombardment. Since the sample is insulating, exposure to positive ions can lead to surface charge accumulation, resulting in a positive surface potential. Such charge buildup affects the emitters' stability, leading to blinking or bleaching behavior [83].

4.1.4. Liquid Exfoliation

For liquid exfoliation, ultra-fine hBN powder is ultra-sonicated in an isopropanol (IPA) solution to form nanosheets suitable for drop-casting onto a Si substrate [89]. For the preparation of the following sample, the hBN–IPA solution was drop-cast onto a Si substrate placed on a hot plate at 100 °C to prevent aggregation of the nanosheets into larger crystals.

A key challenge when working with liquid-exfoliated hBN is that, unlike mechanically exfoliated flakes, it is difficult to relocate and identify the same emitter unless micrometer-scale alignment markers are densely distributed across the substrate (figure 4.5). In contrast to fabrication methods previously mentioned, the Si substrate used here is not patterned with etched holes. While this fabrication method is fast and straightforward, it results in emitters randomly distributed across the entire chip, making detection and selection of high-quality emitters non-deterministic and labor-intensive.

Emitters in exfoliated multilayer flakes have the advantage of reduced substrate interaction, which facilitates easier transfer and device integration. On the other hand, emitters formed in liquid-exfoliated samples are typically mono- or few-layer hBN, which exhibit stronger interaction with the substrate due to their low lateral-to-thickness aspect ratio. As a result, after high-temperature annealing (>850 °C), they are more difficult to transfer for chip-device integration compared to multilayer flakes, which are easier to locate, measure, and manipulate.

Figures 4.4a and 4.4b show representative spectra from liquid-exfoliated hBN samples. Bright and spectrally sharp single-photon emission features, such as the one shown in Figure 4.4a, are occasionally observed. However, most emitters exhibit sharp but low-intensity zero-phonon lines (ZPLs) on top of a broader background, as seen in Figure 4.4b, which might be ensemble of SPEs close to each other. The spectrum in Figure 4.4b is characteristic of ensemble of emitters we have seen in other sample sets (figure 4.18). Here too, they are normalized and have one unit spacing to show individual spectral shapes more clearly. This behavior is consistent with strong emitter–substrate coupling expected for monolayers. We have observed that multilayer hBN flakes—typically 40 nm or thicker—tend to host more stable emitters than mono- or few-layer counterparts. The sharp peak observed in Figure 4.4a may originate from aggregated nanosheet regions behaving as effective multilayers. While monolayer hBN, with its atomically smooth surface, is highly desirable for 2D device integration, multilayer hBN can provide enhanced emitter stability, possibly due to interlayer shielding that mitigates photobleaching [96].

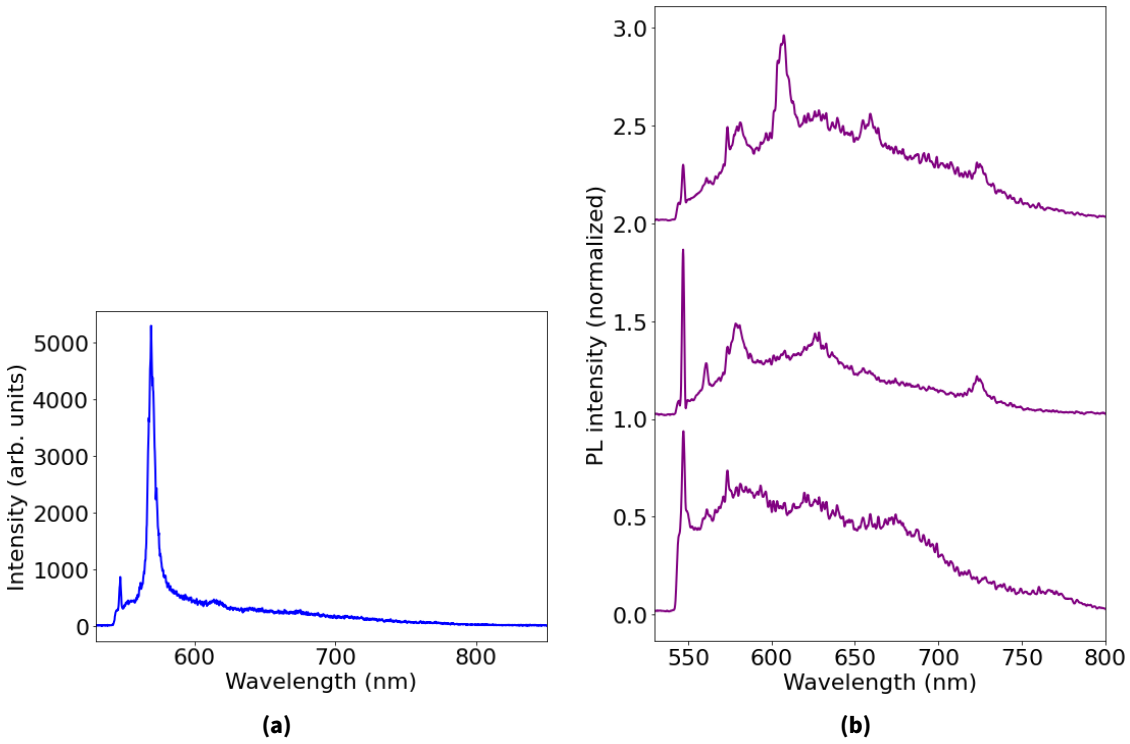

Figure 4.4.: (a) The sharp line shows the ZPL of an SPE from liquid exfoliated hBN; a weak PSB is present at around 610 nm. (b) Ensemble SPEs with multiple peaks, the strongest around 612 nm. The sharp peak at 547 nm is the Si Raman line.

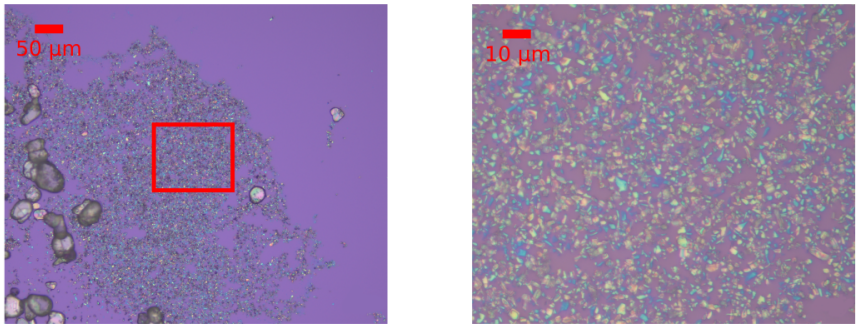

Figure 4.5.: Optical image of liquid exfoliated hBN nanosheets. The right panel shows a zoomed-in view of the region highlighted by the red rectangle in the left image. In confocal microscopy, it is difficult to find back and pinpoint the location of an emitter which has been studied earlier. This is not the case for emitters on exfoliated flakes.

4.1.5. Sputtered Carbon

For sample preparation, multilayer exfoliated flakes on Si were sputtered with carbon and subsequently annealed at 1000 °C in an Ar flow. Three sets of carbon sputtered samples were analyzed which had varying concentrations. The first set (Figure 4.6a), 0.02 Å of carbon was deposited in a high-vacuum using magnetron sputtering with a base pressure of 3×10^{-6} mbar and a sputtering pressure of 5×10^{3} mbar. Given that graphene has a monolayer thickness of 3.35 Å [97], the deposited carbon corresponds to coverage of 0.6% of a monolayer.

Flake 1 was exfoliated from hBN single crystals, which possess higher crystalline purity than the powdered crystals. Powdered crystals were used in the fabrication techniques mentioned earlier such as FIB, RIE, and ICP. As a result, single-crystal flakes generally exhibit a lower density of naturally occurring defects and thus show a reduced yield of emitters following fabrication. In the confocal scan of the flake#1 after annealing in 4.6a , the flake's center contains no observable defects, and the confirmed single-photon emitters (SPEs) appear only near the edges following carbon deposition and annealing. Without any fabrication processes, these flakes exhibit low fluorescence counts even at the edges. Spectral features of several emitters located along the flake's edge are presented in Figure 4.6b. During annealing, defects tend to migrate toward cracks and edges. Elevated temperatures facilitate atomic mobility and rearrangement, enabling defects to diffuse into lower-energy sites such as surfaces or edges [98]. The spectra are normalized and have one unit spacing to show individual shapes more clearly. The low coverage of carbon, only 0.6 % of a monolayer, although produced stable isolated emitters, in order to have a higher yield we deposited more carbon on our next batch.

For the second sample set (figure 4.8a), 2.4 Å of carbon was deposited, corresponding to approximately 78% of a monolayer coverage. This concentration was likely too much for having isolated emitters. At annealing the flake showing heavy etching, as shown in the optical image in 4.7a. Large holes are visible are visible on the green flake and some flakes and partial regions of flakes were etched and blown away during Argon annealing. Etching effects are discussed further in section 4.3. Contaminants and defects in hBN show to facilitate etching effects. Figure 4.7b show that from this sample batch mostly ensemble emitters spectra were obtained. The spectra are normalized and have one unit spacing to show individual spectral shapes more clearly. The top two spectra look like an isolated emitter, this particular ZPL line in higher wavelengths near 700 nm have been observed in heavily etched samples which in section (4.5) will be referred to as class D. Not much is

explored in this work as to the origin of this defect. We only comment on its presence from our experimental observations.

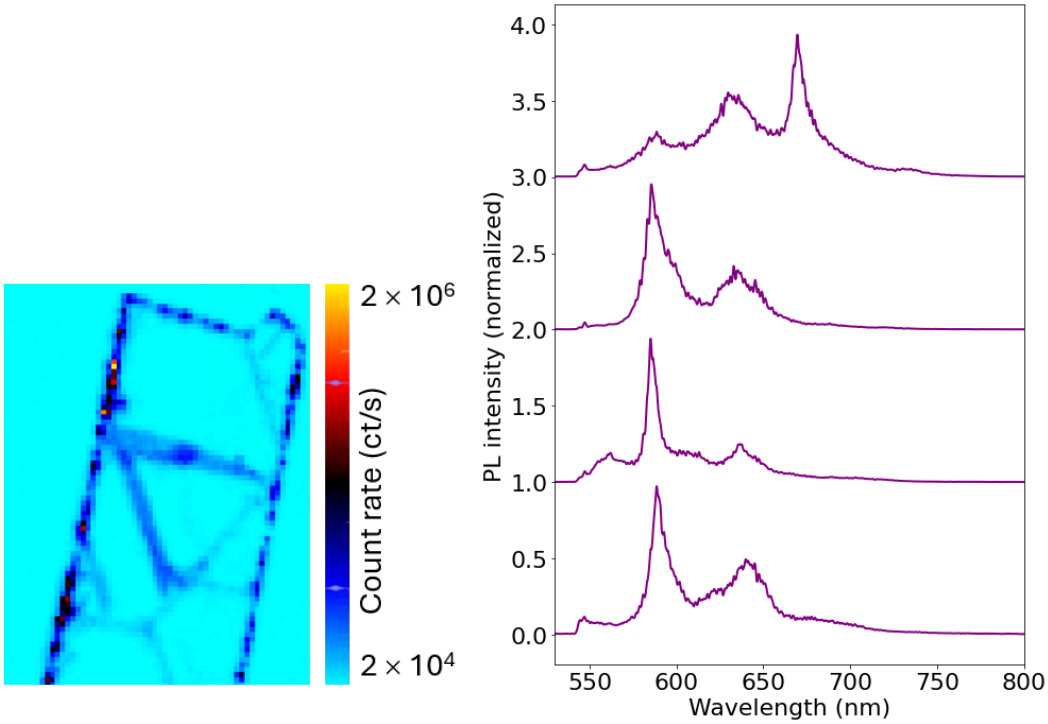

Figure 4.6.: (a) Fluorescence image of a single crystal flake after 18 % of a monolayer of carbon was sputtered and annealed at 1000 °C. Scan size: x × y = 16 µm × 20 µm. Emitters are visible around the flake edges. (b) Spectral properties of the same sample, showing several isolated single-photon emitters with sharp ZPLs.

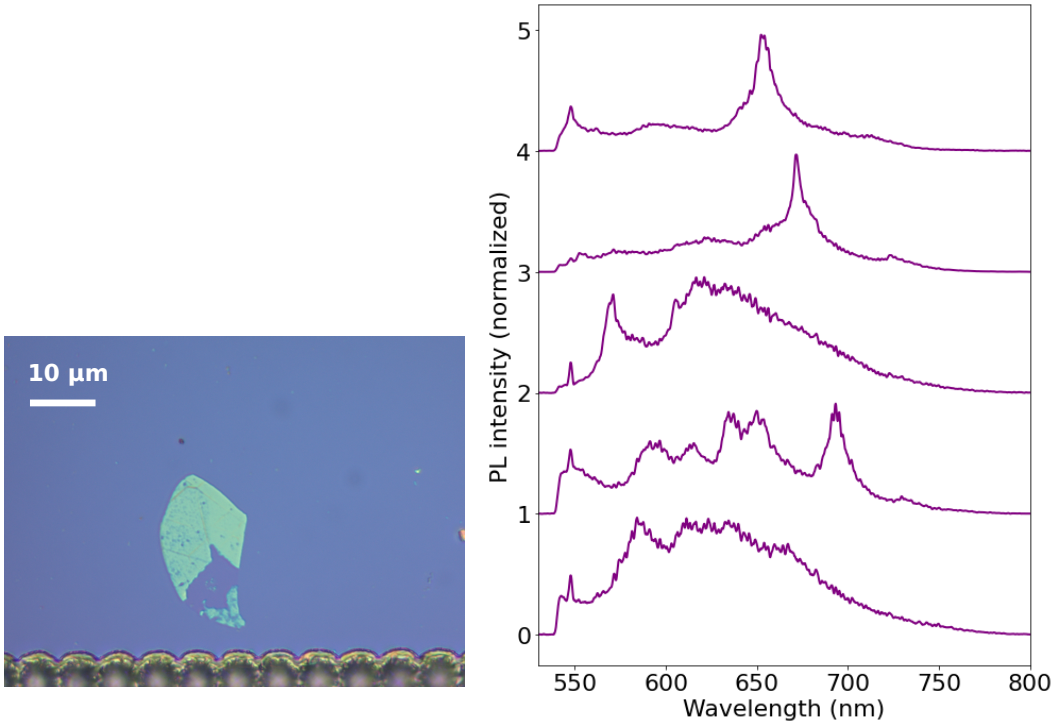

Figure 4.7.: (a) Exemplary optical image of flake after 2.6 Å carbon sputtering and annealing showing heavy etching. (b) Emitters in higher coverage carbon sputtered sample showing formation of ensemble emitters.

Thus the last set was optimized for a lower carbon concentration with 1.6 Å deposition (48% of a monolayer), followed by 1000 °C annealing in Ar flow, showed a high density of emitters. Figures 4.8a and 4.8b show the fluorescence and spectral properties of the emitters from this sample set. Although several of the emitters were blinking, owing to the high yield, a lot of stable emitters could also be found. Figure 4.8b shows better spectral features, compared to emitters in FIB or RIE emitters, for example narrower emission lines and isolated SPEs, and a definite higher yield. As you can see, some are ensembles in addition to single isolated emitters. A higher coverage of carbon leads to extended etching when annealing, thus creating a rough surface topography. This leads to ensembles and instability in emitters. Therefore a deposition coverage of carbon which creates a good yield of emitters but not too high to be creating too many ensembles is ideal.

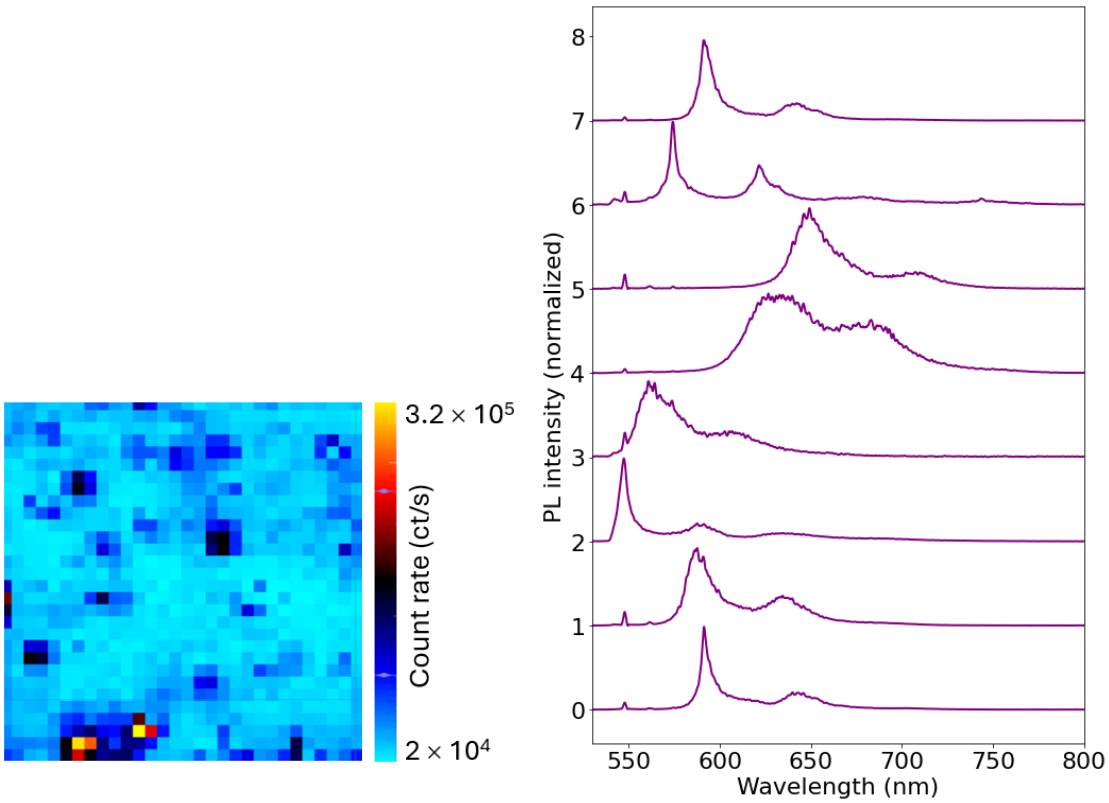

Figure 4.8.: (a) Fluorescence image of emitters on the hBN flake after 1.6 Å (48% of a monolayer) of sputtered carbon and annealing. This is a 4 µm × 4 µm region of a flake. The brightest emitters in this region reach up to 320 kct/s. (b) Spectral features of emitters from the same sample. Emission at lower wavelengths around 540 nm is also observed.

Once again, although this method can quickly help fabricate stable emitters, there are downsides to this fabrication technique which might not make it suitable for chip device integration. First of all, the emitters are not deterministic and thus a higher likelihood of having clusters of closely placed emitters within a confocal volume. Multiple emitters are excited simultaneously and can interact and effect each others' photophysical and electrical properties. Although this is not a stumbling block, when the goal is to only study the properties of these emitters. However, in the long run of using these emitters as spin sensors, it is required for them to be single isolated and well delocalized from its surrounding to have minimum instabilities. The other problem is that after carbon sputtering the flake cannot be transferred effectively. The contact force between the stamp and flake is reduced due to the carbon debris on top which hinders the transfer method.

From results of emitters formed from ICP RIE with CH_4 etching agent and carbon sputtering, it is shown that carbon related defects result in emitters with characteristic high ZPL

to PSB ratio, i.e high Debye Waller factor. This means that the electron-phonon coupling is less compared to emitters with a strong phonon side band. And theoretical studies have shown many carbon related defects to be spin active our fabrication toward having stable isolated single photon emitters which are spin active and transferrable have motivated our fabrication techniques with AFM nanoindentation.

An additional important note on the fabrication techniques used in this chapter, before moving to the next section, is the annealing temperature used. FIB, RIE, ICP and liquid exfoliation were annealed at 850 °C whereas carbon sputtered samples were annealed at 1000 °C. Which may indicate that perhaps the other techniques if annealed at a higher temperature may produce a higher yield of stable emitters although not deterministic.

4.2. AFM Nanoindentation

The analysis conducted on the samples created with this fabrication technique yielded several significant findings that directly address the research questions outlined in the introduction. First of all, I will present how the fabrication technique successfully produces SPEs in a deterministic manner. In the sections that follow we present the following results:

1. Topography of the hBN affected by this fabrication technique.
2. Fluorescence measurements showing deterministic creation of high quality stable SPE.
3. Spectral analysis showing tailored creation of a defect class.
4. Effect of molecules on top of hBN SPE.
5. Spectral analysis at 50 mK with resonant excitation and external magnetic field

Each measurement was conducted with the aim of gaining deeper insight into the defect type of the emitters and their electronic energy level structure. Our results establish that the local environment of the atomic defect plays a crucial role in determining the properties of the single-photon emitter (SPE). To address this, our fabrication technique is designed to produce a clean surface with minimal surface adsorbates following mechanical exfoliation. However, contaminants originating from the tape adhesive can remain on the flakes, and air bubbles may become trapped beneath or between the layers. These surface impurities can be effectively removed using contact-mode AFM scanning. This technique displaces the adsorbates laterally, resulting in a scanned area with picometer-scale surface roughness.

In scenarios involving bubbles, it is advisable to refrain from continuing the fabrication process with a flake containing bubbles, as this has been observed to result in unstable SPEs and cannot be easily removed by contact cleaning. Moreover, locating the indentation sites on flakes with bubbles has proven to be challenging. Figure 4.9 illustrates that mechanical transfer effectively eliminates bubbles from flakes. During transfer, the microdome presses into the flake removing any air trapped inter-layer or between the flake and the substrate. The darker spots on the flake before the transfer are trapped air bubbles. Their presence makes any defect present in their vicinity prone instabilities and high background counts.

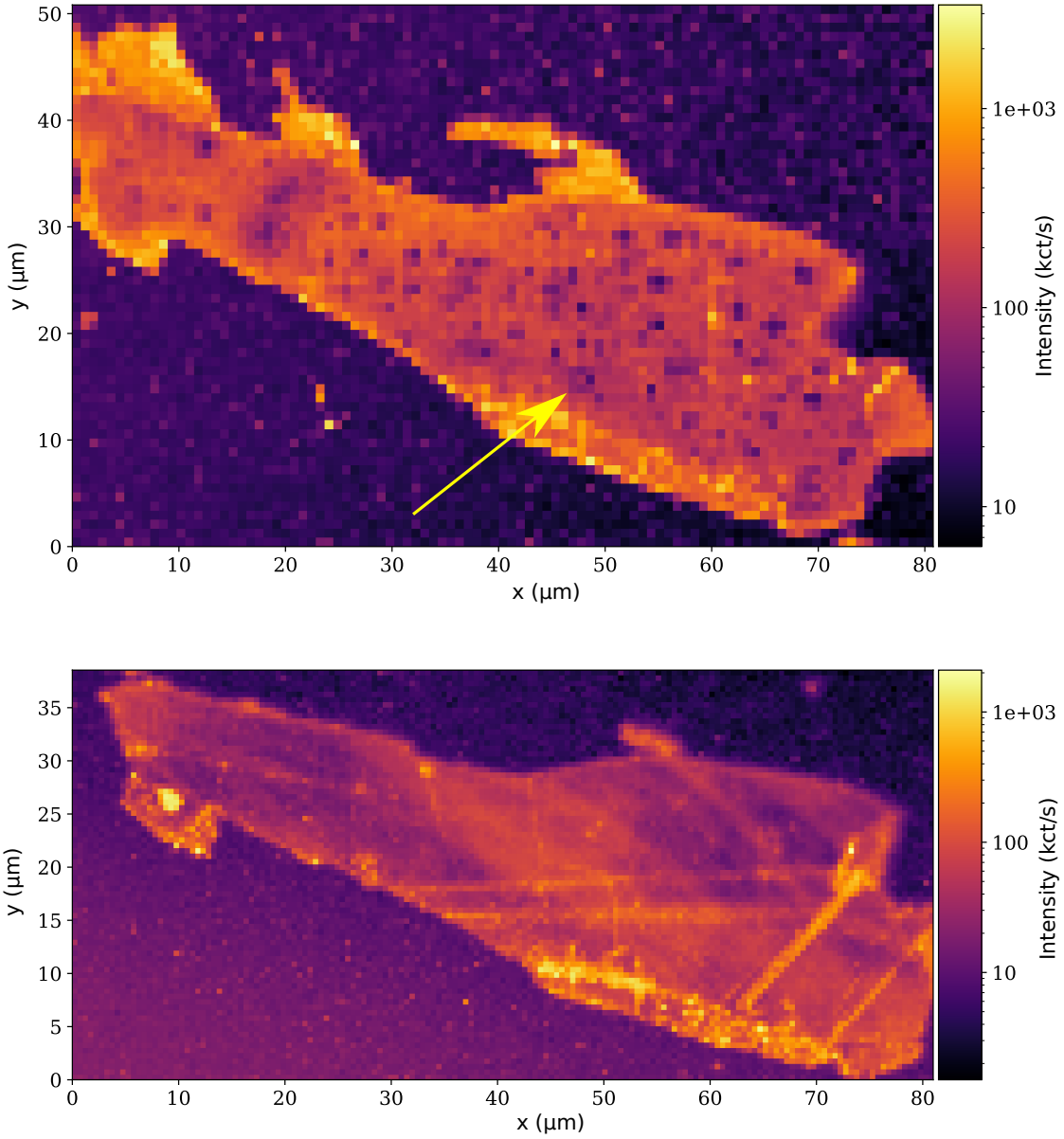

Figure 4.9.: Trapped air bubbles seen as darker counts are removed by 3D manipulation of the flake using our transfer technique. Top image is of the flake before transfer. The yellow arrow points to one of the bubbles referred to, they are present all over the flake. Bottom image shows flake after transfer with the darker micrometer sized circles (bubbles) removed.

After confirming the thickness and a clean surface topography of the chosen flakes, the AFM tip is changed to Tap300 DLC for AFM nanoindentation (detailed method description is given in 3.1.4 and A.1) . This fabrication technique has previously been demonstrated by Xu et al [99]. However, there are important differences in our approach and the goals in our sample fabrication. In their work, they studied how the yield of emitters depended

on the size of the indents made on 25 nm thick flakes. The indents were made completely through the flake, making the substrate visible. In contrast, we used thicker flakes, typically around 40 nm or more, and made only surface indentations, with the goal of creating more isolated single emitters than ensembles. Our results showed a more spectrally deterministic formation of emitters.

Figure 4.10 depicts a series of indents formed on a multilayer hBN flake with 40 nm thickness and their topographical changes. The scanning direction, trace and retrace is along the horizontal (x-axis) of the AFM scans shows in figure 4.10(a), (b), (c), (d), (e) and (h). The direction of indentation is perpendicular to the scanning path, that is, along the y axis. The indentation array exhibits an average height of approximately 7.69 nm, though indent heights can measure as high as 20 nm. This 'height' comes from the debris formed around the indent from tearing of the hBN flake and breakdown of the tip as will be discussed shortly.

Indentation was achievable on flakes with thicknesses as high as 150 nm. The color bar on each AFM scan data in this work represents the height profile. It shows the highest and lowest Z value in nm with respect to the surface of the hBN surface plane which has been set to 0. Detailed analysis of the indents using a high-resolution AFM tip with a radius of less than 1 nm reveals the shape of debris surrounding each indent as shown in 4.10(b), 4.10(c), 4.10(d) and 4.10(e). Despite same indentation settings as explained in 3.1.4, the debris pattern around each perforation differs. Debris accumulates on the upper and lower sides of indents in 4.10(b) and 4.10(c), likely due to the AFM tip's reciprocal motion during the indentation process. Conversely, variations in debris morphology are observed in 4.10(d) and 4.10(e), underscoring material response heterogeneity despite consistent parameters and indentation angles.

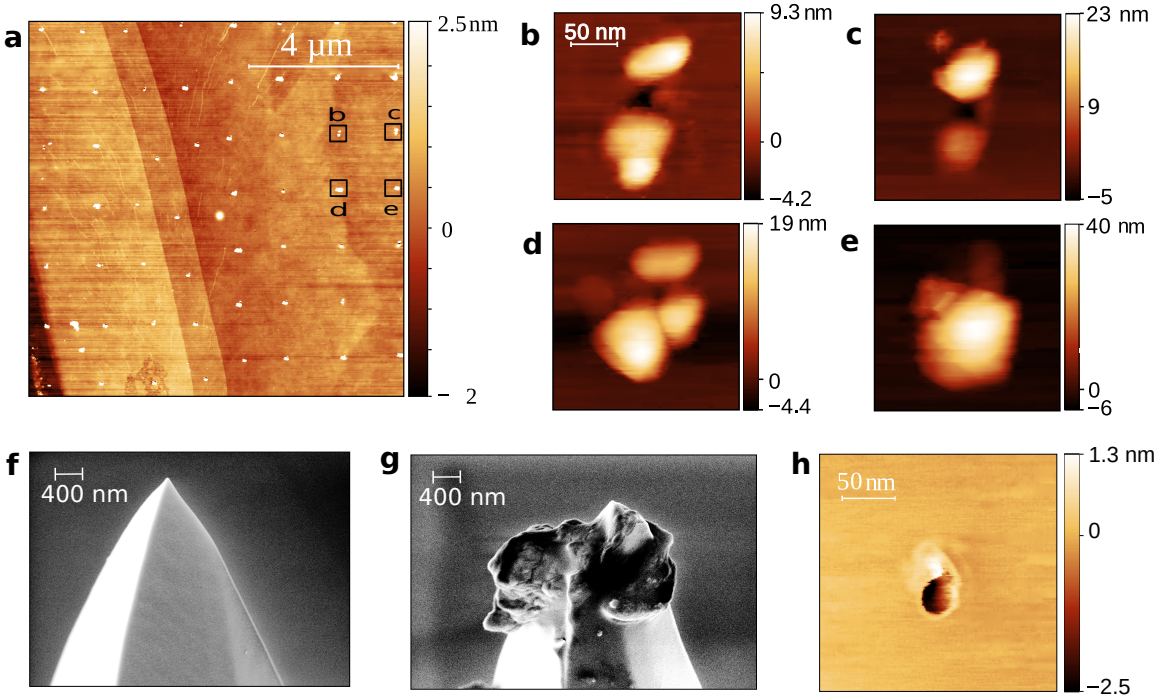

Figure 4.10.: Shows topographical changes of AFM nanoindentation on hBN and the indenting tip. (a) AFM scan in tapping mode after indentation. (b), (c), (d), and (e) exemplarily show higher-resolution images of the individual indents. (f) and (g) are SEM images comparing a carbon-coated diamond-like tip before(f) and after(g) being used for indentation on hBN flakes. (h) high resolution scan in tapping mode of an indent after contact AFM cleaning.

Although the AFM tip is engineered for hardness, it undergoes erosion during indentation, evidenced by comparative examination of an unused tip in figure 4.10(f) and a used one in figure 4.10(g). This erosion would result in carbon deposition around indents, since it is a diamond-like carbon (DLC) coated tip, supporting the notion that AFM nanoindentation introduces carbon into hBN, fostering carbon defect formation. The indents appeared cleaner following contact AFM cleaning [100–103], as shown in figure 4.10(h). If the debris were solely broken hBN flake, the indent shapes would remain the same or exhibit signs of tearing after 'cleaning', which pushes any debris to the scan edges. Thus supporting that the debris removed from contact cleaning are loose particles (from the tip) which can be pushed to the sides with light contact mode AFM scanning, proving that indentation leaves tip remnants on the indentation sites. Moreover, the protrusion at the top of the indent in figure 4.10(h) is visible which must be broken hBN which was pushed and remained attached to the indentation pit.

Figure 4.11 presents optical images of two hBN flakes showing tearing post-contact scanning on indented regions. This tearing occurred as the contact scanning threshold voltage was 1.6 V, much higher than the 1 V generally used for contact AFM cleaning. The tip

pushed the broken hBN flake around the indents to cause tearing. hBN is a rigid material which does not tear from contact mode cleaning alone (see **??**: it creates strain in this voltage), it only caused tearing on areas where indentation was made. This further confirms that the debris comprises of both fragmented hBN and carbon remnants from the AFM tip.

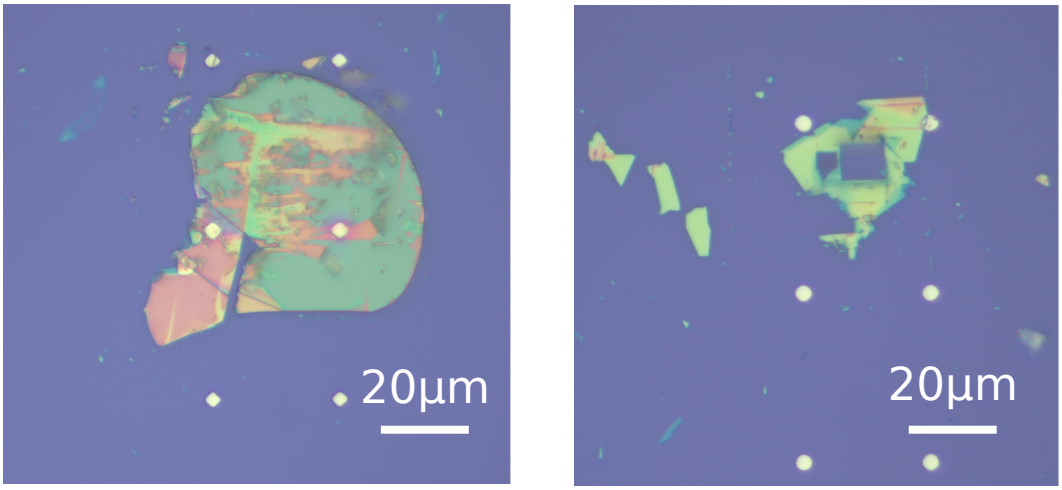

Figure 4.11.: Show tearing caused by high voltage AFM contact cleaning after indentation. The flake protruding from indentation gets pushed to cause tearing during contact scanning. The image on the right shows complete removal of the square region of the flake due to contact AFM.

The introduction of carbon via AFM tip indentation, combined with the formation of flake edges during the process, creates energetically favorable sites for hosting optically active defects. Quantum emitters in hBN are known to exhibit enhanced stability near flake edges, owing to the unique structural and electronic environment found there. At these edges, atoms have fewer neighboring atoms, which leads to increased bond strain and the presence of dangling bonds. These under-coordinated sites are more susceptible to defect incorporation, facilitating the formation of quantum emitters that benefit from the stabilizing influence of the edge environment [19]. As discussed in the theoretical section, carbon is particularly suited for this role due to its low energetic barrier for forming bonds with boron and nitrogen atoms.

4.3. Argon Flow Etching

The next important fabrication parameter which brings about important changes on the topography of the hBN flake is annealing. Annealing does not only play a vital role in

activating emitters but also modulating surface topography. Our findings indicate that annealing at elevated temperatures can induce random etching in hBN. When excessive, the etching produces an erratic environment, leading to weak and unpredictable ensemble SPEs. This is especially a problem when several layers of hBN are removed from top, via uncontrolled etching as will be shown in 4.14(b). Thus we try to find parameters that cause minimal etching. We analyzed the influence of AFM contact cleaning, oxidation conditions, and the flow of Ar gas during annealing. Assessing the annealing parameters, in particular, has enhanced our capacity to regulate the local environment and yield of the SPEs.

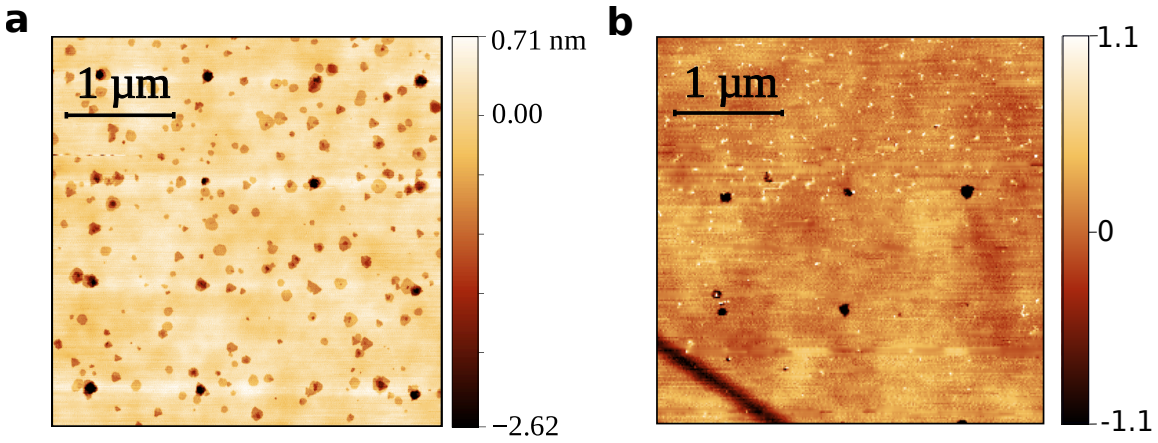

Figure 4.12.: (a) AFM topography scan in tapping mode showing Ar annealed arrays of indents along with random etched pits visible from annealing all over the region. (b) Another indented flake which has also been annealed in Ar flow but was AFM contact cleaned before and after indentation. Random etching was reduced for this flake.

Figures 4.12, 4.13 and 4.14 illustrate comparison of high-resolution atomic force microscopy (AFM) scans in tapping mode, examining the indents after annealing under various conditions. In figure 4.12(a) the hBN flake is indented and subsequently annealed in an Ar flow of 15 ml/min at 850 °C. This process results in the formation of widespread, randomly distributed etched pits, with the deeper pits corresponding to the indentation sites. These pits appear distinct, without any surrounding coagulation of hBN. It should be noted that the sample in figure 4.12(a) was not subjected to AFM cleaning either before or after the indentation. In contrast, another sample in figure 4.12(b), which underwent the same Ar annealing process but was AFM contact cleaned prior to indentation, demonstrates a significant reduction in random etching pits. The random etched locations in Figure 4.12b are identifiable by elevated areas (white spots) on the surface, indicative of upturned BN flakes. With this figure 4.12, we demonstrate that annealing at 850 °C, even in an inert environment, can initiate etching in hBN, and intrinsic defects along with contaminants

further facilitate this unpredictable etching as also seen for the case with high coverage of sputtered carbon on hBN in figure **??**(a) after annealing.

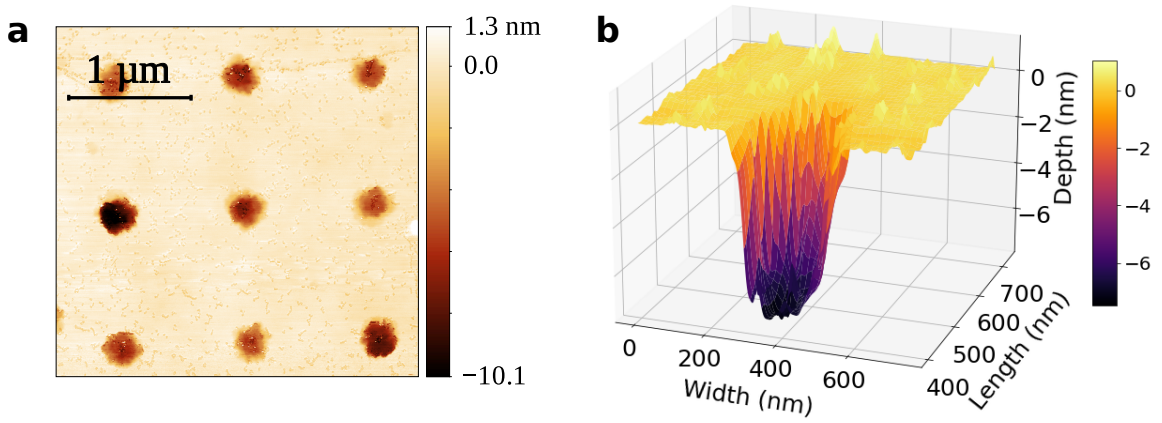

Figure 4.13.: (a) Tapping mode AFM scan on an air annealed flake region which had been indented in an array before annealing. Figure (b) shows AFM 3D representations of one of the indents in flake in (a) clearly showing the hBN layers etched in air.

Figure 4.13(a) illustrates effects of annealing in air after nanoindentation. The oxidation causes deep and isotropic etching [104] as visible from the the size and depth of the indented spot. And similar to random etches portrayed in figure 4.12, annealing in air also brings about random etching pits all over the flake. Figure 4.13(b) showcases a three-dimensional AFM scan of its indent, revealing layered etching and a rough surface at the base of the indent. The air constituents (N_2 and O_2) seem to have a stronger detrimental effect on the chemical stability of hBN.

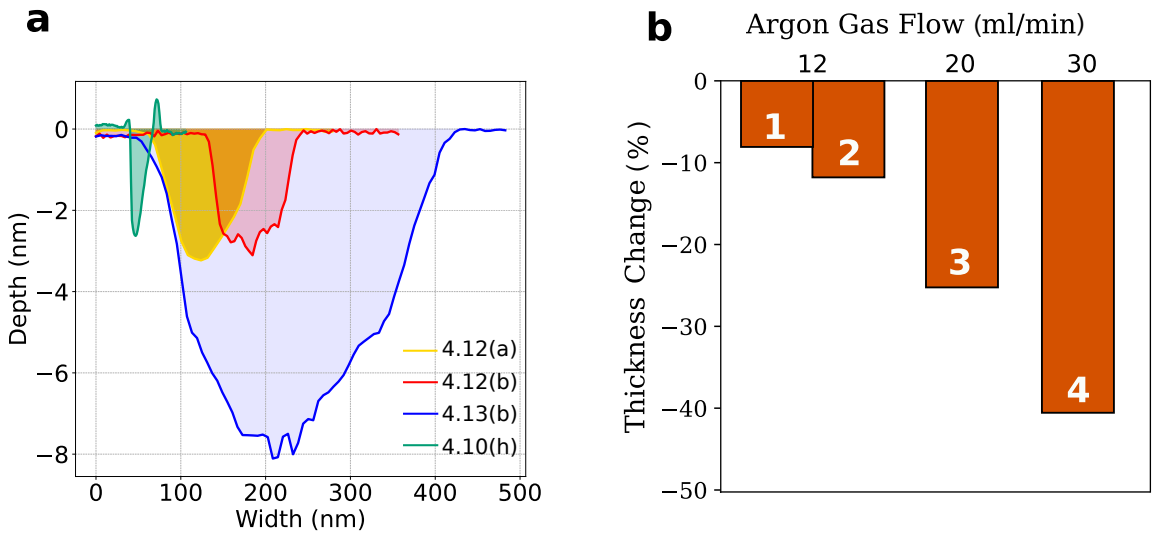

Figure 4.14.: (a) Comparison of the depth and width of indents from samples prepared with different recipes and an unannealed and contact indent from figure 4.10(h) (b) Comparison of the thickness change in hBN flakes after annealing at different Ar flow concentrations.

Figure 4.14(a) illustrates a comparative analysis of the depth and width characteristics of the indents following three distinct annealing processes, as described in figure 4.12(a), figure 4.12(b), and figure 4.13, alongside a control indent that was not subjected to annealing, previously illustrated in figure 4.10(h). These are cross-section height profiles across each of these exemplary indents. When hBN is subjected to high-temperature annealing, irrespective of whether it occurs under argon (Ar) or atmospheric air conditions, a consistent pattern of extensive etching is observed. The indent profiles after Ar annealing labeled 4.12(a) and 4.12(b) are around a 100 nm wide compared to ≈40 nm width of an indent before annealing as seen from 4.10(h). It is also noted that although the indent width increases by almost over double the size after annealing, the depths of the indents do not change much after annealing. In addition, note that the profile of the annealed indent from 4.12(a) has less roughness compared to the other two annealed indents 4.12(b) and 4.10(h), this is because 4.12(a) is from single crystal hBN which has higher crystallinity than flakes from powdered crystals as explain in section 3. The annealing parameters and the type of material used for these different samples are summarized in table 4.1). The protrusion of hBN flake seen in 4.10(h) profile at the edges of the indents is not present after annealing as it gets all etched away. The etching is extremely pronounced particularly in air annealing as visible from 4.13(b). The indent gets approximately 8 nm deep and 400 nm wide, which are approximately four times the etching seen after Ar annealing. This etching, despite an inert environment led us to look into the parameters and source of Ar etching further.

In addition to the gas species, the effects of gas flow, pressure, and annealing time on the morphology of the hBN flakes were also investigated. Four more sets of annealing were conducted to test the etching effects and their results are compared in figure 4.14(b). Measurements of thickness variations before and after annealing were conducted on three flakes per set for different parameter sets of annealing (Table 4.1), and their average thickness changes are depicted. The results indicate that in the pressure range of 6 mbar to 20 mbar Ar, pressure fluctuations had a minimal impact, while the Ar flow rate significantly affected the thickness reduction, that is, etching.

Comparing the annealing parameters used and their corresponding thickness reduction values from sets 1,2,3 and 4 suggest that the flow of Ar has a dominant effect on the process of physical etching. The reason is possibly a combination of enhanced hBN sublimation and the physical impact of Ar molecules. This is best seen by comparing sets 1 and 3 (Table 4.1), where the latter was performed at a much higher flow but at a lower Ar gas pressure.

Despite inert gas conditions, hBN starts to decompose at around 850 °C. An increased Ar flow accelerates sublimation by promoting the ablation of disintegrated surface molecules at a higher rate. Additionally, collisions with Ar atoms contribute to the enlarged indentation features observed after annealing. This is consistent with the formation of pillar-like roughness following substantial etching which removes multiple hBN layers.

Set	T_A (°C)	t_A (min)	P_A (mbar)	Ar flow (ml/min)	**Exfoliated from**	**Thickness reduction (%)**
Fig. 4.12(a)	850	30	6	15	single crystal	–
Fig. 4.12(b)	850	30	6	15	powder	–
Fig. 4.13(b)	850	30	1000	in air	single crystal	–
1*	1000	30	20	12	single crystal	8.1
2*	1000	15	16	12	powder	11.5
3	1000	30	6	20	powder	25
4	1000	30	14	30	powder	40.5

Table 4.1.: Parameters for thermal annealing of hBN in Ar or air.

*Degassed at 400 °C for 15 min before raising to activation temperature. The oven was purged before these annealing sequences.

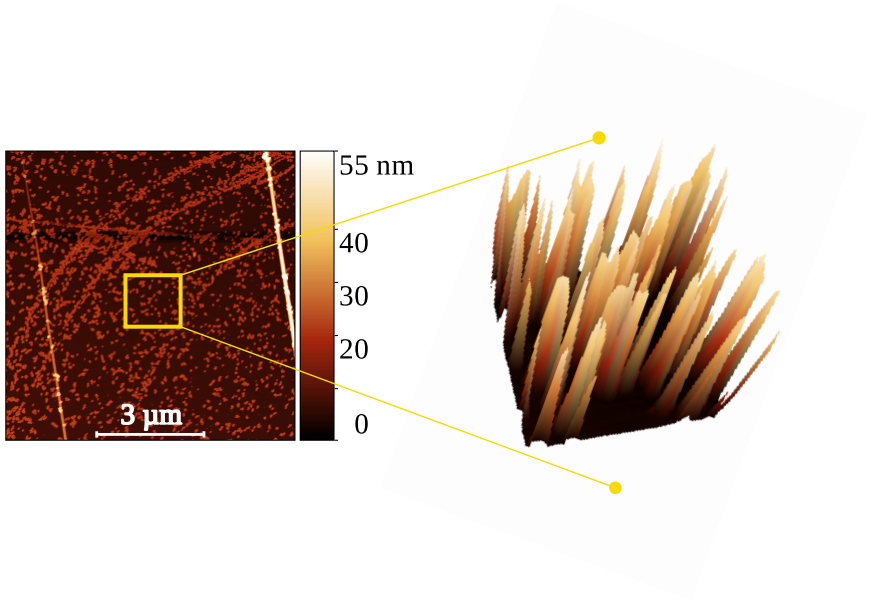

Figure 4.15.: On the left shows 8 µm × 8 µm AFM tapping mode scan of a flake that exhibited thickness reduction due to excessive etching. The inset 2 µm × 2 µmshows a 3D image of the resulting debris, revealing pillar-like structures. Such uneven topography has been reported on flakes annealed with an Ar flow rate of 15 ml/min or higher.

Figure 4.15 shows a flake from Set 3 after annealing. A region from the flake is shown in 3D, illustrating the pillars which are around 20 nm high. We think these pillars are disintegrated hBN which was not removed by the Ar flow. The high temperature annealing which is commonly done for activating and stabilizing SPEs in hBN bring about drastic changes on the surface topography and on the underlying substrate. As reported similarly in other studies, this process can cause cracks and strain in the hBN, forming walls and trenches—much like the effect of an earthquake on the Earth's tectonic plates [105, 106].

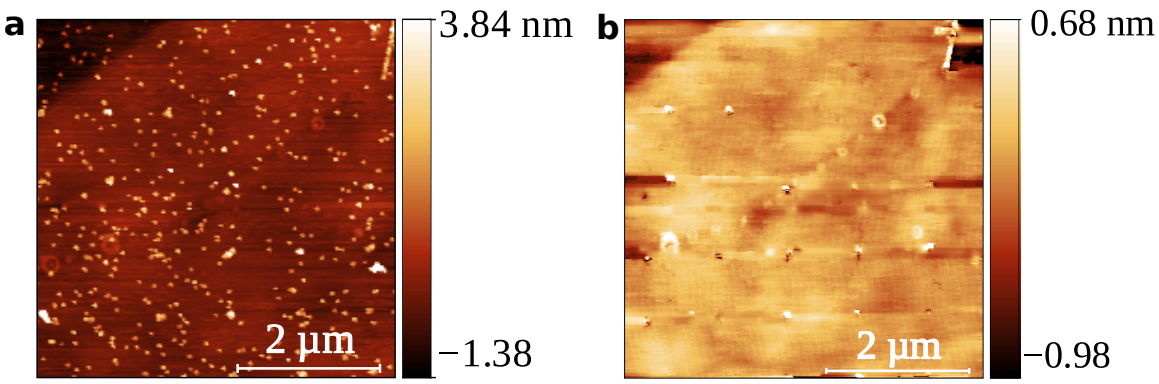

Figure 4.16.: Shows a flake from set 1, with only 8 % thickness reduction after Ar annealing. Left image shows AFM scan in tapping mode. Image on the right labeled (b) shows contact scanned image of the same region with a different AFM tip, showing that debris is removed after contacting scanning and the indentations on the region can now be visible.

Such pillar like structures and other roughness can be removed through contact AFM cleaning, as shown in figure 4.16. Contact scanning pushes any debris to the edges of the scan window forming heaps of collections at the left and right side of the scan window (as can be seen in figure 3.10(a)). After contact cleaning, the patterned indents made before annealing become visible. This shows that the adsorbates are removable and thus have higher chances to be disintegrated hBN. The contact cleaning is done with Multi75DLC AFM tip which has a 15 nm tip radius thus random smaller holes are not visible in the resolution of this scan.

Contact cleaning. Removing surface contaminants and inherent defects before annealing—such as through AFM contact-mode cleaning, as shown in figure 4.12(b)—reduces etching. While moderate etching can enhance the emitter yield on a specimen, excessive etching—caused by increased Ar flow—leads to surface roughness that facilitates the formation of structural irregularities and various energy states, thereby increasing phonon coupling and reducing quantum efficiency. Therefore, maintaining sample cleanliness and a controlled annealing environment is vital for the precise formation of SPEs in hBN. Our fabrication process ensures a clean surface after exfoliation, followed by annealing in a low Ar flow of 10 ml/min at 14 mbar pressure. The detailed fabrication protocol for the emitters is provided in section 3 of this thesis.

4.4. Deterministic Creation of Emitters

Now that we have established important fabrication parameters that affect the topography of the flakes let us look into the fluorescence properties that result from this fabrication technique.

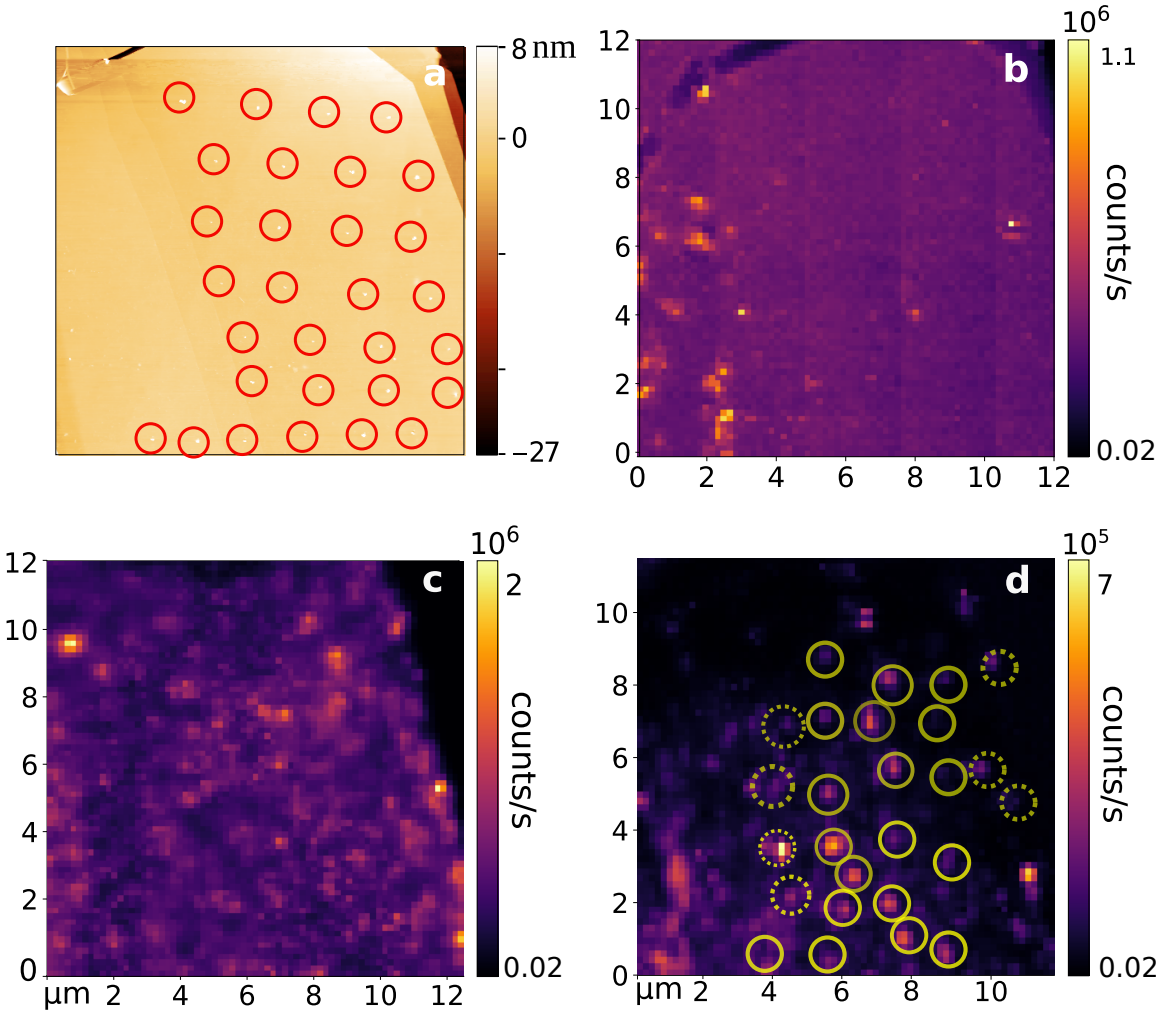

Figure 4.17.: Comparing topography and fluorescence of indented hBN in the same region. (a) AFM scan after indentation before annealing. Each indent has been circled as a guide to the eye. (b) Fluorescence intensity map before annealing. (c) Fluorescence intensity map after annealing at 850 °CC. (d) Fluorescence intensity map after annealing at 1000 °C. Activated SPEs near indent locations are marked by solid circles, while emitters that appear at some distance away from any indent are marked by dashed circles.

Activated Quantum Emitters. Figure 4.17 compares the topography and fluorescence of the same region before and after annealing, demonstrating how the process activates defects in the indentation areas of the flake. Figure 4.17(a) shows an AFM tapping mode scan of a 10 µm region after indentation and prior to annealing. The indented spots are

circled for visual guidance; note that they are not arranged in a perfect array. The same region was then imaged under fluorescence to produce figure 4.17(b), which confirms that indentation alone is insufficient to generate SPEs.

Following annealing at 850 °C, figure 4.17(c), fluorescence is observed; however, most emitter-like spots either bleach rapidly or exhibit blinking behavior, and the indented pattern becomes indistinct. This indicates that annealing at this temperature does not produce stable, deterministic SPEs. In contrast, after annealing at 1000 °C, figure 4.17(d), every bright, round fluorescence spot—circled for clarity—is confirmed to be an SPE. Solid-lined circles mark emitters located near indents, while dashed circles indicate emitters not clearly associated with an indentation.

The confocal excitation volume in our measurements (approximately 270 nm lateral diameter and 900 nm depth) is much larger than the size of an individual indent. Therefore, we cannot pinpoint the exact subdiffraction location of an emitter within an indent from the far-field image alone. Given that a nanoindentation produces a crater on the order of tens of nanometers, it is unlikely that a point defect is created exactly at the center of the indent. Instead, we observe that emitters tend to form around the periphery of the indent sites, predominantly near the fractured edges of the indentations. It is possible that defects initially created at the indent bottom migrate to the flake surface or to nearby regions during high-temperature annealing and eventually settle in energetically favorable locations[107–109]. Importantly, annealing the indented regions at 1000 °C in Ar activates a dense ensemble of emitters within an area of roughly $11 \times 11\,\mu m^2$, underscoring the effectiveness of this fabrication technique in producing SPEs.

4.5. Photophysical Properties of Emitters

In this section we analyze the photophysical properties of the emitters in our sample. We collected fluorescence and spectral data from 12 different flakes from hBN micropowder which were fabricated the same way: AFM nanoindentation followed by annealing at 1000 °C with low Ar flow for 30 min. All emitters presented have been confirmed to be an SPE using HBT experiment setup. The emitters are classified into three different types: isolated, 2 to 3 emitters and ensemble emitters. This refers to the distinguishable emitter emission line visible within one confocal volume. Figure 4.18 illustrates the difference. Isolated SPE refers to such standalone sharp SPE as shown in figure 4.18(a). Note that this particular emitter is very bright compared to photon counts from ensembles in figure

4.18(c), the spectra are always taken with one minute integration time with same laser powers. Indicated '2/3 emitters' in figure 4.18(b) are when more than one emitter is visible in the spectral data and the $g^{(2)}(\tau)$ is higher than 0.5. The defect environment affects the type and quality of the SPE. Ensembles are created more often in strongly etched samples. If the exfoliated flake is noted to have adsorbates or bubbles, it is likely to have many dim (low brightness) emitters which show photo instability. Another observation is that exceptionally bright emitters have a higher likeliness to have photo instability than moderately bright ones. Ensemble SPEs, at room temperature, have shown good stability.

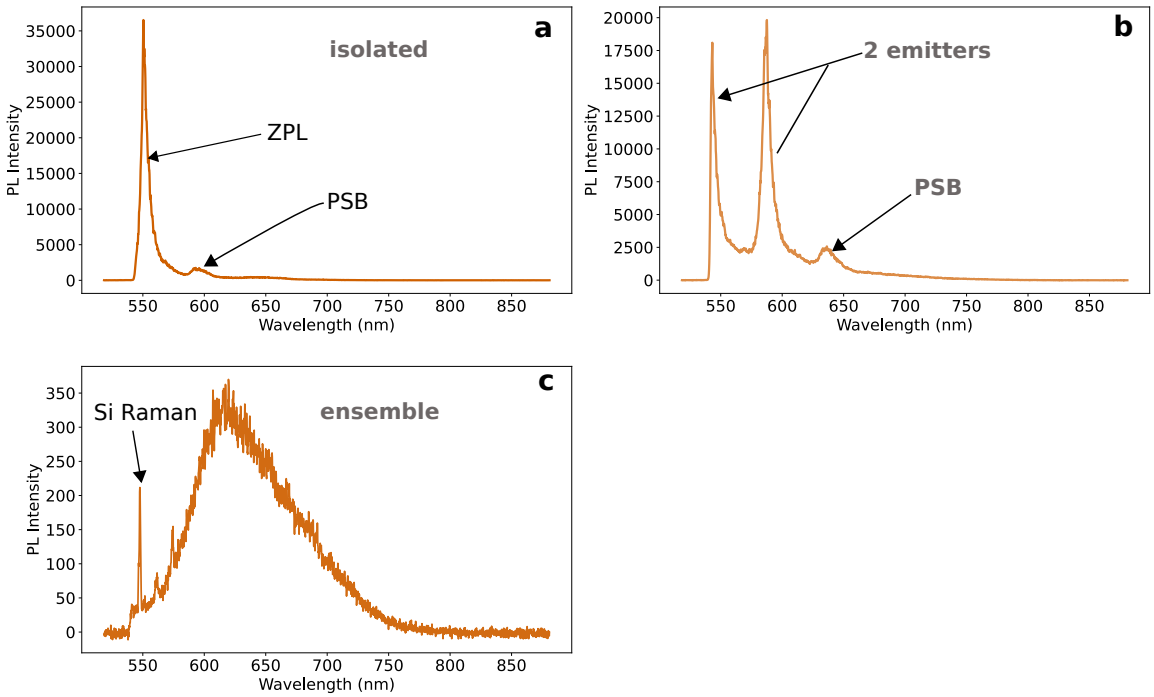

Figure 4.18.: Classification of emission spots: (a) isolated SPEs, (b) double or triple emitters (2–3 emitters in one spot), and (c) ensemble emitters (multiple distinguishable or indistinguishable overlapping emitters in one confocal volume).

Figure 4.19(b) demonstrates that our fabrication process yields emitters of which approximately 70 % from 305 evaluated emitters can be distinctly identified and 47.2 % were isolated SPEs, rather than clusters or ensembles. This distinction is crucial, as isolated SPEs exhibit well-defined electronic transitions that are accessible at room temperature, allowing observation of spectral shifts and other emission properties. The isolation of individual emitters also enhances signal-to-noise ratio by minimizing background fluorescence—an advantage particularly relevant for techniques such as optically detected magnetic resonance (ODMR) or optical/magnetic manipulation of defect states [8, 110].

Among the SPE detected we have distinct emitter classes that emerge, exhibiting exceptionally sharp features and high brightness. The SPE with ZPL in between 565 nm (2.19 eV) and 590 nm (2.10 eV) are class A emitters. Another class, identified between 540 nm (2.30 eV) and 560 nm (2.21 eV), is referred to as Class B. These emitters have previously been associated with carbon-related defects that exhibit spin properties [8]. Additional emitter classes are found in the 620 nm to 640 nm range (Class C) and around 700 nm (Class D). Although Class D emitters are less common, they exhibit weak phonon coupling and a high Debye-Waller factor, characteristics that are desirable for quantum applications. Interestingly, a higher number of Class D emitters were observed in samples subjected to extensive etching. Figure 4.19a provides a representative overview of these identified emitter classes showing distinct zero-phonon lines (ZPLs) at 550.4 nm, 571.2 nm, 625 nm, and 713.3 nm.

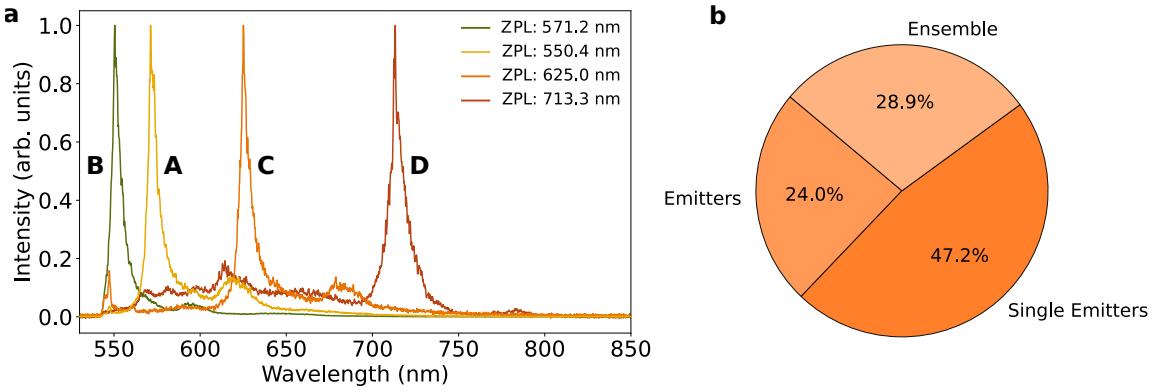

Figure 4.19.: (a) Photoluminescence spectra of representative emitter classes detected in our samples (b) Distribution of emission types observed in the study.

Figure 4.20(b) shows distribution of the linewidth of the isolated emitters. It shows that most of the isolated emitters in classes A and B have a narrow linewidth indicating a higher quantum efficiency. The linewidth for this distribution has been derived from the experimental data of the spectra as shown in an example in figure 4.20(a). The ZPL in figure 4.20(a) has a linewidth of 5.46 nm.

With figures 4.17, 4.18, 4.19 and 4.20 we demonstrate that this fabrication techniques produces sharp, bright and isolated SPE that would provide a good platform for further quantum device applications.

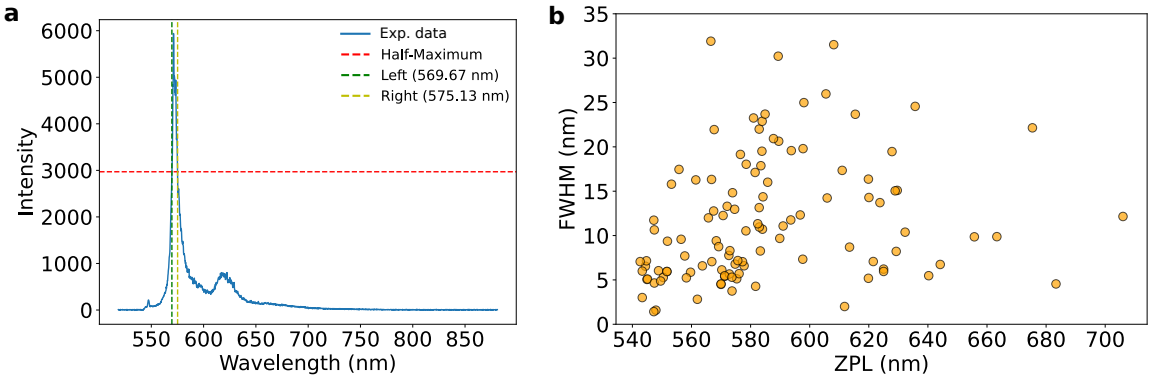

Figure 4.20.: (a) Spectrum of an isolated SPE showing how the FWHM (5.46 nm) is deduced from the experimental data (b) Full width at half maximum (FWHM) of the isolated SPEs as a function of their ZPL positions.

4.6. Reproducible Carbon Emitters

Properties of Class A SPE. Figure 4.21(a) depicts the distribution of occurrences of ZPL positions derived from the spectral analysis of 305 emitters identified across 12 distinct flakes. Spectra were collected with one minute integration period. Notably, 41 % of these emitters display ZPLs within the 565 nm to 590 nm (2.19 eV to 2.10 eV) spectrum, categorized as emitter class A. While other emitter types are present in the sample, they occur less frequently as shown in the histogram in figure 4.21(a).

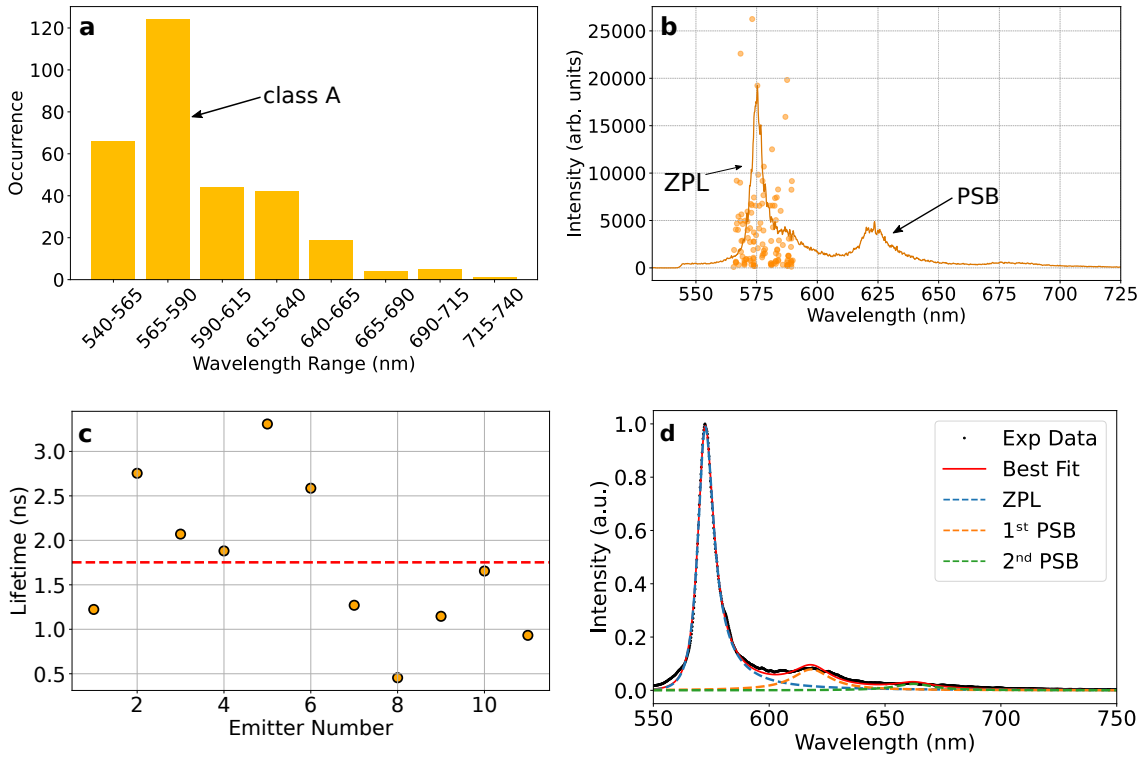

Figure 4.21.: Emitter class A and their photophysical properties. (a) Distribution of occurrences of a total of 305 SPEs with different emission wavelengths. The most reproducible SPE is in the 565 nm to 590 nm range, named emitter class A. (b) A representative photoluminescence (PL) spectrum of type A, showing a sharp ZPL at 575 nm and PSBs at 625 nm and 680 nm respectively. The dots are ZPL of other class A emitters. (c) Shows characteristic lifetime decay of class A emitters from the same flake to be around 2 ns. (d) Spectral fit to find DW factor, PSE and Huang Rhys factor for an isolated emitter. The average values for class A emitters are provided in Table 4.2.

Figure 4.21(b) illustrates the ZPL distribution of emitters in the (565-590 nm) range in dots, centered around a representative bright emitter in class A. The dominant emission centered at 575 nm (2.16 eV) suggests the deterministic creation of a particular class of defects. Slight variations in the ZPL of the same defect type, likely influenced by local atomic environment, can be mitigated by tuning the emission frequency by strain through

the external application of stress [78, 111]. Note that the PL intensity for many of the emitters has 8 times more photon intensity than the average.

Additionally, at room temperature, the lowest recorded inhomogeneous linewidth for hBN is ~9 nm [11, 112]. Indicating that many of these class A emitters could be belonging to the same type of defect class. This proves a high probability of reliably fabricating a single type of defect using this method. Emitters near 575 nm (2.16 eV) have been reported in previous studies [99, 113] and have been associated with carbon-related defects [10, 46]. Theoretical studies indicate that multiple carbon defect configurations are energetically favorable within the 540 nm and 640 nm range which is between the 2.30 eV and 1.90 eV range [55, 114–116]. This broad range suggests that precise identification of defects remains challenging. Furthermore, local environmental factors such as strain and charge states can influence the spectral properties of a single defect type, potentially resulting in shifts in ZPL.

Thus, in order to further understand the most abundant SPE emission range, we have looked into their lineshape, PSEs and lifetimes. The PSE is derived from the distance between the ZPL and the PSB. A characteristic time τ_0 for the excited state is derived from a fit $g^{(2)}(\tau) = 1 - a \cdot \exp(-|\tau|/\tau_0)$ of the second-order correlation measurement $g^{(2)}(\tau)$, where τ is the measured delay time between detection of two consecutive photons. Here, τ_0 is an estimate for the lifetime of the excited state. Figure 4.21c shows lifetime of class A SPEs from the same flake derived from second order correlation functions, showing an lifetime of around 2 ns. The exact determination of the latter would require an analysis of its dependence on the laser intensity [117]. The laser power used for all room temperature measurements has been less than 100 µW as mentioned earlier in the beginning of results section 4.1. Here, lifetime is compared among 11 emitters and from the same flake to minimize discrepancies arising from thickness variations. However, we have observed that emitters with similar ZPL positions and line shapes do not necessarily have the same lifetimes. To portray this, spectra from emitters in figure 4.21 along with their $g^{(2)}(\tau)$ is given in the Appendix figure A.2 and figure A.3.

For a more quantitative analysis we fitted the spectra of class A emitters to obtain the Debye–Waller factor $W = I_{\mathrm{ZPL}}/I_{\mathrm{total}}$, i.e. the ratio of the integrated emission intensity of the ZPL to the total integrated emission intensity, and the Huang–Rhys factor $S = -\ln W$ [118]. A representative spectrum of an isolated SPE is shown in figure 4.21(d), where the ZPL accounts for $W = 0.80$ (80 % of the total emitted photons are in the ZPL) and the primary PSB appears at an energy of 162 meV, yielding a Huang–Rhys factor $S = 0.22$. The

best fit was obtained with a skewed Voigt function for the asymmetric ZPL lineshape and with Lorentzian and Gaussian functions for the first and second PSBs, respectively. The data from the fits, i.e. the derived values of ZPL, PSE, S and W for the single isolated class A emitters are summarized and compared with the theoretical work [56] in table 4.2.

	ZPL (eV)	ZPL (nm)	PSE (meV)	S	W	time τ_0 (ns)
C_2C_N (calc.)[56]	2.13	582	180	1.35	0.26	2.19
Class A (this work)	2.15 ± 0.025	577 ± 6.8	179 ± 2.17	0.475 ± 0.030	0.631 ± 0.018	2 ± 1

Table 4.2.: Parameters of all class **A** isolated single emitters compared with theoretical results [56].

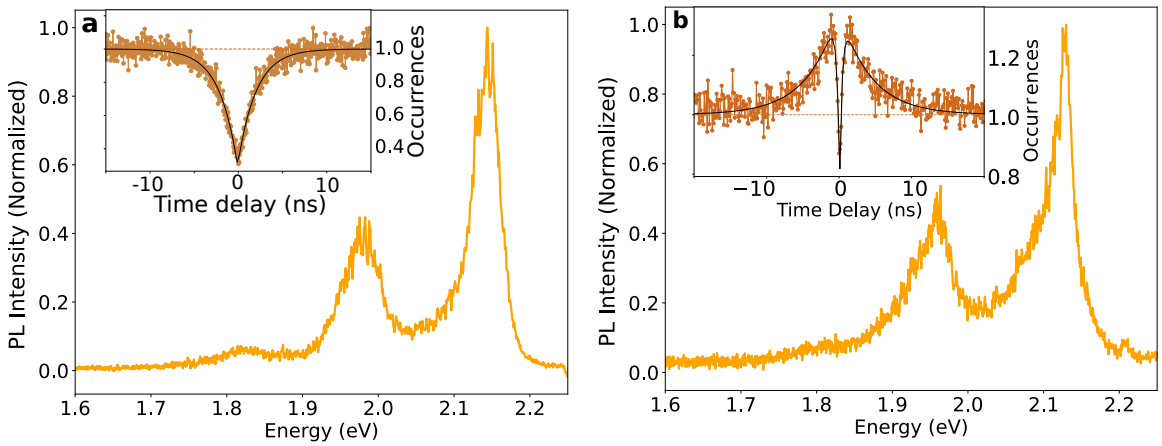

Figure 4.22.: (a) PL intensity spectra in the energy domain. Inset shows the second-order autocorrelation function $g^{(2)}(\tau)$ of this emitter, characteristic to a two level system, confirming the single-photon nature of the emission. (b) PL spectra of another class A emitter. Inset shows the $g^{(2)}(\tau)$ characteristics of this emitter to be a three-level system.

Figures 4.22(a) and figure 4.22(b) highlight examples of class A emitters, whose spectral shape and lifetime (inset) align with the theoretical findings[49]. Figure 4.22(a) has a ZPL at 2.14 eV (579 nm) and two PSBs. Characteristic to class **A** emitters, the second PSB is much weaker with only about 5 % of the ZPL photon intensity. The $g^{(2)}(\tau)$ in the inset gives the lifetime of this emitters from the fit which is the black line: $g^{(2)}(\tau) = 1 - a \cdot \exp(-|\tau|/\tau_0)$. The $g^{(2)}(\tau)$ is 0.309 and the lifetime(τ) is 2.07 ns. Figure 4.22b shows another emitters with ZPL at 2.13 eV (582 nm) with a narrower linewidth and similar asymmetric lineshape than in (a). The $g^{(2)}(\tau)$ of this emitter with fit is given in the inset. Note that the lifetime decay has a bunching shoulder which corresponds to a metastable state. It

is thus fit to a three level system: $g^{(2)}(\tau) = 1 - (a + b)\cdot \exp(-|\tau|/\tau_1) + \mathrm{b} \cdot \exp(-|\tau|/\tau_2)$. The lifetimes for the two relaxation pathways are $\tau_1 = 0.34\,\mathrm{ns}$ and $\tau_2 = 4.26\,\mathrm{ns}$. These two spectra and their second order correlations are taken from two different flakes. Almost all our emitters from class A have shown a behaviour characteristic of a two level system. The narrowest ZPL linewidth recorded among class A SPEs is 4.3 nm, the average linewidth is 15 nm. Notably, the brightest emitters were predominantly found on thicker flakes, and thinner flakes (<30 nm) were more susceptible to broader ZPL linewidth.

Table 4.2 summarizes the optical parameters obtained for all isolated class A emitters and compares them with the theoretical values predicted for the carbon trimer defect (C_2C_N) in hBN [56], the values are obtained from the fit process mentioned earlier at figure 4.21(d). We find excellent agreement in the ZPL, PSE and spectral lineshape of the C_2C_N defect between our experimental values and the theoretical study. The experimental ZPL energy and PSE values are $\approx 2.15\,\mathrm{eV} \pm 0.025\,\mathrm{eV}$ and $\approx 179\,\mathrm{meV} \pm 2.17\,\mathrm{eV}$ respectively. One notable difference is that our experimental Debye–Waller factor W is significantly higher than the theoretical value, as also reported in other experimental works [**Tran2016**, 19, 118]. Consequently, the extracted Huang–Rhys factors in the experiment are smaller than predicted by the theory. Minor discrepancies between the experimental and theoretical values are expected, as the calculations do not fully account for interlayer defects or strain effects that can vary with flake thickness and local environment. Furthermore, mixing of different charge states of the defect can affect the ZPL energy. While the ZPL position, PSE, and the lifetime provide substantial information, they may not alone conclusively characterize the exact configuration of the defect. However, the strong correspondence between our results and the carbon trimer model (C_2C_N) strongly suggests that this defect is responsible for the SPEs we observe. Narrowing down the defect to the carbon trimer is an important step towards delving into its energy-level scheme and spin properties.

4.6.1. C_2C_N Energy System

This subsection compares and reasons the choice of selecting Li *et al*'s work over other former works on C_2C_N defect for comparing our experimental results. It then explains the energy level of this defect and the spin allowed transitions that make up this optically active defect.

Li *et al.* (2022) and Auburger & Gali (2021) both investigate the C_2C_N defect in hBN but from different methodological perspectives. Li *et al.* employ advanced many-body

perturbation theory (GW/BSE) to address DFT's limitations in excited-state predictions, enabling accurate determination of the ZPL and optical properties. The GW approximation corrects quasiparticle energies by incorporating electron–electron interactions via the Green's function (G) and the screened Coulomb potential (W), while the Bethe–Salpeter Equation (BSE) accounts for excitonic effects by capturing electron–hole correlations.

However, in the case of hBN—a 2D material with strong Coulomb interactions—the GW approximation alone tends to overestimate the band gap due to underestimation of dielectric screening. To address this, Coulomb truncation/simplifying the electrostatic interaction, and inclusion of BSE are necessary to capture excitonic behavior accurately. Moreover, in 2D materials, phonons can interact with collective electron oscillations (plasmons). When they couple, they can change how electrons interact with each other. This can make the interactions stronger at certain resonant conditions—something that standard GW calculations usually don't take into account

Li *et al.* assign the ~2 eV SPEs to the C_2C_N defect by comprehensively calculating its atomic structure, electronic levels, zero-phonon line (ZPL), PSB, and photoluminescence (PL) lifetime. Their GW/BSE results yield a ZPL of 2.13 eV, in excellent agreement with experiment, and highlight the role of non-radiative decay in producing the observed 2.2 ns PL lifetime. Before Li *et al*'s work carbon trimers including C_2C_N and C_2C_B were also proposed by Jara *et al* [119] which had good agreement with the experimental PSE and ZPL, however the ZPL was 0.4 eV short of the average value for class A emitters and information on HR factor, PL lifetime and QY (Quantum Yield) which are calculated in Li *et al* was not done in the former.

In contrast, Auburger & Gali conduct a broader survey of carbon-related defects, examining trends in electronic structure and spin properties. Their hybrid DFT + ΔSCF approach predicts a lower ZPL of 1.62 eV and identifies C_2C_N as a deep, paramagnetic center. Specifically, they find that while single C_N or C_B defects yield higher transition energies and the adjacent dimer C_BC_N emits at approximately 4.2 eV, the C_2C_N trimer significantly lowers the ZPL to 1.62 eV. This suggests that adding a third carbon atom forms a localized "molecular" state within the band gap, fundamentally altering the defect's electronic structure. Although their approach captures qualitative trends effectively, the lower ZPL may reflect methodological limitations in treating exciton effects such as done in Li *et a*l's work with BSE treatment.

Despite their differences, the studies agree that C_2C_N introduces multiple mid-gap defect levels, exhibits strong electron–phonon coupling (with comparable phonon sideband

energies), and is stable in all charge states, neutral, positive or negative. The neutral defect has an unpaired electron and localized frontier orbitals that enable optical transitions.

In summary, Li *et al.* provide compelling evidence that C_2C_N is responsible for the ~2.13 eV emitter observed in this work and in prior studies [46], whereas Auburger & Gali emphasize its potential as a spin-active defect. Their complementary approaches collectively support C_2C_N as a promising candidate for both quantum emission and spin-based applications in hBN. In the following sections, I will compare my experimental results with those of Li *et al.*, as their findings closely align with my data. Nonetheless, Auburger *et al.* offer valuable guidance for identifying and characterizing spin defects in hBN.

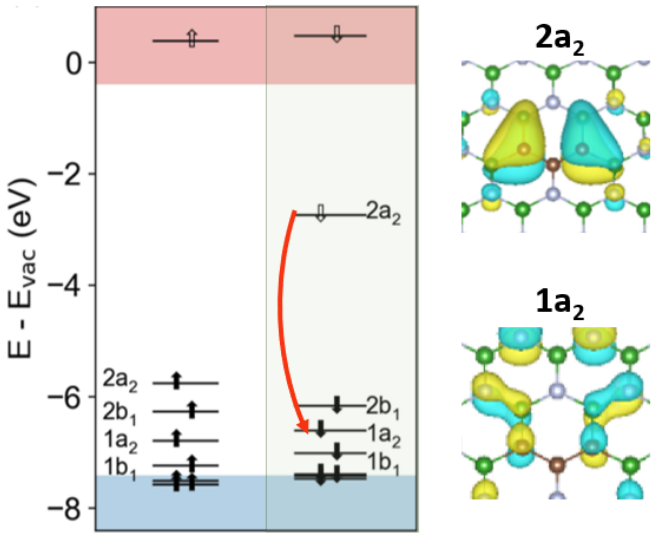

Figure 4.23.: Single particle diagram of the ground state ${}^2_0A_2$. The red arrow shows the most probable optical transition $2a_2$ to $1a_2$. The wavefunction for each of the states on the right show C_{2V} symmetry, allowing the spin conserving intradefect transition while forbidding others for more details into the formulation used to derived the transition levels for the emitter please refer to [56].

In Li et al's work the C_2C_N hosts four localized defect states derived from molecular-like orbitals which are placed within the bandgap which is composed of the unoccupied defect state ($2a_2$) and three occupied defect states ($2b_1$, $1a_2$, $1b_1$) in the spin-down channel as shown in figure 4.23. The most probable intradefect transition involves a down spin relaxation from orbital $2a_2$ to $1a_2$ shown by the red arrow. The absorption peaks are polarized differently along the in-plane x and y directions, corresponding to the orientation

of the C_2 axis in C_2v symmetry. The radiative lifetimes of the intradefect recombination is calculated by Fermi's golden rule and is given by [120, 121]:

$$\tau^{\mathrm{R}} = \frac{3c^3}{4E_0^3\mu_{e-h}^2}, \tag{4.2}$$

with the dielectric constant, ϵ_r, set to 1 since it is a 2D material. This gives the time (on average) for light (a photon) to be emitted when an excited state returns to the ground state by *radiative recombination*. In equation 4.2, τ^{R} denotes the radiative lifetime, which quantifies the average time before photon emission occurs due to radiative recombination. The constant c is the speed of light (in atomic units). E_0 represents the excitation energy, i.e., the energy difference between the excited and ground states of the system. μ_{e-h} is the transition dipole moment between the electron and hole, and μ_{e-h}^2 is its squared modulus, which determines the strength of the optical transition. A larger dipole moment or higher excitation energy leads to a shorter radiative lifetime, indicating a more efficient light emission process. Note that higher the excitation energy E_0, the shorter the lifetime. The radiative lifetime decreases rapidly with increasing energy or dipole moment.

With one dimensional phonon approximation [122, 123] the non-radiative recombination rate from an initial electronic state i to a final state f can be described by Fermi's golden rule as

$$\frac{1}{\tau_{if}^{\mathrm{NR}}} = \frac{2\pi}{\hbar}\, g\, |W_{if}|^2\, X_{if}(T),$$

where τ_{if}^{NR} is the non-radiative lifetime, the inverse of it is the rate of non-radiative recombination or inverse of lifetime; g is the degeneracy of the final state, W_{if} is the electronic coupling between the states, and $X_{if}(T)$ is the phonon-related factor that depends on temperature T.

The electronic coupling term W_{if} is given by

$$W_{if} = \left\langle \psi_i(\mathbf{r},\mathbf{R}) \left| \frac{\partial H}{\partial Q} \right| \psi_f(\mathbf{r},\mathbf{R}) \right\rangle_{\mathbf{R}=\mathbf{R}_a},$$

where ψ_i and ψ_f are the electronic wavefunctions of the initial and final states, H is the Hamiltonian, Q is the phonon coordinate, and $\mathbf{R}_a$ is the equilibrium nuclear position of the final state.

The phonon term $X_{if}(T)$ accounts for the vibrational overlap and energy conservation:

$$X_{if} = \sum_{n,m} p_{in} \left| \left\langle \phi_{fm}(\mathbf{R}) \left| Q - Q_a \right| \phi_{in}(\mathbf{R}) \right\rangle \right|^2 \delta(m\hbar\omega_f - n\hbar\omega_i + \Delta E_{if}),$$

where ϕ_{in} and ϕ_{fm} are vibrational wavefunctions of the initial and final state, p_{in} is the thermal occupation of vibrational state n following Boltzmann distribution, ω_i and ω_f are phonon frequencies, Q_a is the equilibrium position in the final state and ΔE_{if} is the electronic energy difference.

The matrix element $\langle \phi_{fm} | Q - Q_a | \phi_{in} \rangle$ measures the overlap of these phonon states, weighted by the nuclear displacement—reflecting the likelihood of phonon-mediated transitions during the transition. The delta function enforces energy conservation: the energy change in phonons (absorbing or emitting m and n quanta, respectively) must match the electronic energy difference ΔE_{if}. This equation captures how both electronic and vibrational factors determine the rate of non-radiative transitions in defects and underpins the idea of multi-phonon emission—the system can transition non-radiatively by exchanging multiple phonons, provided the total energy is conserved.

Figure 4.24 shows the multiplet structure of C_2C_N. The electronic term W_{if} for the transition ${}^2_2A_2 \rightarrow {}^0_2A_2$ is much larger than the other two transitions, because it is symmetry allowed. Since the non radiative lifetime is inversely proportional to the square of W_{if} , it has a more contribution than the phonon part X_{if}, resulting in τ_{NR} several times shorter than the other two transition. The quantum yield, η [124], is calculated by [125] $\eta = \frac{1}{\tau^{\mathrm{R}}} / \left(\frac{1}{\tau^{\mathrm{R}}} + \sum_i \frac{1}{\tau_i^{\mathrm{NR}}} \right)$. And the PL lifetime is the inverse of the total recombination rate $\tau^{\mathrm{PL}} = 1 / \left(\frac{1}{\tau^{\mathrm{R}}} + \sum_i \frac{1}{\tau_i^{\mathrm{NR}}} \right) = \tau^{\mathrm{R}} * \eta$. They found that (ref. Figure 4.24) that the non-radiative lifetime is almost 10 time shorter than the radiative lifetime, and the Pl lifetime 2.19 ns which is exactly around what is recorded experimentally for emitters with around 2 eV ZPL. Further calculations gave the phonon side bands which are in close agreement to the experimentally extracted values as well.

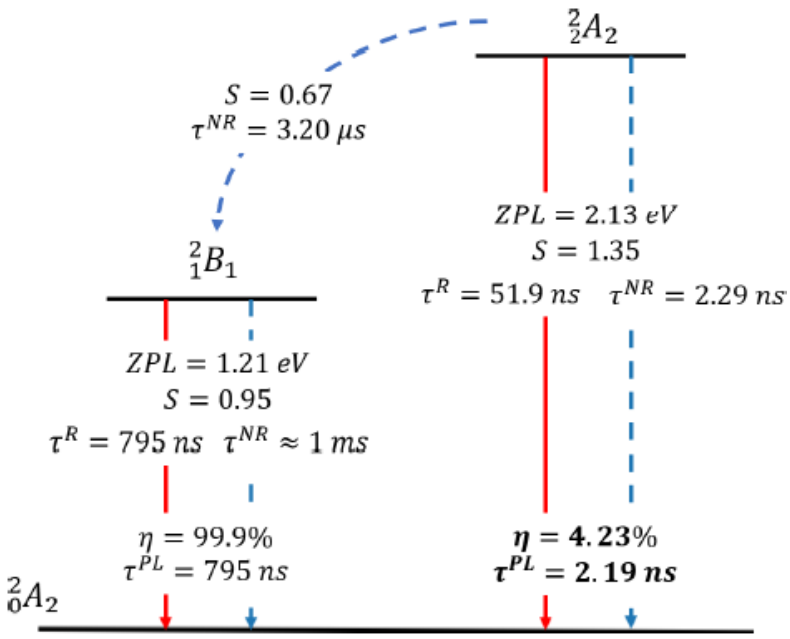

Figure 4.24.: Shows the multiplet structure and key physical parameters of the C_2C_N defect. The ground state is labeled as $^2A_2$, while the two optically accessible excited states are $^2B_1$ and $^2A_2$ (in increasing energy order). Radiative transitions are shown as solid red arrows, and correspond to photon emission (zero-phonon lines, ZPLs), whereas non-radiative transitions—mediated by phonon emission—are shown as dashed blue arrows. For each transition, the Huang-Rhys factor S quantifies the strength of electron-phonon coupling, calculated using full-phonon mode analysis. The radiative lifetime τ^R and non-radiative lifetime τ^{NR} indicate how long the system resides in the excited state before decaying by emitting a photon or via phonons, respectively. The photoluminescence quantum yield η represents the efficiency of radiative emission relative to total decay, and the overall photoluminescence lifetime τ^{PL} reflects the combined effect of both radiative and non-radiative processes. Notably, the lower excited state ($^2B_1$) exhibits a high quantum yield close to unity due to a very long non-radiative lifetime, while the higher excited state ($^2A_2$) suffers significant non-radiative losses, resulting in a much lower quantum yield [56].

4.7. Molecule Deposition

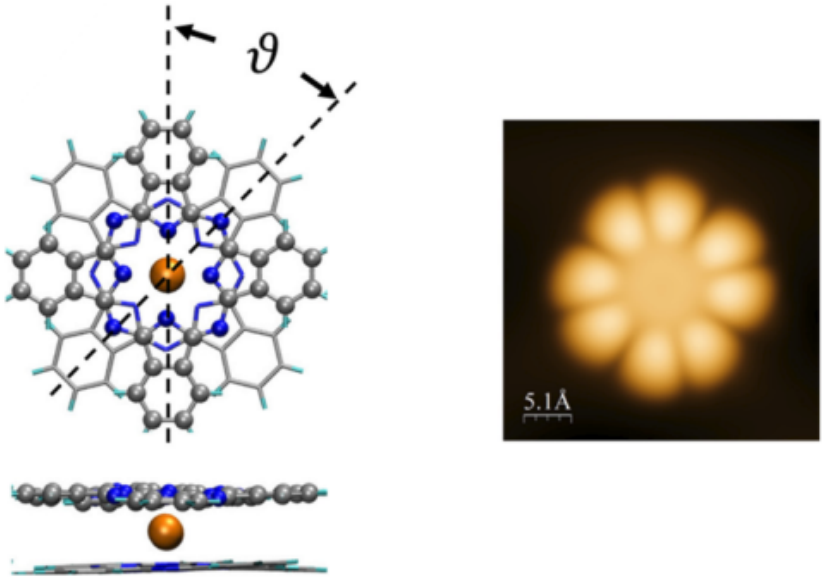

Figure 4.25.: $TbPc_2$ molecular structure taken from [126]. On the left shows the geometry of the $TbPc_2$ molecule. ϑ is the dihedral angle between the upper Pc (balls) and the lower Pc (sticks). Color code: C (grey), N (blue), Tb (orange). STM image on the right visualizes the upper Pc of the molecule on Au(111).

The interaction of a defect with its lattice environment determines its electrical and optical properties. However, to utilize the quantum emitter as a sensor, it is crucial that the SPE remains robust when the sensing target is introduced to the defect. Since the quality and stability of SPE defects in hBN have been shown to deteriorate due to surface contaminants, we examined the effect of our sensing target—i.e., magnetic molecules—on hBN quantum emitters. For this purpose, we selected the bis(phthalocyaninato)terbium(III) ($TbPc_2$) molecule due to its well-studied magnetic properties [28]. If the SPE remains stable upon interaction with $TbPc_2$, it would serve as a promising starting point for establishing hBN defects as nanoscale sensors—an application that remains largely unexplored and unproven.

$TbPc_2$ has been reported to self-assemble or aggregate into islands upon deposition on various substrates, primarily due to strong molecule–molecule interactions outweighing molecule–substrate interactions [126, 127]. The orientation of these molecules on the substrate depends on the material type—whether a metal or a 2D material—and such interactions are critical in determining their electronic and magnetic properties [128, 129]. In this section, we report the optical response of SPEs in the presence of $TbPc_2$, as well as the Raman and fluorescence characteristics of the magnetic molecule on our specific

substrate. Figure 4.25 illustrates the orientation of a single $TbPc_2$ molecule on Au(111), where the top ligand is rotated 45° relative to the bottom phthalocyanine ligand. Notably, a single $TbPc_2$ molecule is over six times larger (16 Å) than the unit cell of hBN (2.5 Å), effectively encapsulating the SPE beneath it. This implies that any optical absorption or emission from the emitter must interact with or pass through the molecule.

We employed two methods for the deposition of $TbPc_2$ molecules: thermal evaporation and drop-casting. In the evaporation method, $TbPc_2$ crystals were heated in a crucible and deposited onto the substrate under vacuum. For drop-casting, the crystals were dissolved in chloroform and dispensed onto the substrate using a pipette, with the substrate placed on a hot plate. Heating the substrate during deposition facilitates rapid evaporation of the chloroform, thereby minimizing molecular coagulation that would otherwise lead to ring-like formations during slow solvent drying. The objective of both deposition techniques is to achieve isolated or small ensemble molecular coverage, rather than the formation of bulk crystals. First, I will present the results from evaporated molecules on hBN.

Evaporated $TbPc_2$ on SPE

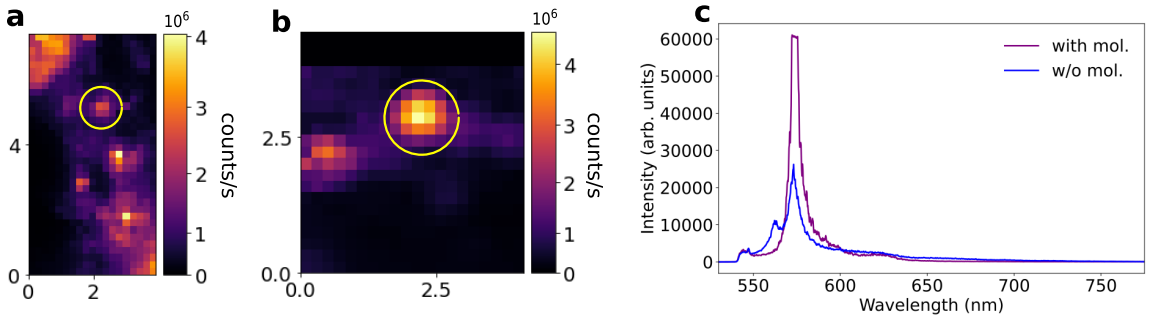

Figure 4.26.: Comparison of emission properties of an SPE before and after 40 % of a monolayer (ML) of evaporated $TbPc_2$.

Figure 4.26 shows comparison of an emitter's optical properties with its fluorescence and spectral data before and after evaporating molecules. Among the bright spots in figure 4.26(a), which are SPEs, the circled emitter is selected for comparison. By using the contrast in the fluorescence map of the flake—particularly its distinct shape and edges—it is possible to reliably locate the same emitter across different measurements. The measurements have all been carried out with room temperature confocal setup at the excitation power of less than a 100 µW on sample with a 532 nm Continuous Wave (CW) laser.

It is evident that the emitter has not quenched but rather has amplified spectral response as shown in figure 4.26(c), which compares spectra taken on the same emitter before and after molecular evaporation. The spectrum taken without molecule has an integration time of 1 min, like all RT spectra recorded in this thesis unless, otherwise mentioned. Since after adding molecules, the spectrum showed saturated counts, it was integrated for 10 s only. Several SPEs showed such saturated counts: some SPE recorded from this sample set before and after evaporation of molecules are shown in figure A.6. In these figures their ZPL photon count against wavelength is plotted.

The amplified spectral response in figure 4.26 may be explained by analogy to the 'antennae effect' expected in sensitizing the Ln^{3+} for magneto-optical read-out[130]. To compensate for the inherently weak absorption of lanthanide(Ln) ions due to parity-forbidden 4f–4f transitions, luminescent Ln^{3+} complexes—such as $TbPc_2$—utilize strongly absorbing organic ligands that act as sensitizers. In these systems, the phthalocyanine ligand plays a critical role by absorbing light in the visible region, with its main absorption (Q-band) typically centered between 600 nm and 700 nm, and a more intense B-band in the 300 nm to 400 nm range [29, 129, 131]. Upon light absorption, the ligand undergoes inter-system crossing from its singlet excited state to a triplet state, which subsequently transfers energy to the lanthanide's excited manifold. For example, in Tb^{3+}, the emitting level lies at approximately 20,500 cm^{-1} (~488 nm), and efficient sensitization requires the ligand triplet state to be slightly above this energy to ensure downhill energy transfer while avoiding back-transfer. This process—known as the "antenna effect"—enables indirect but efficient population of the lanthanide's emissive state, resulting in sharp, long-lived luminescence characteristic of 4f–4f transitions. Therefore, careful alignment between the ligand's triplet state and the lanthanide energy levels is crucial for optimizing both brightness and efficiency in luminescent lanthanide single-molecule magnets.

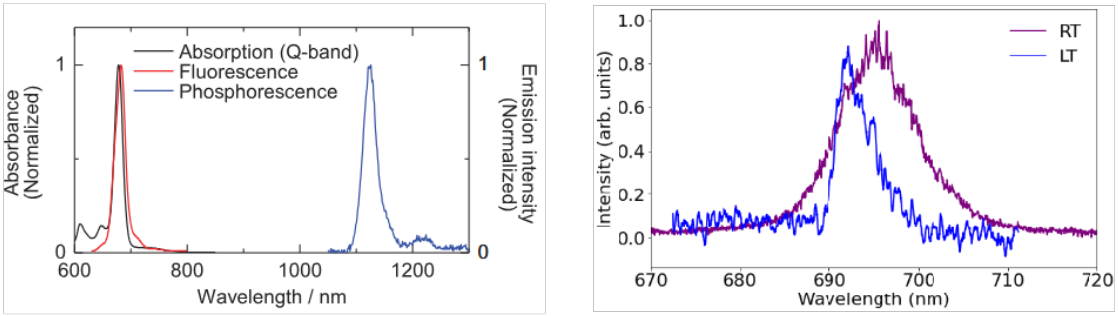

Figure 4.27.: Left shows UV–vis absorption (black), fluorescence (red), and phosphorescence (blue) spectra for Si(IV)tbPc(OH)2 (fig 15 from [29]). Right shows the peak around 680 nm on our samples at RT and LT.

Similarly, if the Pc ligands couple to the defect such that, after strongly absorbing light, the ligand sensitizes the SPE electronic level structure to emit with higher efficiency. In addition to spectral enhancement, the evaporation of molecules exhibited influence on emitter detection, with a greater number of emitters becoming detectable. It is improbable to assert that SPE optical activation occurred due to molecule deposition. Instead, it appears that emitters previously exhibiting dim signals or high background noise, and had fallen through detection as isolated single photon sources, became more easily detectable following the molecule deposition. It is as if the molecular encapsulation results in a lens-like interaction with the emitted photons. More comparison of SPE ZPL counts in individual flakes before and after molecule deposition are provided in Appendix section A.4.

To confirm that this response is indeed in effect to the molecule, we evaporated a higher coverage of $TbPc_2$ molecules onto another sample, aiming to detect the Raman peaks of the Pc ligands. The presence of these peaks would confirm the molecule's presence within the confocal volume. Interestingly, for this sample with a higher coverage of molecules, a peak around 695 nm was consistently observed on the sample globally. They were seen alongside SPE zero phonon lines, on Si substrate and as well on the metal waveguides. Image in the right side of figure 4.27 shows spectra of the 695 nm emission at RT and at LT. The measurements are not done on the same spot: the room temperature (RT) spectrum was taken on a bright spot on the Pt CPW and the low temperature spectrum is another bright spot at the edge of the hBN flake at 50mK. Note that the linewidth is very broad even at LT and is less likely to be an hBN SPE, LT measurements of which are reported in further details in the next section. Such signal is reported for $Si(IV)tbPc(OH)_2$ as shown on the left image of figure 4.27. The complex's excited state characteristics are exemplified here, particularly for $^1(\pi, \pi^*)$ (singlet-singlet) and $^3(\pi, \pi^*)$ (triplet-triplet) states, commonly observed in Pc complexes. In such cases, the luminescent properties are notably influenced by the metal center. Both the absorption and fluorescence maxima are located around 678 nm and 680 nm, respectively, exhibiting a minimal Stokes shift of roughly 40 cm^{-1}, which suggests negligible structural relaxation post-photo-excitation. At 77 K, a broad phosphorescence band is observable around 1100 nm, linked to the $^3(\pi, \pi^*) \rightarrow {}^1(\pi, \pi^*)$ transition. These findings suggest effective inter-system crossing and a prolonged triplet state lifespan, notwithstanding the relatively weak spin–orbit coupling inherent to the Si^{IV} center.

The monolayer molecules on this sample were still too weak to get a Raman spectroscopy. However, in rare cases (because we have most spectra in a narrow range) when the emitter

does not spectrally overlap with the Raman band of the Pc ligands, they are visible from the fluorescence spectral data, as shown in figure 4.28. Here, a 10 min integration time for the spectral collection was used to achieve a better signal-to-background ratio for the Raman branches. The emitter's ZPL appears around 647 nm and, unlike the emitter shown in figure A.6, does not overlap with the Raman features of the ligand.

In the zoomed image on the right, the Raman signals of YPc_2 and $TbPc_2$ crystals are shown to overlap with each other, as well as with the fluorescence signal from the molecule-emitter spectrum (shown in purple). YPc_2 was used to confirm that the observed peaks arise from Pc and not from the magnetic Tb^{III} $^5D_4 \rightarrow ^7 F_4$ transitions, which also occur in the 570 nm to 600 nm range [130].

Raman spectroscopy was performed on YPc_2 and $TbPc_2$ crystals deposited on Si/SiO_2 substrates by Co. The Raman shift in wavenumbers is converted to nanometer for comparison to the fluorescence spectrum of the emitter. The Pc band from the molecule on the emitter lacks sharpness and definition compared to the crystal spectra, due to its amorphous nature. In contrast, the crystalline Raman spectra exhibit long-range order, resulting in well-defined and sharp peaks corresponding to specific vibrational modes of the crystal lattice. While many of the emitters in the range of 540 nm to 600 nm showed enhanced spectral intensity, there were also emitters with no spectral changes. As mentioned, evaporated molecules are unlikely to form a uniform layer that covers the entire flake, rather they have reported to form islands.

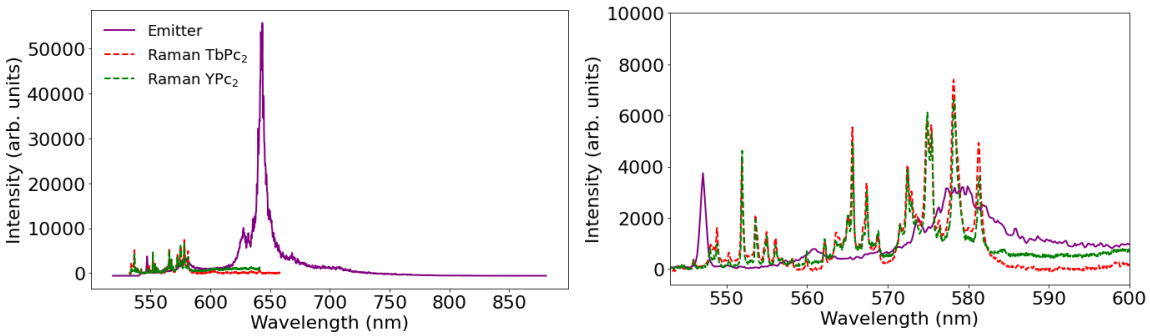

Figure 4.28.: Left shows emitter spectra with evaporated molecule showing a bright ZPL (purple) and Raman spectra of $TbPc_2$ and YPc_2 crystals. On the right the Pc ligand from the crystals and molecule structure between 560 nm and 680 nm is zoomed are shown for better comparison.

Dropcasted Single Molecular Magnet on SPE

After drop-casting molecules, the emitters also remained stable. However as seen for many emitters after evaporation of molecules, there was no saturated counts visible after drop-casting molecules. Some emitters showed slightly enhanced PL counts while others showed no significant changes. Following are two spots on hBN shown in figures 4.29 and 4.30 comparing their fluorescence and spectra before and after molecules were drop-casted.

In figure 4.29, the SPE being compared is circled. The left image is a fluorescence scan of the flake region with an isolated SPE before molecule was drop-casted. The centre fluorescence scan is of the same flake after molecule deposition. Although the scan areas we have for comparison is slightly different, the SPE being compared is clearly visible, and it is certainly the same SPE. The centre fluorescence scan size is bigger than the left scan. The emitter is bright with 4.5 million counts/s before molecules are drop-casted on top. It shows reduced fluorescence of 1.2 million counts/s after molecule evaporation. The rightmost image compares the spectral data from the emitter with and without molecule. Interestingly, there are no visible shifts in the ZPL after the deposition. Drop-casting most likely has the molecules only loosely attached on top of the emitter. The data taken before and after the molecules were taken on the same day with same laser settings, 532 nm excitation laser and ~100 µW power. The spectral intensity counts without molecule is 10 000 and with molecules it is increased to 15 000 counts.

A second emitter chosen for comparison is shown in figure 4.30, where the fluorescence scan before molecule deposition (left), centre image shows fluorescence scan image on the same emitter after molecules and the right image compares the spectral counts on the emitter before and after the molecules were drop-casted. The data taken before and after the molecules were taken on the same day with same laser settings, 532 nm excitation laser and ~100 µW power. The fluorescence counts with molecules is $\approx 3.7 \times 10^6$ counts, and before molecules it was 1.5×10^6 counts. The spectral counts increased from $\approx$ 2000 to $\approx$ 4000. For this particular emitter example, it may seem that the emitter data taken after molecules has a better focus, and thus the higher counts in both fluorescence and spectral data could be reasoned solely to technical causes.

However, that was not the case for this emitter region. As can bee seen in the scans there are emitters present in the vicinity, it was observed that after molecule deposition, the particular emitter' fluorescence was brighter than the surrounding emitters, both images were taken with optimized Z focal position. As mentioned earlier, for evaporated molecule too, after molecule addition, the fluorescence is sometimes more discernible. ZPL

comparison of emitters before and after molecule deposition for different flakes are shown in A.4.

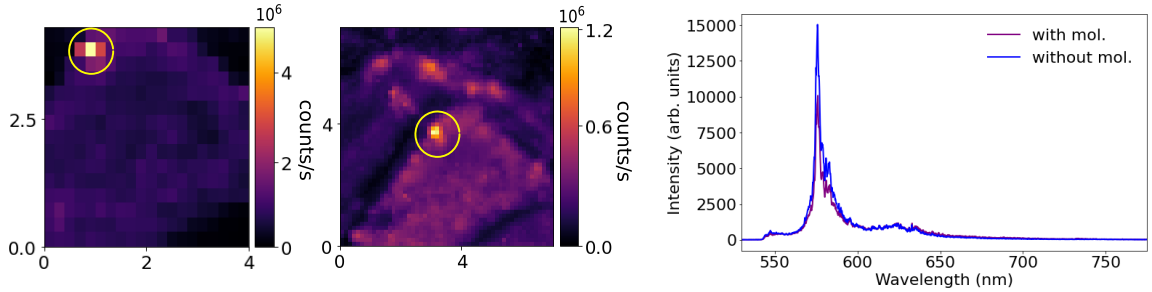

Figure 4.29.: Left shows fluorescence scan of emitter#1 on the hBN before molecule deposition and the centre image shows fluorescence scan after molecule deposition. The right image compares the spectral counts on the emitter from before and after molecule drop-casting.

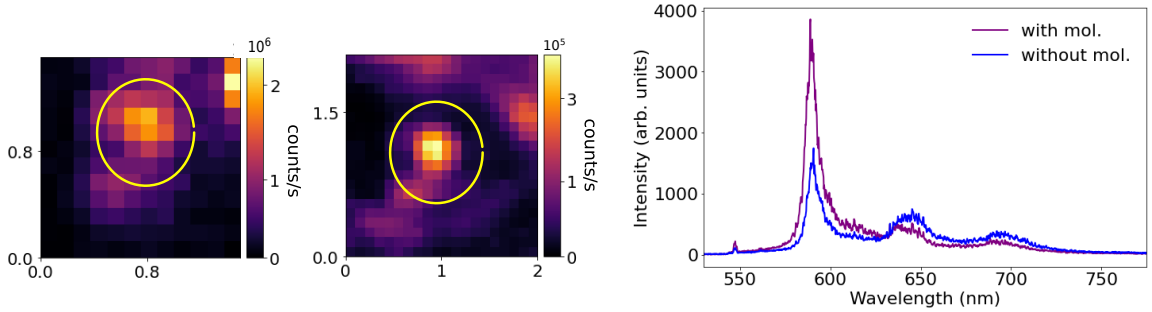

Figure 4.30.: Emitter#2 showing fluorescence before (left) and after (center) molecule deposition. This emitter showed an increased spectral and fluorescence intensity after adding molecules.

We summarize that single-photon sources in hBN do not exhibit quenching upon the deposition of single-molecule magnets such as $TbPc_2$. In contrast, an enhancement in spectral intensity has been observed following the evaporation of $TbPc_2$ molecules. This enhancement can be interpreted by analogy to an antenna effect, wherein the phthalocyanine (Pc) ligand strongly absorbs incident light and transfers energy to the defect site through inter-system crossing, thereby increasing the efficiency of quantum emission.

The structural compatibility between the Pc ligand and the carbon-based hBN defect may play a crucial role in this interaction. Both systems possess hexagonal, covalently bonded ring structures and exhibit symmetry along the *C*-axis. Furthermore, they both display in-plane polarization, which may facilitate dipole–dipole coupling between the molecular ligand and the quantum emitter [132]. Such alignment could enable efficient energy transfer, enhancing the radiative emission of the defect.

However, further investigation is required to elucidate the exact mechanism responsible for this enhancement. Understanding the nature of the interaction will be critical for reproducibly engineering such hybrid systems. This phenomenon raises several intriguing questions that merit deeper exploration:

- Are the emitters coupled to intact $TbPc_2$ molecules, or to partially decomposed Pc ligands resulting from thermal evaporation?
- How are the spin properties of the emitter influenced by the proximity of the magnetic Tb^{III} ion? Could an ionic form of $TbPc_2$ alter or quench the emission?
- Is it possible to control the charge state of the molecule via coupling to a quantum emitter, enabling selective charge transfer in one direction or the other?

Addressing these questions could pave the way toward novel hybrid quantum systems that combine magnetic and optical functionalities with tunable emission properties.

4.8. Low-Temperature Measurements

These measurements have been executed primarily to investigate the electronic level structure of quantum emitters in our sample using Optically detected magnetic resonance (ODMR) and Photoluminescence excitation (PLE) measurements. We have investigated the spectral stability of defects with both off and on resonant excitations and investigated their response to external magnetic fields using a 3D vector magnet. In addition, we have done lifetime measurements on resonant excitation on one emitter which showed PLE.

We investigated optically detected magnetic resonance (ODMR) at low temperatures in quantum emitters from two different hBN flakes across two separate cryostat cooldowns. In these experiments, no clear ODMR signal was observed. The ODMR measurements were performed under off-resonant excitation using a 532 nm laser. A frequency sweep ranging from 0.5 GHz to 4 GHz was applied while an in-plane magnetic field was present. The frequency scans were conducted in 1 GHz segments (e.g., 0–1 GHz, 1–2 GHz, etc.) with a resolution of 1 MHz and a microwave power of +18 dBm.

We also attempted room temperature (RT) ODMR measurements on several flakes. Among these, only one emitter showed measurable ODMR contrast when an external magnetic field of approximately 15 mT was applied using small permanent magnets (see Appendix A.9). For these RT measurements, the emitters were excited with a green laser while sweeping the microwave frequency from 0.2 GHz to 3 GHz. Similar to the low-temperature setup, the frequency range was divided into 1 GHz segments with 1 MHz resolution. A higher microwave power of +17 dBm was used in the room temperature experiments to improve sensitivity.

Figure A.9 shows the room temperature ODMR signal from a quantum emitter in an hBN flake, with a zero-phonon line (ZPL) centered around 577 nm. The data represents the ODMR contrast as a function of applied microwave frequency, with the RF field delivered through an antenna and an external magnetic field of approximately 15 mT applied in-plane using small permanent magnets.

A clear dip in the RT ODMR contrast is observed near 795 MHz in figure A.9, reaching a maximum contrast of approximately −1.2 %. This dip signifies a resonant interaction between the applied microwave field and the spin states of the emitter, consistent with optically detected magnetic resonance behavior. The resonance feature is symmetric and fits well with a Lorentzian profile (indicated by the orange dashed fit), suggesting homogeneous broadening of the transition.

The frequency range scanned spans from 700 MHz to 900 MHz, with a resolution of 1 MHz and a high RF power of 40 dBm to ensure sufficient signal-to-noise ratio. The background fluctuations in the ODMR contrast are likely due to noise and instability in either the laser excitation or microwave delivery but are relatively minor compared to the depth of the resonance dip.

This result demonstrates that under room temperature conditions, stable and measurable ODMR contrast can be achieved in hBN emitters using modest external magnetic fields and high RF power. Notably, this was the only emitter among several flakes tested to show consistent ODMR contrast over several hours, suggesting either favorable orientation, local strain environment, or optimal emitter activation in this particular case.

4.8.1. Non Resonant Excitation

Spectral instability. Figure 4.31 portrays two representative examples of emitters: left(a)-(c) and right(d)-(f), showing spectral diffusion. Each show their ZPL at 50 mK with 532 nm excitation wavelength. These emitters have stable photon counts, meaning that they do not show blinking. In figures 4.31(a) and 4.31(d) a single scan of the ZPL is fit to Gaussian, Lorentzian and Voigt fits, the Gaussian is shown to have the best fit for these spectral measurements. The Gaussian shape arises primarily from inhomogeneous broadening mechanisms, most notably spectral diffusion. Spectral diffusion results from random fluctuations in the local electrostatic environment, such as those caused by charge traps or fluctuating dipoles near the emitter (as explained in theory section). These fluctuations lead to a statistical distribution of emission energies over time, and by the central limit theorem, such stochastic processes naturally yield Gaussian lineshape. In addition, inhomogeneities in strain, local dielectric environment, or lattice disorder can also contribute to a Gaussian distribution of emitter transition energies across a sample as seen for these emitters in 4.31(b) and (e) which show single scans of the ZPL taken over 60 frames with each scan integrated over 1 min. From an instrumental perspective, the finite resolution of the spectrometer further enforces a Gaussian response function due to the combined effects of grating dispersion, slit width, optical aberrations, and CCD pixel integration. While purely homogeneous broadening mechanisms would produce Lorentzian profiles, the instabilities resulting from non resonant excitation outweighs the homogeneous broadening that is always present even at at such low temperatures, making the Gaussian component dominant. Therefore, fitting the ZPL with a Gaussian function is both empirically justified and physically meaningful in the context of such photoluminescence measurements.

Right emitter in figure 4.31 shows more spectral diffusion than the left emitter in figure 4.31. In figure 4.31(d), the emitter showed spectral diffusion over a 1.4 THz range. These spectral instabilities hinder the likelihood of producing indistinguishable single photons. Furthermore, effects such as blinking, bleaching or spectral diffusion limit the optical coherence properties [133]. Spectral instabilities can be mitigated with a conductive surface or by selecting a substrate with higher purity, like Al_2O_3. Although emitter 4.31(a) exhibits reduced spectral diffusion, its relatively broad linewidth still renders photoluminescence excitation (PLE) spectroscopy unfeasible. In comparison, the second emitter displays an even broader linewidth of approximately 205 GHz, likely due to enhanced spectral broadening mechanisms. Figures 4.31(c) and (f) illustrate the temporal evolution of the emission spectra over the course of one hour.

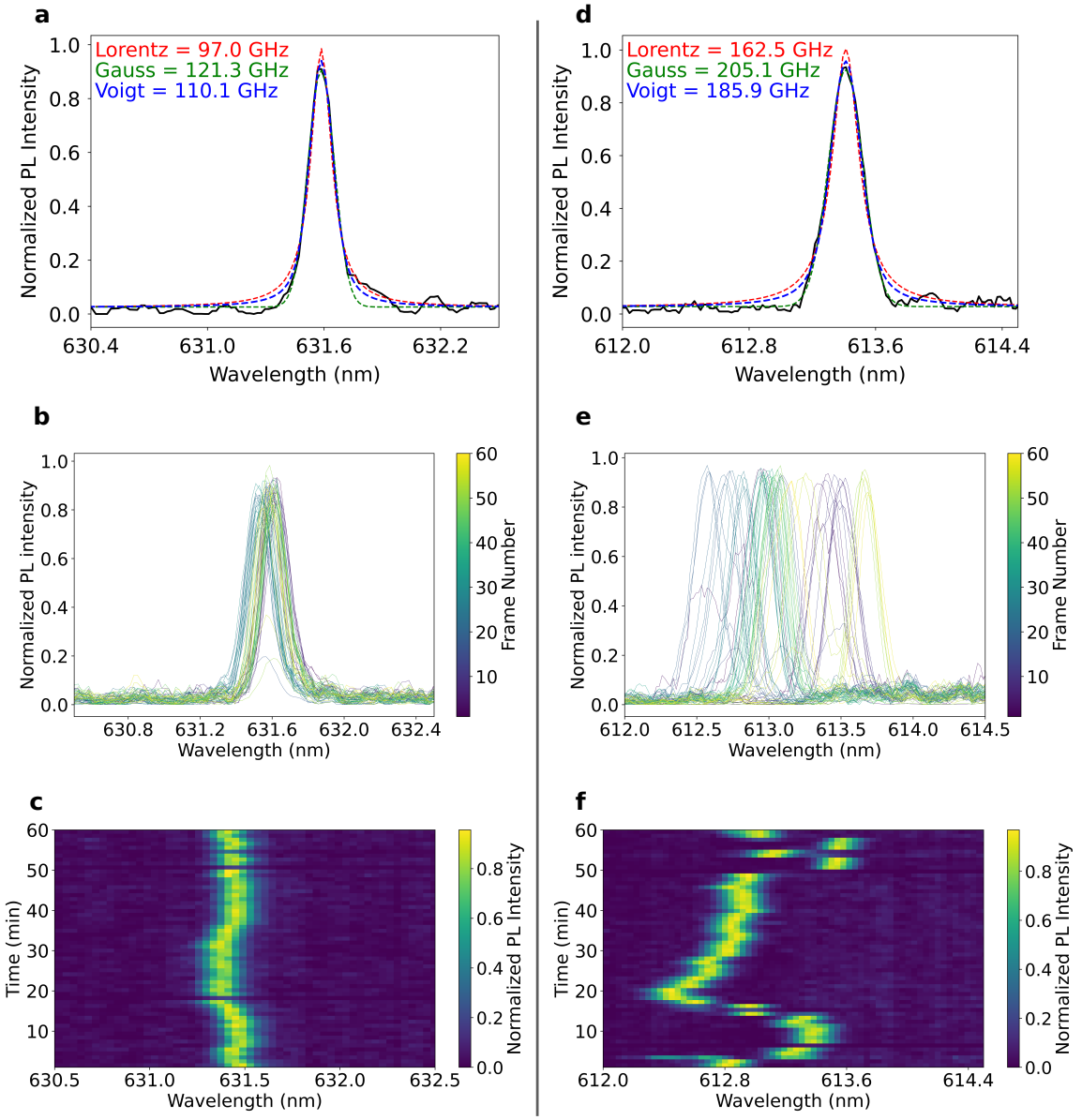

Figure 4.31.: Left (a)-(c) and right (d)-(f) are two different emitters with ZPL around 631.6 nm and 613.5 nm respectively. (a)& (d) show spectral fit on a single scan, with Gaussian being the accurate fit on the respective emitters. (b) and (e) show normalized ZPL over 1 hour, with each scan having an integration time of 1 min. (c) and (f) represent the measurement in (b) and (e) showing the spectral diffusion over time respectively.

Spectrally stable emitter. Figure 4.32 presents a representative stable emitter that exhibits no observable spectral diffusion under non-resonant excitation. As shown through an analysis analogous to that in Figure 4.31 (panels a, b, and c), the emitter in Figure 4.32 maintains a fixed ZPL position over time and features a relatively narrow linewidth of 97.7 GHz. Despite this apparent spectral stability, PLE measurements were unsuccessful, suggesting that the emission may either not be Fourier-limited or subject to rapid spectral jumps between metastable states, occurring on timescales too fast to resolve in time-averaged spectra.

Figures 4.32(d), (e) and (f) show the behaviour of this emitter in presence of external magnetic field, in the XY plane. The starting ZPL is at around 620 nm which then jumps to 618.4 nm and then settles in the centre wavelength at around 619.2 nm as seen in (e). The magnetic field direction corresponding to the jumps is presented in the polar plot in 4.32(f).

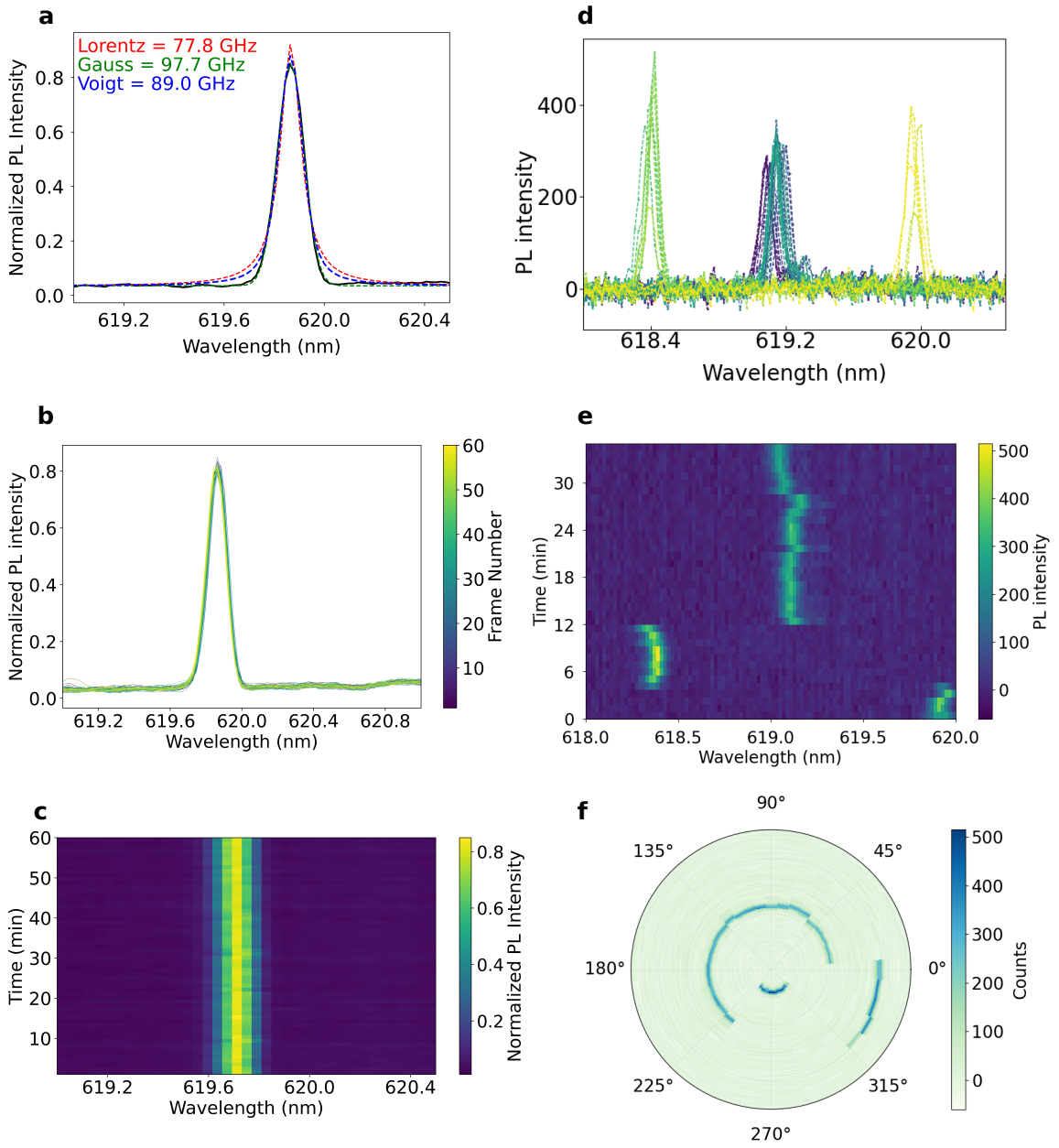

Figure 4.32.: Shows emitter with ZPL at 619.8 nm. On the left (a)-(c) are without magnetic field, on the right (d)-(f) are with magnetic field. (a) shows spectral fit on a single scan, with Gaussian being the accurate fit. (b) shows normalized ZPL over 1 hour, with each scan having an integration time of 1 min. (c) represents the measurement in (b) showing the spectral stability over time. (d)-(f) show the instabilities of the same emitter when an in plane magnetic field is applied.

4.8.2. Photoluminescence Excitation

Another example of a spectrally stable emitter is shown in Figure 4.33. Under non-resonant excitation, the ZPL remains stable over a 30-minute period, with a fitted linewidth over one of the single scan to be approximately 93,GHz. This emitter's ZPL (579.5 nm) falls within the spectral range of class A emitters, which are tentatively attributed to carbon trimer defects with a doublet spin configuration. Despite its spectral stability, the emitter exhibited power-dependent blinking at an excitation power of 10 µW, as shown in Figure 4.34. Notably, it was the only emitter to exhibit a detectable PLE signal, indicating resonant absorption and efficient excitation of the emissive state.

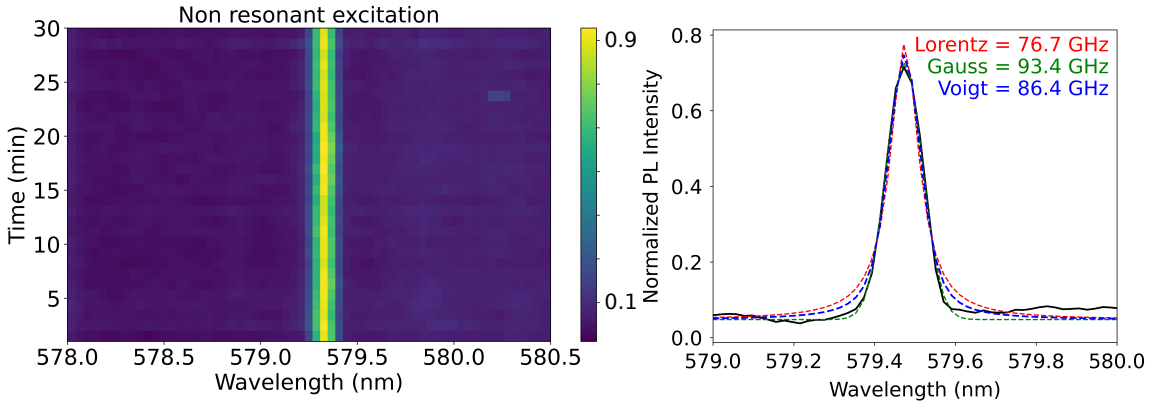

Figure 4.33.: Spectral map over time on the left and fitted linewidth of a single scan on the right.

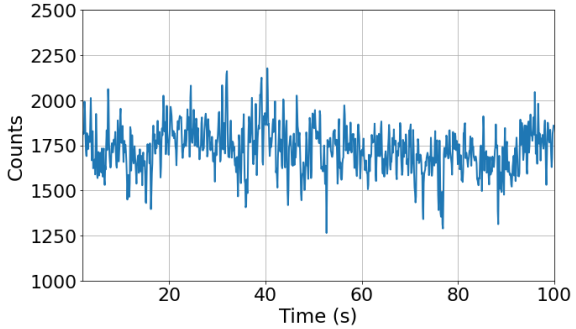

Figure 4.34.: Photon counts of the emitter which showed PLE, it showed blinking with 20 µW at non resonant excitation.

Figure 4.35 (left) illustrates the photoluminescence excitation (PLE) behavior of the emitter centered around 579.4 nm as it evolves over time. The emitter is resonantly excited by scanning a narrow-linewidth laser at across its absorption profile, while the resulting emission is collected through a 590 nm long-pass (LP) filter. This filter effectively suppresses the ZPL emission and selectively transmits the PSB, allowing for sensitive detection of resonant absorption events. In the left panel, the time-resolved PLE map illustrates the frequency shift of the emitter in relation to the initial frequency of 517.326 693 THz, extending over a considerable range of approximately ±500 MHz. Notably, the PLE resonance shows marked spectral wandering, transitioning between several distinct frequency positions over a period of 2.5 h. The corresponding frequency histogram (right) further supports this assessment, presenting a broad, multi-peaked distribution centered around 0 MHz, indicative of several preferred resonant frequencies. This implies underlying spectral diffusion phenomena, potentially driven by charge noise , local field variations or diverse emissive configurations. Notably, this measurement was performed using only 70 pW of excitation power, without any re-pumping from a green laser. Higher resonant excitation powers, as well as the introduction of non-resonant excitation at 532 nm, resulted in more pronounced spectral diffusion and broader frequency instability. Even at picowatt excitation levels, the addition of non-resonant excitation was found to induce spectral jumps on the order of gigahertz, often requiring the emitter frequency to be actively relocated. The linewidth of the resonant excitation laser line is given in Appendix figure A.12.

Linewidth distribution. Figure 4.36 shows the linewidth statistics of the emitter. The left panel presents a representative single-scan PLE spectrum fitted with a Lorentzian lineshape, indicating that the emission is homogeneously broadened on the timescale of the scan. This is a key indicator of transform-limited behavior, where the linewidth is dictated solely by the excited-state lifetime, with minimal contributions from spectral diffusion or pure dephasing during the measurement window.

In the following analysis (Figure 4.37), we compare this linewidth to the natural (lifetime-limited) linewidth derived from time-resolved photoluminescence measurements. The close agreement between the two values further supports that the emitter operates near the transform limit under resonant excitation, a highly desirable condition for coherent photon generation.

The right plot presents a probability distribution of full-width at half-maximum (FWHM) values extracted from multiple scans, with a mean linewidth of 53.75 MHz. This relatively narrow linewidth indicates that the emitter is coherently addressable at short timescales,

although long-term spectral instability would limit photon indistinguishability. Together, the data reveal a system with promising coherence at the emission level, but with significant frequency drift requiring stabilization for quantum optical applications.

The lifetime of the emitter in its excited state was determined to be 4.08 ns as shown in figure 4.37 when measured at a resonant frequency of 517.326 693 THz using time-correlated single-photon counting. This yields a Fourier-transform-limited linewidth, given by $f = \frac{1}{2\pi\tau} = 39.01$ MHz. The PLE linewidth of the emitter, 53.75 MHz, is not far from the natural linewidth of the emitter, implying slight dephasing beyond the natural lifetime limit. The single dominant exponential decay pathway with no long lived shelving state indicate a two level system approximation.

Our PLE measurements demonstrate a significant advancement over previously reported results. In contrast to earlier studies where spectral diffusion and linewidth broadening limited the resolution of resonant features—for example, Tran et al. reported linewidths narrowing to ~700 MHz in individual scans under active spectral diffusion [134] and Dietrich et al. extracted a homogeneous linewidth of 124.5±60.5 MHz across 204 scans with an inhomogeneous distribution of 67.5±9.5 GHz [77]—our emitter exhibits Fourier

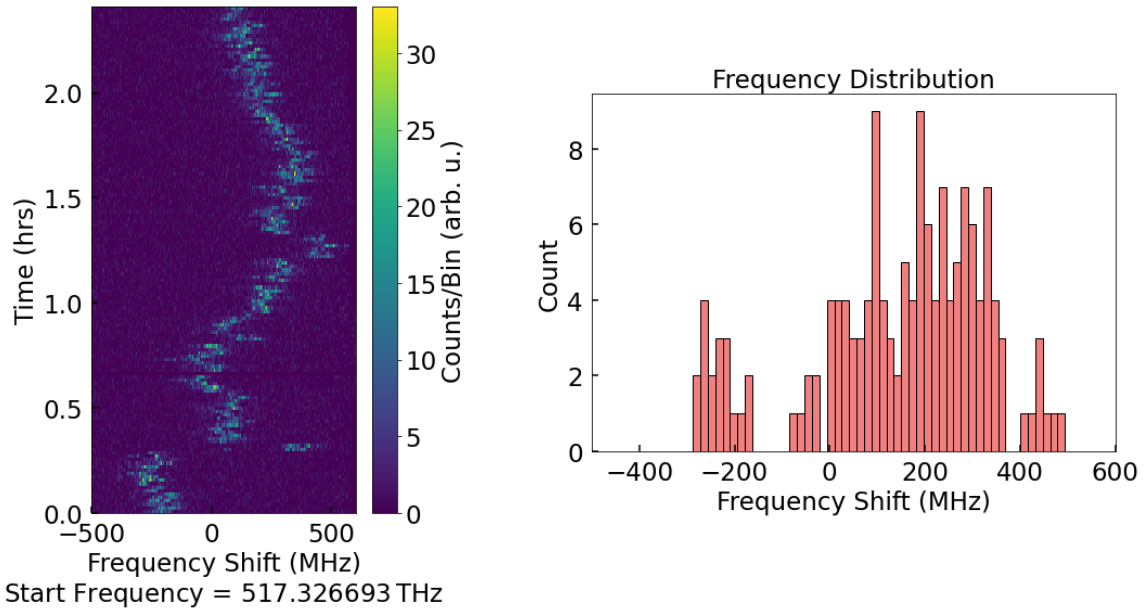

Figure 4.35.: On the left, the time-resolved PLE map showing the frequency shift of the emission line over a period of ~2.2 h. The data is referenced to a starting absolute frequency of 517.326 693 THz. Color scale indicates photon counts. On the right is the histogram of frequency shifts extracted from the time series, showing the distribution of emission frequency fluctuations. The emitter exhibits a drift as well as intermittent spectral jumps, indicating spectral diffusion likely due to local charge fluctuations or environmental perturbations.

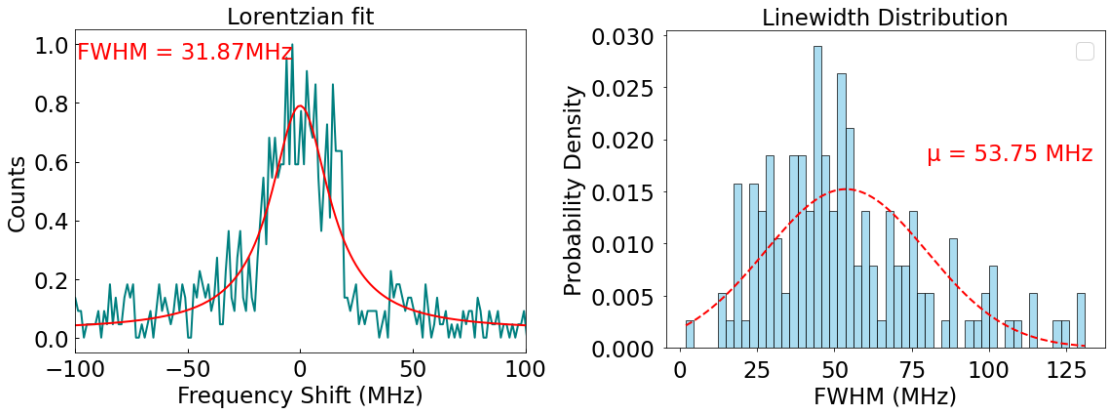

Figure 4.36.: Left shows Lorentzian fit to a single scan at resonant excitation. Right shows the linewidth distribution to show the average linewidth to be 53.56 MHz.

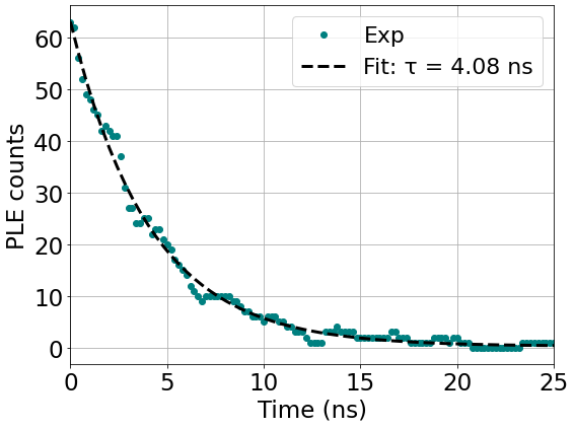

Figure 4.37.: Lifetime decay at resonant excitation.

Transform limited linewidths with a linewidth average of 53.75 ± 26.21 MHz across 147 scans, approaching the lifetime-limited value of 39 MHz (from a measured lifetime of 4 ns). It has consistently stable ZPL under non-resonant excitation. We achieve a spectral diffusion of only ~1 GHz during PLE measurements. These results represent the narrowest and most stable PLE response reported to date for quantum emitters in hBN with PLE measurements, highlighting the potential of our system for coherent optical control.

4.8.2.1. PLE with External Magnetic Field

Further PLE measurements are carried out on the same emitter using angular magnetic field sweep in order to investigate the spin system of the emitter. The vector magnet is controlled via a Python script interfaced with an ADwin system, which continuously manages the output voltages from digital-to-analog converters (DACs) connected to three orthogonal pairs of Helmholtz coils. These voltages correspond to the magnetic field components along the lab xx-, yy-, and zz-axes, enabling full 3D control of the magnetic field vector. When a new field configuration is requested, the script applies updated DAC values at a controlled ramp rate (V=0.1 V/sV=0.1V/s) to smoothly adjust the field without interrupting system stability. Once the target field is reached and verified, the script triggers the photoluminescence excitation (PLE) measurement, ensuring precise field alignment for each scan. More details on the setup can be found in the PhD work of Ioannis Karapatzakis [135].

Figure 4.38 and figure 4.39 show (PLE) maps and corresponding polar plots of the emitter under a static magnetic field of 400 mT, recorded in two orthogonal rotation planes: XY (figure 4.38) and YZ (figure 4.39). No splitting is observed due to the external magnetic field indicating that this particular emitter might be spin neutral.

While the ZPL of this emitter aligns with that of the carbon trimer, the expectation is that it possesses a spin doublet configuration. Consequently, it is plausible to infer that this emitter, which has demonstrated photoluminescence excitation (PLE), might exhibit varying charge states and exhibit a neutral spin. A potential candidate for this emitter could be one of the C_BC_N-DAP defects [55]. These defects consist of neighboring carbon–boron–nitrogen vacancies (C_BC_N) associated with a diatomic acceptor–donor pair (DAP), featuring mid-gap energy levels that can either accept or donate electrons. This defect can exist in multiple charge states, each associated with a distinct spin configuration. Although the neutral point defects (C_B, C_N) are paramagnetic, their interaction results in non-paramagnetic assemblies C_BC_N-DAPs with "charge structure" $C^+B\text{-}C^=N$, as it is energetically advantageous to transfer the unpaired electron from C_B to C_N. As depicted in Table 2.1, the neutral state of this carbon DAP is also spin-neutral and could potentially reside within the ZPL range of interest.

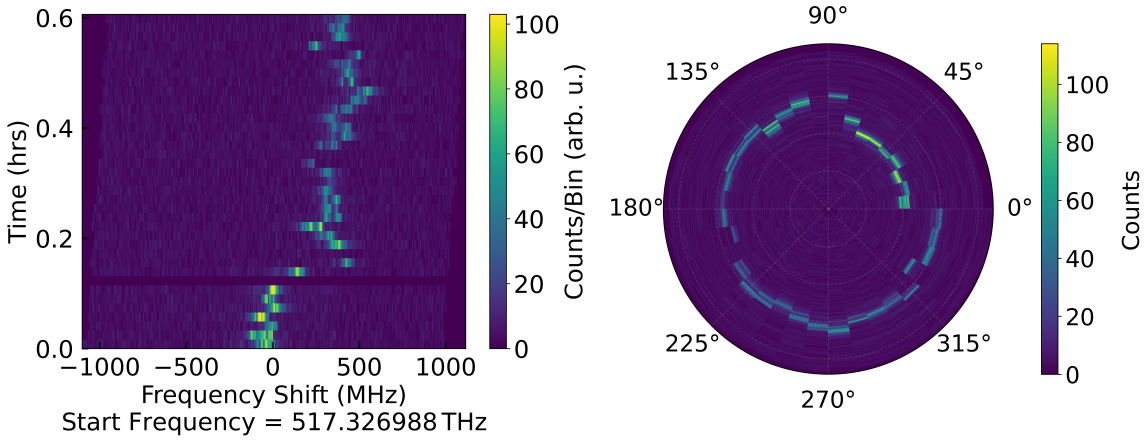

Figure 4.38.: Shows PLE map at 400 mT in XY rotation plane (left) and the corresponding polar plot.

This study presents a significant advancement in the resonant optical control of quantum emitters in hexagonal boron nitride (hBN), particularly in the context of photoluminescence excitation (PLE) measurements. While many emitters investigated under off-resonant excitation showed substantial spectral diffusion and broad Gaussian lineshapes due to environmental charge noise and strain inhomogeneities, some showed continuous spectral stability under non resonant excitation with narrow linewidths, among them, one spectrally stable emitter with a zero-phonon line at 579.5 nm consistently exhibited detectable PLE. Compared to earlier studies where PLE was hindered by strong spectral diffusion and limited coherence—such as Tran *et al.* reporting ~700 MHz linewidths and Dietrich *et al.* extracting 124.5 ± 60.5 MHz homogeneous linewidths from inhomogeneous ensembles—our emitter demonstrates a **mean linewidth of 53.75 ± 26.21 MHz**, approaching the **lifetime-limited linewidth of 39 MHz** derived from a 4.08 ns excited-state lifetime.

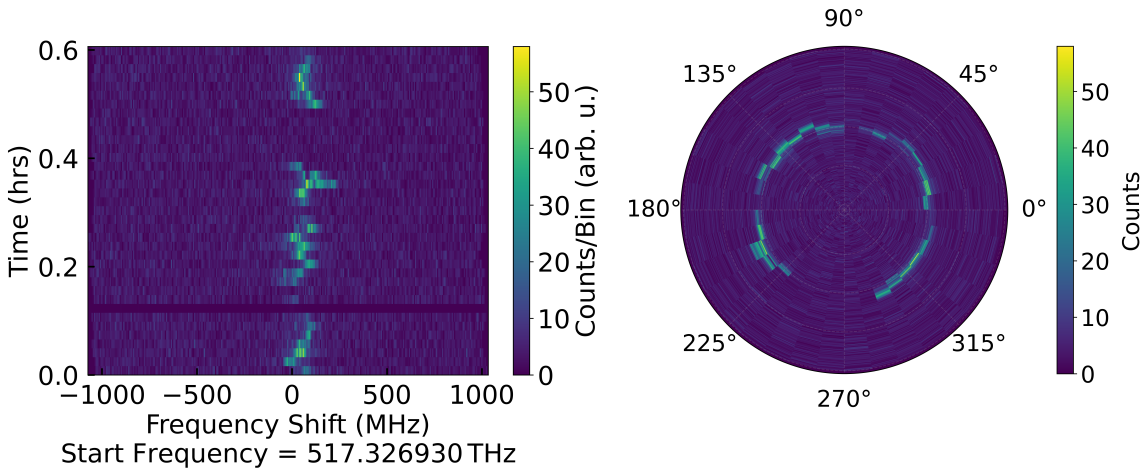

Figure 4.39.: Shows PLE map at 400 mT in YZ rotation plane (left) and the corresponding polar plot.

This is the narrowest and most stable PLE response reported to date in hBN. Even under ultra-low resonant excitation power (70 pW) without repumping, the emitter maintained coherence with only ~1 GHz spectral diffusion over 2.5 hours. Furthermore, despite magnetic field application up to 400 mT using a vector magnet, no spin splitting was observed, suggesting a spin-neutral charge state, likely associated with a C_BC_N-DAP defect configuration. Altogether, these findings mark a substantial improvement in spectral stability and coherence over previous works and underscore the potential of hBN emitters for future quantum photonics applications requiring resonant control.

4.9. Challenges and Pointers

This section is especially intended for readers who are also working with fabricating quantum emitters in hBN. For those comrades in this exciting journey of frustration, I would like to offer some pointers of possible problems you might face and what could be helpful. Of course, this is highly dependent on the main goal of your fabrication, but putting them in line or similar to our goals in this thesis, I shall suggest away. I have mentioned these points sporadically throughout the thesis and would like to summarize them here.

Adsorbates and charge build up: these are two of the main environmental sources I deduce to be the culprit for poor quality SPE and blinking emitters, and which may be somewhat avoided with care. Although extra steps are taken to obtain a clean, assumedly stable emitter at RT, the local environment of the emitters may still show instabilities at low temperatures. The best chances are to start clean and keep clean with sample fabrication and for chip device integration.

- After exfoliation, check the topography of the flake with AFM to see if it is free of surface adsorbates. A roughness on the picometer scale is good. If you see bubbles and many adsorbates on most of the flakes from the exfoliation process, revisit your technique of exfoliation, and I would suggest making fresh batches. Clean with acetone and IPA solution after exfoliation. Contact AFM cleaning can help remove debris on selected regions if AFM nanoindentation is the choice of fabrication. However, too many adsorbates and bubbles degrade the flake surface during annealing. Adsorbates accelerate etching during annealing, which creates ensemble emitters and a complicated local environment for the emitter. Moreover, contact AFM cleaning reduces the yield of emitters, so it is best to start with a clean flake and then directly proceed to nanoindentation after checking the topography with AFM.
- If you notice that after annealing, the background count on the flake is too high (clean hBN should have similar fluorescence counts as the SiO_2 substrate), bleach the sample with high power, for example, a couple of milliwatts. This reduces charge build up and bleaches any luminescent organic adsorbates that might have contaminated your sample. This also gets rid of emitters that will bleach anyway and saves measurement time. Most stable emitters in hBN stay stable even after such high laser powers.

- During annealing, the degassing step should not be skipped—this gets rid of any adhesive that could be left over from exfoliation.
- Once emitters are created, they are not affected by dirt from ambient conditions. They are robust. However, if you are covering them with photoresist for further fabrication processes, the quality of the emitters might be affected. Photoresists and PMMA have been shown not to be completely removed after lithography. Below shows pictures of electrodes fabricated after the emitters in the hBN flake were fabricated for studying Stark effect. If the flake is being transferred after fabrication, then it should be suspended during annealing; otherwise, it is hard to remove from the sample.

Naturally occurring defects: these are inherent defects in hBN. If your fabrication goals do not require them, it is better to use high-purity single crystals. It is more likely to have a narrower class of emitters from the chosen fabrication technique.

In conclusion, I would like to point out that, like most interesting systems such as SnV or NV^-, finding an excellent quantum emitter on which coherent measurements can be carried out is not abundant. The difficulties in fabrication and determining defect electronic states, especially at this relatively early stage of research, do not diminish the appeal of hBN as a quantum material. With continued collective effort from the research community, hBN is likely to further demonstrate its potential as a robust platform for quantum technologies.

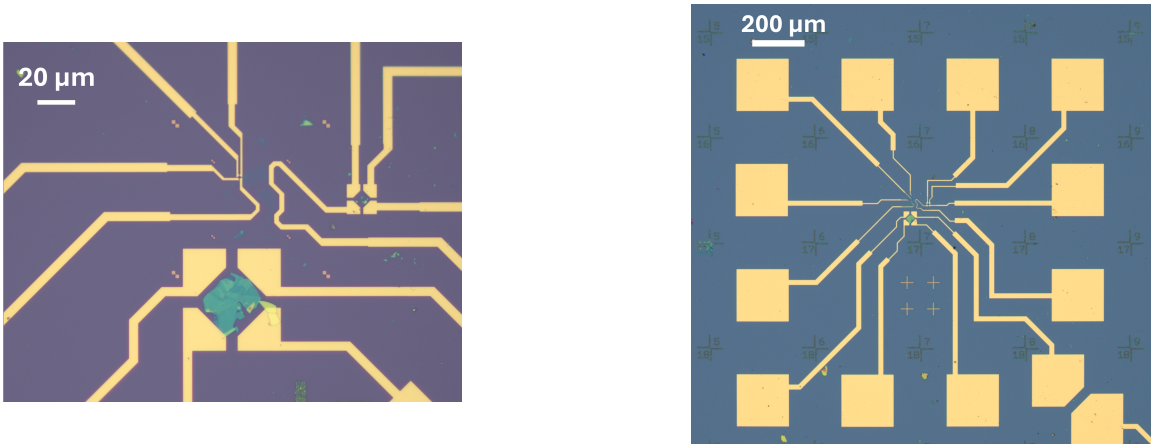

Figure 4.40.: Patterned electrodes around hBN flake fabricated for SPEs.

5. Conclusion

AFM nanoindentation followed by thermal annealing provides a controlled route to generate stable SPEs in hBN. The method yields a high density of isolated carbon-related defects mainly attributed to the C_2C_N carbon trimer [49, 56] with narrow linewidths, dominant emission in ZPL, and excellent spectral stability.

The properties of the emitters are strongly influenced by the annealing conditions. Excessive etching due to elevated Ar flow or air exposure [136, 137] increases the clustering of defects and surface roughness. Optimizing Ar flow and surface cleanliness are crucial for precise emitter formation and removes surface adsorbates and trapped bubbles [88]. An unconventional cleaning step for hBN which is contact AFM scanning, which resulted in reduced etching effect. Higher voltages of contact scanning has shown strain response via wrinkling.

hBN defects are highly sensitive to their local atomic environment, and even slight modifications in the fabrication process can influence their deterministic formation. Although this sensitivity can make fabrication more demanding, the emitters created via nanoindentation have proven to be remarkably robust. Once formed, they remain stable for two years or more under ambient conditions. For instance, the sample used for the PLE measurements discussed in Section 4.8.2 was fabricated in August 2023, and the measurements were carried out in May 2025—without requiring any reactivation or cleaning steps prior to re-measurement. These results and process insights highlight a scalable, charge-neutral route for SPE engineering, enabling the formation of single, isolated carbon defects.

The emitters are shown to be robust in presence of single molecule magnet such $TbPc_2$. Single or ensemble $TbPc_2$ on the emitter supposedly induces an antennae effect, which sensitizes the electronic level system (for defect types where the energy down conversion is allowed) resulting higher emission efficiency of many of SPE. RT ODMR signal was seen in one emitter where RF was applied via an antennae. Low temperature measurements provided more insight into the different spectral instabilities that cannot be seen

at RT. We have seen that emitters with random blinking can show FT limited linewidth. Photoluminescence excitation (PLE) measurements were successfully performed on this emitter, enabling estimation of its excited-state lifetime and natural linewidth, which are critical parameters for evaluating coherence and suitability for quantum applications. It was deduced that this emitters has spin 0 state and is probably one of the C_BC_N- donor acceptor pair (DAP)s with multiple optically active charge states.

5.1. Outlook

hBN quantum emitters were first reported in 2016 by Tran and colleagues at the University of Technology Sydney, Australia. Despite growing interest, much remains unknown about the nature of the defect systems that give rise to these emitters. Notably, a reliable method to reproducibly generate a single, well-defined defect type has yet to be established. Any such fabrication technique must also suppress the formation of other, unintended defects—a challenge that remains unresolved.

The field has not yet reached the point where an emitter can be definitively identified as, for instance, a carbon trimer based on direct experimental evidence. Currently, identifications are largely inferential, relying on comparison with theoretical models. However, as discussed in the results chapter, external factors such as strain and local environmental changes can shift the emitter's zero-phonon line (ZPL), and the broad spectral linewidths at room temperature further complicate ZPL assignment. Moreover, there is a gap between theory and experiment: some theoretical models appear to underestimate ZPL energies, likely due to insufficient treatment of excitonic effects via the Bethe–Salpeter Equation (BSE). Most existing fabrication methods are based on damaging B–N bonds, leading to vacancies and dangling bonds—features not always fully captured in theoretical models. Additionally, while hBN quantum emitters are generally assumed to lie on or near the surface, little to no work has explored the possibility that emitters could form within subsurface regions or craters—an intriguing possibility with techniques like AFM nanoindentation.

A more productive approach to understanding hBN defects may lie in narrowing focus: reproducibly creating and studying a single class of emitter in depth. Techniques such as ODMR and PLE could be used to uncover their energy-level structure. Coordinated experimental and theoretical efforts would be essential in achieving this. Higher-resolution AFM scans at low temperatures could provide further spatial and structural insight, while

switching from Si to Al_2O_3 substrates may help reduce low-temperature spectral instabilities.

That said, the very fact that so much remains to be explored makes hBN quantum emitters a particularly fascinating platform. Their potential for engineering—toward quantum communication and nanoscale sensing—remains strong. Through this work, several follow-up directions and open questions have emerged:

First, more PLE measurements are needed on emitters believed to be carbon trimers, ideally at low temperatures, with an optimized substrate and functioning waveguide. Since this defect is expected to have a spin doublet ground state, it should exhibit Zeeman splitting under an external magnetic field. This would enable further coherence studies and help refine our understanding of the energy-level structure. Demonstrating Zeeman splitting would also significantly strengthen the claim that emitters around 580 nm originate from carbon trimers.

Second, the interaction between emitters near 580 nm and evaporated $TbPc_2$ molecules requires further investigation. More samples with low coverage of $TbPc_2$ should be prepared to examine potential effects on the emitters. Similar experiments using phthalocyanine (Pc) ligands alone should also be carried out, as it is possible that the double-decker $TbPc_2$ complex breaks during evaporation, leaving only the ligands on the surface. Once a stable emitter with well-resolved spin properties is identified, it would be especially interesting to study its interaction with the magnetic centre of such molecules. In any case, if enhanced spectral signal is reproducible then this could be an important finding, it would show that molecules could be used to enhance signal as is done with optical cavities.

Third, the influence of nearby charge environments on SPE stability should be explored. Depositing hBN flakes directly onto metallic electrodes could help suppress charge noise and improve photophysical stability. Comparing emitter performance in such configurations may offer insights into controlling charge fluctuations.

Lastly, strain engineering remains a largely unexplored area in hBN quantum photonics. This work reports that wrinkling can be induced via contact-mode AFM scanning—a technique initially used for surface cleaning. Although this finding was not pursued further, it suggests the potential to activate or modulate optical defects through localized strain, which warrants deeper investigation.

Bibliography

[1] Marco Gilardoni, Cian Eizagirre Barker, Conor L. Curtin, et al. "A single spin in hexagonal boron nitride for vectorial quantum magnetometry". In: *Nature Communications* 16 (2025), p. 4947. DOI: 10.1038/s41467-025-59642-0. URL: https://doi.org/10.1038/s41467-025-59642-0.

[2] Hannah L. Stern et al. "A quantum coherent spin in hexagonal boron nitride at ambient conditions". In: *Nature Materials* 23.10 (May 2024). Epub 2024 May 20. PMID: 38769205, pp. 1379–1385. DOI: 10.1038/s41563-024-01887-z. URL: https://doi.org/10.1038/s41563-024-01887-z.

[3] Hamidreza Akbari et al. "Temperature-dependent Spectral Emission of Hexagonal Boron Nitride Quantum Emitters on Conductive and Dielectric Substrates". In: *Physical Review Applied* 15 (1 Jan. 2021). ISSN: 23317019. DOI: 10.1103/PhysRevApplied.15.014036.

[4] J. Wrachtrup, S. Y. Kilin, and A. P. Nizovtsev. "Quantum computation using the ^{13}C nuclear spins near the single NV defect center in diamond". In: *Optics and Spectroscopy* 91.3 (2001), pp. 429–437. DOI: 10.1134/1.1405224.

[5] L. Childress et al. "Coherent dynamics of coupled electron and nuclear spin qubits in diamond". In: *Science* 314.5797 (2006), pp. 281–285. DOI: 10.1126/science.1131871.

[6] T. Gaebel et al. "Room-temperature coherent coupling of single spins in diamond". In: *Nature Physics* 2 (2006), pp. 408–413. DOI: 10.1038/nphys318.

[7] J. M. Taylor et al. "High-sensitivity diamond magnetometer with nanoscale resolution". In: *Nature Physics* 4 (2008), pp. 810–816. DOI: 10.1038/nphys1075.

[8] Nai Jie Guo et al. "Coherent control of an ultrabright single spin in hexagonal boron nitride at room temperature". In: *Nature Communications* 14 (1 2023), p. 2893. ISSN: 20411723. DOI: 10.1038/s41467-023-38672-6.

[9] Igor Aharonovich, Jean Philippe Tetienne, and Milos Toth. "Quantum Emitters in Hexagonal Boron Nitride". In: *Nano Letters* 22 (23 2022), pp. 9227–9235. ISSN: 15306992. DOI: 10.1021/acs.nanolett.2c03743.

[10] Stefania Castelletto et al. “Hexagonal boron nitride: A review of the emerging material platform for single-photon sources and the spin-photon interface”. In: *Beilstein Journal of Nanotechnology* 11 (2020), pp. 740–769. ISSN: 21904286. DOI: 10.3762/bjnano.11.61.

[11] Cong Su et al. “Fundamentals and emerging optical applications of hexagonal boron nitride: a tutorial”. In: *Advances in Optics and Photonics* 16 (2 June 2024), p. 229. ISSN: 19438206. DOI: 10.1364/aop.502922.

[12] Hannah L. Stern et al. “Spectrally Resolved Photodynamics of Individual Emitters in Large-Area Monolayers of Hexagonal Boron Nitride”. In: *ACS Nano* 13 (4 Apr. 2019), pp. 4538–4547. ISSN: 1936-0851. DOI: 10.1021/acsnano.9b00274.

[13] Bernd Sontheimer et al. “Photodynamics of quantum emitters in hexagonal boron nitride revealed by low-temperature spectroscopy”. In: *Physical Review B* 96 (12 2017), pp. 1–5. ISSN: 24699969. DOI: 10.1103/PhysRevB.96.121202.

[14] Marie Krečmarová et al. “Extrinsic Effects on the Optical Properties of Surface Color Defects Generated in Hexagonal Boron Nitride Nanosheets”. In: *ACS Applied Materials & Interfaces* 13 (38 Sept. 2021), pp. 46105–46116. ISSN: 1944-8244. DOI: 10.1021/acsami.1c11060.

[15] Sylvia Xin Li et al. “Prolonged photostability in hexagonal boron nitride quantum emitters”. In: *Communications Materials* 4 (1 Dec. 2023), p. 19. ISSN: 26624443. DOI: 10.1038/s43246-023-00345-8.

[16] Hannah L. Stern et al. “Room-temperature optically detected magnetic resonance of single defects in hexagonal boron nitride”. In: *Nature Communications* 13 (1 2022), pp. 1–9. ISSN: 20411723. DOI: 10.1038/s41467-022-28169-z.

[17] Xingyu Gao et al. “High-Contrast Plasmonic-Enhanced Shallow Spin Defects in Hexagonal Boron Nitride for Quantum Sensing”. In: *Nano Letters* 21 (18 2021), pp. 7708–7714. ISSN: 15306992. DOI: 10.1021/acs.nanolett.1c02495.

[18] Andreas Gottscholl et al. “Spin defects in hBN as promising temperature, pressure and magnetic field quantum sensors”. In: *Nature Communications* 12 (1 2021), pp. 6–13. ISSN: 20411723. DOI: 10.1038/s41467-021-24725-1. URL: http://dx.doi.org/10.1038/s41467-021-24725-1.

[19] Annemarie L. Exarhos et al. “Optical Signatures of Quantum Emitters in Suspended Hexagonal Boron Nitride”. In: *ACS Nano* 11 (3 2017), pp. 3328–3336. ISSN: 1936086X. DOI: 10.1021/acsnano.7b00665.

[20] Akbar Basha Dhu al Shaik, Penchalaiah Palla, and David Jenkins. "Electrical tuning of quantum light emitters in hBN for free space and telecom optical bands". In: *Scientific Reports* 14.1 (2024), p. 811. ISSN: 2045-2322. DOI: 10.1038/s41598-024-51504-x. URL: https://doi.org/10.1038/s41598-024-51504-x.

[21] Gichang Noh et al. "Stark Tuning of Single-Photon Emitters in Hexagonal Boron Nitride". In: *Nano Letters* 18.8 (June 2018), pp. 4710–4715. ISSN: 1530-6992. DOI: 10.1021/acs.nanolett.8b01030. arXiv: 1807.04945. URL: https://pubs.acs.org/doi/full/10.1021/acs.nanolett.8b01030.

[22] Alessio Scavuzzo et al. "Electrically tunable quantum emitters in an ultrathin graphene–hexagonal boron nitride van der Waals heterostructure". In: *Applied Physics Letters* 114.6 (Feb. 2019). ISSN: 0003-6951. DOI: 10.1063/1.5067385. URL: https://aip.scitation.org/doi/abs/10.1063/1.5067385.

[23] Lin Gan et al. "Large-Scale, High-Yield Laser Fabrication of Bright and Pure Single-Photon Emitters at Room Temperature in Hexagonal Boron Nitride". In: *ACS Nano* 16 (9 Sept. 2022), pp. 14254–14261. ISSN: 1936086X. DOI: 10.1021/acsnano.2c04386.

[24] Guan Lin Liu et al. "Single Photon Emitters in Hexagonal Boron Nitride Fabricated by Focused Helium Ion Beam". In: *Advanced Optical Materials* 12 (9 2024), pp. 1–9. ISSN: 21951071. DOI: 10.1002/adom.202302083.

[25] Evgenii Glushkov et al. "Engineering Optically Active Defects in Hexagonal Boron Nitride Using Focused Ion Beam and Water". In: *ACS Nano* 16 (3 Mar. 2022), pp. 3695–3703. ISSN: 1936086X. DOI: 10.1021/acsnano.1c07086.

[26] James Callum Stewart et al. "Quantum Emitter Localization in Layer-Engineered Hexagonal Boron Nitride". In: *ACS Nano* 15 (8 Aug. 2021), pp. 13591–13603. ISSN: 1936086X. DOI: 10.1021/acsnano.1c04467.

[27] Clarisse Fournier et al. "Position-controlled quantum emitters with reproducible emission wavelength in hexagonal boron nitride". In: *Nature Communications* 12 (1 Dec. 2021), p. 3779. ISSN: 20411723. DOI: 10.1038/s41467-021-24019-6.

[28] Clément Godfrin. "Quantum information processing using a molecular magnet single nuclear spin qudit". Theses. Université Grenoble Alpes, Apr. 2017. URL: https://theses.hal.science/tel-01648035.

[29] Mengfei Wang and Kazuyuki Ishii. *Photochemical properties of phthalocyanines with transition metal ions*. Oct. 2022. DOI: 10.1016/j.ccr.2022.214626.

[30] A. E. Naclerio and P. R. Kidambi. "A Review of Scalable Hexagonal Boron Nitride (h-BN) Synthesis for Present and Future Applications". In: *Advanced Materials* 35.6 (2023), e2207374. DOI: 10.1002/adma.202207374. URL: https://doi.org/10.1002/adma.202207374.

[31] Joshua D. Caldwell et al. "Photonics with Hexagonal Boron Nitride". In: *Nature Reviews Materials* 4 (2019), pp. 552–567. DOI: 10.1038/s41578-019-0124-1. URL: https://doi.org/10.1038/s41578-019-0124-1.

[32] T. N. A. Mai et al. "Quantum Emitters in Hexagonal Boron Nitride: Principles, Engineering and Applications". In: *arXiv preprint arXiv:2501.12677* (2025). URL: https://arxiv.org/abs/2501.12677.

[33] R. S. Pease. "An X-ray Study of Boron Nitride". In: *Acta Crystallographica* 5 (1952), pp. 356–361. DOI: 10.1107/S0365110X52001064. URL: https://doi.org/10.1107/S0365110X52001064.

[34] Csongor Imre. *Creation of defects as hosts for single photon emitters in hexagonal boron nitride with the nano-indentation technique and investigation of thermal annealing effects on surface quality and emitter properties.* 2025.

[35] Li Song and et al. "Large Scale Growth and Characterization of Atomic Hexagonal Boron Nitride Layers". In: *Nano Letters* 10 (2010), pp. 3209–3215. DOI: 10.1021/nl1022139. URL: https://doi.org/10.1021/nl1022139.

[36] Jingang Wang, Fengcai Ma, and Mengtao Sun. "Graphene, hexagonal boron nitride, and their heterostructures: properties and applications". In: *RSC Advances* 7.27 (Mar. 2017). Accessed: 2025-02-21, pp. 16801–16822. ISSN: 2046-2069. DOI: 10.1039/C7RA00260B. URL: https://pubs.rsc.org/en/content/articlelanding/2017/ra/c7ra00260b.

[37] R. V. Gorbachev et al. "Hunting for monolayer boron nitride: Optical and Raman signatures". In: *Small* 7.4 (2011), pp. 465–468. DOI: 10.1002/smll.201001628.

[38] P. Blake et al. "Making graphene visible". In: *Applied Physics Letters* 91.6 (2007), p. 063124. DOI: 10.1063/1.2768624.

[39] Yuto Anzai et al. "Broad range thickness identification of hexagonal boron nitride by colors". In: *Applied Physics Express* 12.5 (2019), p. 055007. ISSN: 1882-0786. DOI: 10.7567/1882-0786/ab0e45. URL: https://doi.org/10.7567/1882-0786/ab0e45.

[40] K. Watanabe, T. Taniguchi, and H. Kanda. "Direct-bandgap properties and evidence for ultraviolet lasing of hexagonal boron nitride single crystal". In: *Nature Materials* 3.6 (2004), pp. 404–409. DOI: 10.1038/nmat1134.

[41] R. M. Ribeiro and N. M. R. Peres. "Stability of boron nitride bilayers: Ground-state energies, interlayer distances, and tight-binding description". In: *Physical Review B: Condensed Matter and Materials Physics* 83.23 (2011), p. 235312. DOI: 10.1103/PhysRevB.83.235312.

[42] Shohei Fukamachi et al. "Large-area synthesis and transfer of multilayer hexagonal boron nitride for enhanced graphene device arrays". In: *Nature Electronics* 6 (2023), pp. 126–136. DOI: 10.1038/s41928-022-00911-x. URL: https://doi.org/10.1038/s41928-022-00911-x.

[43] Toan Trong Tran et al. "Quantum emission from hexagonal boron nitride monolayers". In: *Nature Nanotechnology* 11 (1 2016), pp. 37–41. ISSN: 17483395. DOI: 10.1038/nnano.2015.242.

[44] Nathan Chejanovsky et al. "Single-spin resonance in a van der Waals embedded paramagnetic defect". In: *Nature Materials* 20 (8 Aug. 2021), pp. 1079–1084. ISSN: 14764660. DOI: 10.1038/s41563-021-00979-4.

[45] A. Gottscholl et al. "Room temperature initialization and read-out of intrinsic spin defects in a van der Waals crystal". In: *Nature Materials* 19 (2020), pp. 540–545. DOI: 10.1038/s41563-020-0619-6. URL: https://doi.org/10.1038/s41563-020-0619-6.

[46] Noah Mendelson et al. "Identifying carbon as the source of visible single-photon emission from hexagonal boron nitride". In: *Nature Materials* 20 (3 2021), pp. 321–328. ISSN: 14764660. DOI: 10.1038/s41563-020-00850-y. URL: http://dx.doi.org/10.1038/s41563-020-00850-y.

[47] Mark E. Turiansky et al. "Dangling Bonds in Hexagonal Boron Nitride as Single-Photon Emitters". In: *Physical Review Letters* 123 (12 Sept. 2019). ISSN: 10797114. DOI: 10.1103/PhysRevLett.123.127401.

[48] A. Sajid, Michael J. Ford, and Jeffrey R. Reimers. "Single-photon emitters in hexagonal boron nitride: a review of progress". In: *Reports on Progress in Physics* 83 (4 2020). ISSN: 00344885. DOI: 10.1088/1361-6633/ab6310.

[49] Wei Liu et al. "Spin-active defects in hexagonal boron nitride". In: *Materials for Quantum Technology* 2.3 (2022), p. 032002. DOI: 10.1088/2633-4356/ac7e9f. URL: https://dx.doi.org/10.1088/2633-4356/ac7e9f.

[50] L. Museur, E. Feldbach, and A. Kanaev. "Defect-related photoluminescence of hexagonal boron nitride". In: *Journal of Applied Physics* 103.10 (2008), p. 103520. DOI: 10.1063/1.2924771.

[51] L. Weston et al. “Native Point Defects and Impurities in Hexagonal Boron Nitride”. In: *Physical Review B* 97.21 (2018), p. 214104. DOI: 10.1103/PhysRevB.97.214104. URL: https://doi.org/10.1103/PhysRevB.97.214104.

[52] S. Smidstrup et al. “QuantumATK: An Integrated Platform of Electronic and Atomic-Scale Modelling Tools”. In: *Journal of Physics: Condensed Matter* 32.1 (2020), p. 015901. DOI: 10.1088/1361-648X/ab4007.

[53] Ding Zhong et al. “Carbon-Related Quantum Emitter in Hexagonal Boron Nitride with Narrow Emission Linewidth and Aligned Dipole Orientation”. In: *Nano Letters* 24.4 (2024), pp. 1106–1113. DOI: 10.1021/acs.nanolett.3c03628. URL: https://doi.org/10.1021/acs.nanolett.3c03628.

[54] Tingli N. A. Du et al. “Carbon Defects Engineering in Hexagonal Boron Nitride for Single Photon Emission and Spin Qubits”. In: *AIP Advances* 2.2 (2025), p. 026127. DOI: 10.1063/5.XXXXXXX.

[55] Philipp Auburger and Adam Gali. “Towards ab initio identification of paramagnetic substitutional carbon defects in hexagonal boron nitride acting as quantum bits”. In: *Phys. Rev. B* 104 (7 2021), p. 075410. DOI: 10.1103/PhysRevB.104.075410. URL: https://link.aps.org/doi/10.1103/PhysRevB.104.075410.

[56] Kejun Li, Tyler J. Smart, and Yuan Ping. “Carbon trimer as a 2 eV single-photon emitter candidate in hexagonal boron nitride: A first-principles study”. In: *Phys. Rev. Mater.* 6 (4 2022), p. L042201. DOI: 10.1103/PhysRevMaterials.6.L042201. URL: https://link.aps.org/doi/10.1103/PhysRevMaterials.6.L042201.

[57] V. Ivády et al. “Ab Initio Theory of the Negatively Charged Boron Vacancy Qubit in Hexagonal Boron Nitride”. In: *npj Computational Materials* 6 (2020), p. 41. DOI: 10.1038/s41524-020-0310-9. URL: https://doi.org/10.1038/s41524-020-0310-9.

[58] Mehdi Abdi et al. “Color Centers in Hexagonal Boron Nitride Monolayers: A Group Theory and Ab Initio Analysis”. In: *ACS Photonics* 5.5 (2018), pp. 1967–1976. DOI: 10.1021/acsphotonics.7b01442. URL: https://doi.org/10.1021/acsphotonics.7b01442.

[59] Asif Sajid et al. “Edge Effects on Optically Detected Magnetic Resonance of Vacancy Defects in Hexagonal Boron Nitride”. In: *Communications Physics* 3 (2020), p. 153. DOI: 10.1038/s42005-020-00416-1. URL: https://doi.org/10.1038/s42005-020-00416-1.

[60] Y. Chen and S. Y. Quek. "Photophysical Characteristics of Boron Vacancy-Derived Defect Centers in Hexagonal Boron Nitride". In: *The Journal of Physical Chemistry C* 125.38 (2021), pp. 21791–21802. DOI: 10.1021/acs.jpcc.1c05108. URL: https://doi.org/10.1021/acs.jpcc.1c05108.

[61] Feng Wu et al. "First-principles engineering of charged defects for two-dimensional quantum technologies". In: *Physical Review Materials* 1 (7 2017), pp. 1–6. ISSN: 24759953. DOI: 10.1103/PhysRevMaterials.1.071001.

[62] A. Sajid, Jeffrey R. Reimers, and Michael J. Ford. "Defect states in hexagonal boron nitride: Assignments of observed properties and prediction of properties relevant to quantum computation". In: *Phys. Rev. B* 97 (6 Feb. 2018), p. 064101. DOI: 10.1103/PhysRevB.97.064101. URL: https://link.aps.org/doi/10.1103/PhysRevB.97.064101.

[63] T. Taniguchi and K. Watanabe. "Synthesis of high-purity boron nitride single crystals under high pressure by using Ba–BN solvent". In: *Journal of Crystal Growth* 303.2 (2007), pp. 525–529. DOI: 10.1016/j.jcrysgro.2006.12.140.

[64] O. L. Krivanek et al. "Atom-by-atom structural and chemical analysis by annular dark-field electron microscopy". In: *Nature* 464.7288 (2010), pp. 571–574. DOI: 10.1038/nature08879.

[65] Tsz Wing Tang et al. "Structured-Defect Engineering of Hexagonal Boron Nitride for Identified Visible Single-Photon Emitters". In: *ACS Nano* 19.9 (2025), pp. 8509–8519. DOI: 10.1021/acsnano.4c11413. URL: https://doi.org/10.1021/acsnano.4c11413.

[66] J. Sun et al. "Recent progress in the tailored growth of two-dimensional hexagonal boron nitride via chemical vapour deposition". In: *Chemical Society Reviews* 47.12 (2018), pp. 4242–4258. DOI: 10.1039/C7CS00821E.

[67] Y. Zhou et al. "Formation energies and transition levels of carbon-related defects in hexagonal boron nitride". In: *Physical Review B* 97.21 (2018), p. 214104. DOI: 10.1103/PhysRevB.97.214104.

[68] Gunn Kim, Hyoung Joon Choi, and Seung-Hoon Jhi. "First-principles study of substitutional carbon pair and Stone–Wales defect complexes in boron nitride nanotubes". In: *arXiv preprint arXiv:1112.6319* (2011). URL: https://arxiv.org/abs/1112.6319.

[69] H. Hamdi, A. Belabbes, and A. Schleife. "Stone–Wales defects in hexagonal boron nitride as ultraviolet emitters". In: *arXiv preprint arXiv:2008.06857* (2020). URL: https://arxiv.org/abs/2008.06857.

[70] Ashley L. Gibb et al. "Atomic Resolution Imaging of Grain Boundary Defects in Monolayer CVD-Grown Hexagonal Boron Nitride". In: *Journal of the American Chemical Society* 135.18 (2013), pp. 6758–6761. DOI: 10.1021/ja401675g.

[71] Mark Fox. *Quantum Optics: An Introduction*. 1st. Oxford Master Series in Physics. Oxford: Oxford University Press, 2006. ISBN: 978-0198566733.

[72] Rodney Loudon. *The Quantum Theory of Light*. 3rd. Oxford: Oxford University Press, 2000. ISBN: 978-0198501772.

[73] Brahim Lounis and Michel Orrit. "Single-photon sources". In: *Reports on Progress in Physics* 68.5 (Apr. 2005), p. 1129. DOI: 10.1088/0034-4885/68/5/R04. URL: https://dx.doi.org/10.1088/0034-4885/68/5/R04.

[74] Carlos F. D. Faurby et al. "Purifying Photon Indistinguishability through Quantum Interference". In: *Phys. Rev. Lett.* 133 (3 2024), p. 033604. DOI: 10.1103/PhysRevLett.133.033604. URL: https://link.aps.org/doi/10.1103/PhysRevLett.133.033604.

[75] F. W. Sun and C. W. Wong. "Indistinguishability of independent single photons". In: *Phys. Rev. A* 79 (1 2009), p. 013824. DOI: 10.1103/PhysRevA.79.013824. URL: https://link.aps.org/doi/10.1103/PhysRevA.79.013824.

[76] Toan Tran et al. "Quantum emission from hexagonal boron nitride monolayers". In: *Nature Nanotechnology* 11 (2016), pp. 37–41. DOI: 10.1038/nnano.2015.242. URL: https://doi.org/10.1038/nnano.2015.242.

[77] A. Dietrich et al. "Observation of Fourier transform limited lines in hexagonal boron nitride". In: *Phys. Rev. B* 98 (8 2018), p. 081414. DOI: 10.1103/PhysRevB.98.081414. URL: https://link.aps.org/doi/10.1103/PhysRevB.98.081414.

[78] Gabriele Grosso et al. "Tunable and high-purity room temperature single-photon emission from atomic defects in hexagonal boron nitride". In: *Nature Communications* 8 (1 2017), pp. 1–8. ISSN: 20411723. DOI: 10.1038/s41467-017-00810-2. URL: http://dx.doi.org/10.1038/s41467-017-00810-2.

[79] Simon J. U. White et al. "Electrical control of quantum emitters in a Van der Waals heterostructure". In: *Light: Science & Applications* 11.1 (2022), p. 186. DOI: 10.1038/s41377-022-00877-7. URL: https://doi.org/10.1038/s41377-022-00877-7.

[80] Toan Trong Tran et al. “Quantum Emission from Defects in Single-Crystalline Hexagonal Boron Nitride”. In: *Phys. Rev. Appl.* 5 (3 2016), p. 034005. DOI: 10.1103/PhysRevApplied.5.034005. URL: https://link.aps.org/doi/10.1103/PhysRevApplied.5.034005.

[81] Gyungmok Noh et al. “Electron-Beam-Induced Emission Control of Quantum Emitters in Hexagonal Boron Nitride”. In: *Nano Letters* 22.10 (2022), pp. 4052–4059. DOI: 10.1021/acs.nanolett.2c00266. URL: https://doi.org/10.1021/acs.nanolett.2c00266.

[82] Laura J. Martínez et al. “Spatial and spectral instabilities of quantum emitters in hexagonal boron nitride”. In: *ACS Nano* 16.5 (2022), pp. 6952–6961. DOI: 10.1021/acsnano.2c00111. URL: https://doi.org/10.1021/acsnano.2c00111.

[83] Madhava Krishna Prasad et al. “Charge Transfer and Quantum Emitters in Two-Dimensional Heterostructures: An Ab Initio Study”. In: *AIP Conference Proceedings*. Vol. 2743. AIP Publishing, 2023, p. 020004. DOI: 10.1063/5.0131961. URL: https://doi.org/10.1063/5.0131961.

[84] Zai-Quan Xu et al. “Charge and energy transfer of quantum emitters in 2D heterostructures”. In: *2D Materials* 7.3 (Apr. 2020), p. 031001. DOI: 10.1088/2053-1583/ab7fc3. URL: https://dx.doi.org/10.1088/2053-1583/ab7fc3.

[85] L. J. Martínez et al. “Efficient single photon emission from a high-purity hexagonal boron nitride crystal”. In: *Phys. Rev. B* 94 (12 2016), p. 121405. DOI: 10.1103/PhysRevB.94.121405. URL: https://link.aps.org/doi/10.1103/PhysRevB.94.121405.

[86] Igor Aharonovich, Dirk Englund, and Milos Toth. “Solid-state single-photon emitters”. In: *Nature Photonics* 10 (2016), pp. 631–641. DOI: 10.1038/nphoton.2016.186. URL: https://doi.org/10.1038/nphoton.2016.186.

[87] Samco International. *Part2– What is the Bosch Process (Deep Reactive Ion Etching)?* Online tutorial. Accessed July2025. 2024. URL: https://www.samcointl.com/news-events/tutorials/what-is-the-bosch-process/.

[88] Yusai Wakafuji et al. “3D Manipulation of 2D Materials Using Microdome Polymer”. In: *Nano Letters* 20 (4 2020), pp. 2486–2492. ISSN: 15306992. DOI: 10.1021/acs.nanolett.9b05228.

[89] Stefan Pfleging. “Fabrication of Quantum Emitters in Hexagonal Boron Nitride and their Electric Field Tuning in Stacked Sample Architectures”. MA thesis. Karlsruhe Institute of Technology, 2022.

[90] Cheng Wang et al. “Hexagonal Boron Nitride Nanomaterials for Biomedical Applications”. In: *Bioengineering & Translational Medicine* 9.1 (2024), e12068. DOI: 10.1002/btm2.12068. URL: https://doi.org/10.1002/btm2.12068.

[91] Kuan Zhang and Marino Arroyo. “Understanding and strain-engineering wrinkle networks in supported graphene through simulations”. In: *Journal of the Mechanics and Physics of Solids* 72 (2014), pp. 61–74. ISSN: 0022-5096. DOI: https://doi.org/10.1016/j.jmps.2014.07.012. URL: https://www.sciencedirect.com/science/article/pii/S0022509614001501.

[92] G. Ling et al. “Prolonged photostability in hexagonal boron nitride quantum emitters”. In: *Nature Communications* 14 (2023). Demonstrates photostability only after annealing at 850°C, p. 3210. DOI: 10.1038/s43246-023-00345-8.

[93] Aslı Çakan et al. “Quantum Applications of Hexagonal Boron Nitride”. In: *arXiv preprint arXiv:2410.07712* (2024). URL: https://arxiv.org/abs/2410.07712.

[94] Rachael Klaiss et al. “Uncovering the morphological effects of high-energy Ga^+ focused ion beam milling on hBN single-photon emitter fabrication”. In: *The Journal of Chemical Physics* 157.7 (2022), p. 074703. DOI: 10.1063/5.0097581. URL: https://doi.org/10.1063/5.0097581.

[95] Chao Lyu et al. “Single-photon emission from two-dimensional hexagonal boron nitride annealed in a carbon-rich environment”. In: *Applied Physics Letters* 117.24 (2020), p. 244002. DOI: 10.1063/5.0025792. URL: https://doi.org/10.1063/5.0025792.

[96] S. X. Li et al. “Prolonged photostability in hexagonal boron nitride quantum emitters”. In: *Communications Materials* 4.1 (2023), p. 19. DOI: 10.1038/s43246-023-00345-8. URL: https://doi.org/10.1038/s43246-023-00345-8.

[97] Cameron J. Shearer et al. “Accurate thickness measurement of graphene”. In: *Nanotechnology* 27.12 (2016), p. 125704. DOI: 10.1088/0957-4484/27/12/125704.

[98] Kaiyue Wang et al. “Annealing and lateral migration of defects in IIa diamond created by near-threshold electron irradiation”. In: *Applied Physics Letters* 110.15 (2017), p. 152101. DOI: 10.1063/1.4980017. URL: https://doi.org/10.1063/1.4980017.

[99] Xiaohui Xu et al. “Creating Quantum Emitters in Hexagonal Boron Nitride Deterministically on Chip-Compatible Substrates”. In: *Nano Letters* 21 (19 2021), pp. 8182–8189. ISSN: 15306992. DOI: 10.1021/acs.nanolett.1c02640.

[100] Niclas Lindvall, Alexey Kalabukhov, and August Yurgens. "Cleaning graphene using atomic force microscope". In: *Journal of Applied Physics* 111 (6 2012), p. 064904. ISSN: 00218979. DOI: 10.1063/1.3695451.

[101] Yongliang Chen et al. "Generation of High-Density Quantum Emitters in High-Quality, Exfoliated Hexagonal Boron Nitride". In: *ACS Applied Materials & Interfaces* 13 (39 Oct. 2021), pp. 47283–47292. ISSN: 1944-8244. DOI: 10.1021/acsami.1c14863.

[102] Achint Jain et al. "Minimizing residues and strain in 2D materials transferred from PDMS". In: *Nanotechnology* 29 (26 June 2018), p. 265203. ISSN: 0957-4484. DOI: 10.1088/1361-6528/aabd90.

[103] A. M. Goossens et al. "Mechanical cleaning of graphene". In: *Applied Physics Letters* 100 (7 Feb. 2012). ISSN: 0003-6951. DOI: 10.1063/1.3685504.

[104] N. Khan, J. Li, and J. H. Edgar. "The thermal oxidation of hexagonal boron nitride single crystals: Dry and ambient air compared". In: *MRS Communications* 12 (1 Feb. 2022), pp. 74–82. ISSN: 21596867. DOI: 10.1557/s43579-021-00143-8.

[105] Philipp Valerius et al. "Annealing of ion-irradiated hexagonal boron nitride on Ir(111)". In: *Phys. Rev. B* 96 (23 2017), p. 235410. DOI: 10.1103/PhysRevB.96.235410. URL: https://link.aps.org/doi/10.1103/PhysRevB.96.235410.

[106] Guocheng Zhang, Yufang Chang, and Bin Yan. "The Study of the Wrinkles of Hexagonal Boron-Nitride Flake after the Annealing". In: *Crystals* 13.2 (2023). ISSN: 2073-4352. DOI: 10.3390/cryst13020304. URL: https://www.mdpi.com/2073-4352/13/2/304.

[107] Md Samiul Islam et al. "Large-Scale Statistical Analysis of Defect Emission in hBN: Revealing Spectral Families and Influence of Flake Morphology". In: *ACS Nano* 18.32 (2024). PMID: 39083640, pp. 20980–20989. DOI: 10.1021/acsnano.3c10403. eprint: https://doi.org/10.1021/acsnano.3c10403. URL: https://doi.org/10.1021/acsnano.3c10403.

[108] Yongliang Chen et al. "Annealing of blue quantum emitters in carbon-doped hexagonal boron nitride". In: *Applied Physics Letters* 123 (4 July 2023), p. 041902. ISSN: 0003-6951. DOI: 10.1063/5.0155311.

[109] A. Zobelli et al. "Vacancy migration in hexagonal boron nitride". In: *Physical Review B - Condensed Matter and Materials Physics* 75 (9 Mar. 2007). ISSN: 10980121. DOI: 10.1103/PhysRevB.75.094104.

[110] Toan Trong Tran et al. "Resonant Excitation of Quantum Emitters in Hexagonal Boron Nitride". In: *ACS Photonics* 5 (2 2018), pp. 295–300. ISSN: 23304022. DOI: 10.1021/acsphotonics.7b00977.

[111] Noah Mendelson et al. "Strain-Induced Modification of the Optical Characteristics of Quantum Emitters in Hexagonal Boron Nitride". In: *Advanced Materials* 32 (21 2020), pp. 1–9. ISSN: 15214095. DOI: 10.1002/adma.201908316.

[112] Chi Li et al. "Purification of single-photon emission from hBN using post-processing treatments". In: *Nanophotonics* 8 (11 2019), pp. 2049–2055. ISSN: 21928614. DOI: 10.1515/nanoph-2019-0099.

[113] Nicholas R. Jungwirth et al. "Temperature Dependence of Wavelength Selectable Zero-Phonon Emission from Single Defects in Hexagonal Boron Nitride". In: *Nano Letters* 16 (10 2016), pp. 6052–6057. ISSN: 15306992. DOI: 10.1021/acs.nanolett.6b01987.

[114] Marek Maciaszek, Lukas Razinkovas, and Audrius Alkauskas. "Thermodynamics of carbon point defects in hexagonal boron nitride". In: *Phys. Rev. Mater.* 6 (1 2022), p. 014005. DOI: 10.1103/PhysRevMaterials.6.014005. URL: https://link.aps.org/doi/10.1103/PhysRevMaterials.6.014005.

[115] Chao Lyu et al. "Single-photon emission from two-dimensional hexagonal boron nitride annealed in a carbon-rich environment". In: *Applied Physics Letters* 117 (24 2020), p. 244002. ISSN: 0003-6951. DOI: 10.1063/5.0025792.

[116] Michael Winter et al. "Photoluminescent properties of the carbon-dimer defect in hexagonal boron-nitride: A many-body finite-size cluster approach". In: *Physical Review Materials* 5 (9 2021), pp. 1–12. ISSN: 24759953. DOI: 10.1103/PhysRevMaterials.5.095201.

[117] Maximilian Pallmann et al. "Cavity-Mediated Collective Emission from Few Emitters in a Diamond Membrane". In: *Phys. Rev. X* 14 (4 2024), p. 041055. DOI: 10.1103/PhysRevX.14.041055. URL: https://link.aps.org/doi/10.1103/PhysRevX.14.041055.

[118] Qixing Wang et al. "Photoluminescence Upconversion by Defects in Hexagonal Boron Nitride". In: *Nano Letters* 18 (11 Nov. 2018), pp. 6898–6905. ISSN: 15306992. DOI: 10.1021/acs.nanolett.8b02804.

[119] Cesar Jara et al. "First-principles identification of single photon emitters based on carbon clusters in hexagonal boron nitride". In: *Journal of Physical Chemistry A* 125 (6 Feb. 2021), pp. 1325–1335. ISSN: 15205215. DOI: 10.1021/acs.jpca.0c07339.

[120] F. Wu, D. Rocca, and Y. Ping. "Dimensionality and Anisotropy Dependence of Radiative Recombination in Nanostructured Phosphorene". In: *Journal of Materials Chemistry C* 7.41 (2019), pp. 12891–12899. DOI: 10.1039/C9TC04289E.

[121] M. Palummo, M. Bernardi, and J. C. Grossman. "Exciton Radiative Lifetimes in Two-Dimensional Transition Metal Dichalcogenides". In: *Nano Letters* 15.5 (2015), pp. 2794–2800. DOI: 10.1021/nl503799t.

[122] A. Alkauskas, Q. Yan, and C. G. Van de Walle. "First-principles theory of nonradiative carrier capture via multiphonon emission". In: *Physical Review B* 90.7 (2014), p. 075202. DOI: 10.1103/PhysRevB.90.075202.

[123] F. Wu et al. "Carrier recombination mechanism at defects in wide band gap two-dimensional materials from first principles". In: *Physical Review B* 100.8 (2019), p. 081407. DOI: 10.1103/PhysRevB.100.081407.

[124] Mark E. Turiansky and Chris G. Van de Walle. "Impact of dangling bonds on properties of h-BN". In: *2D Materials* 8.2 (2021), p. 024002. DOI: 10.1088/2053-1583/abe4bb.

[125] Lukas Novotny and Bert Hecht. *Principles of Nano-Optics*. Cambridge, UK: Cambridge University Press, 2012. ISBN: 978-0521192270.

[126] Patrick Lawes et al. "Hierarchical Self-Assembly and Conformation of Tb Double-Decker Molecular Magnets: Experiment and Molecular Dynamics". In: *Nanomaterials* 13.15 (2023), p. 2232. DOI: 10.3390/nano13152232. URL: https://doi.org/10.3390/nano13152232.

[127] Zhitao Deng et al. "Self-assembly of bis(phthalocyaninato)terbium on metal surfaces". In: *Physica Scripta* 90 (9 Sept. 2015). ISSN: 14024896. DOI: 10.1088/0031-8949/90/9/098003.

[128] Manuel Lopes et al. "Surface-enhanced raman signal for terbium single-molecule magnets grafted on graphene". In: *ACS Nano* 4 (12 2010), pp. 7531–7537. ISSN: 19360851. DOI: 10.1021/nn1018363.

[129] Vaibhav Varade et al. "Chiral Light Emission from a Hybrid Magnetic Molecule-Monolayer Transition Metal Dichalcogenide Heterostructure". In: *ACS Nano* 17 (3 Feb. 2023), pp. 2170–2181. ISSN: 1936086X. DOI: 10.1021/acsnano.2c08320.

[130] Riccardo Marin, Gabriel Brunet, and Muralee Murugesu. "Shining New Light on Multifunctional Lanthanide Single-Molecule Magnets". In: *Angewandte Chemie - International Edition* 60 (4 2021), pp. 1728–1746. ISSN: 15213773. DOI: 10.1002/anie.201910299.

[131] Kazuyuki Ishii. *Functional singlet oxygen generators based on phthalocyanines*. Aug. 2012. DOI: 10.1016/j.ccr.2012.03.022.

[132] Anand Kumar et al. "Polarization Dynamics of Solid-State Quantum Emitters". In: *ACS Nano* 18.7 (2024). Open Access, published February 9, 2024, pp. 5270–5281. ISSN: 1936-0851. DOI: 10.1021/acsnano.3c08940.

[133] Alexander Kubanek. "Coherent quantum emitters in hexagonal boron nitride". In: *Advanced Quantum Technologies* 5.9 (2022), p. 2200009. DOI: 10.1002/qute.202200009.

[134] Toan Trong Tran et al. "Resonant Excitation of Quantum Emitters in Hexagonal Boron Nitride". In: *ACS Photonics* 5.2 (2018), pp. 295–300. DOI: 10.1021/acsphotonics.7b00977. URL: https://doi.org/10.1021/acsphotonics.7b00977.

[135] Ioannis Karapatzakis. "Microwave Control of the Tin-Vacancy Spin Qubit in Diamond with a Superconducting Waveguide". PhD thesis. Karlsruhe Institute of Technology, 2025.

[136] Zhizhan Qiu et al. "Atomic and Electronic Structure of Defects in hBN: Enhancing Single-Defect Functionalities". In: *ACS Nano* 18 (35 Sept. 2024), pp. 24035–24043. ISSN: 1936086X. DOI: 10.1021/acsnano.4c03640.

[137] Dillon Wong et al. "Characterization and manipulation of individual defects in insulating hexagonal boron nitride using scanning tunnelling microscopy". In: *Nature Nanotechnology* 10 (11 2015), pp. 949–953. ISSN: 17483395. DOI: 10.1038/nnano.2015.188. URL: http://dx.doi.org/10.1038/nnano.2015.188.

[138] Sandro Stamenkovic. *3D Manipulation of 2D Materials Using h-BN for Creating Quantum Emitters*. 2023.

[139] F. Hahl. "Developing a confocal microscope for characterizing quantum emitters as sensors for magnetic field using the Nitrogen-Vacancy Center in nanodiamonds". Master's thesis. Karlsruhe Institute of Technology, 2018.

[140] A. Zilz. "Investigation of the rarefied gas flow in the pumping tube of a ^{3}He/^{4}He dilution refrigerator". Master's thesis. Karlsruhe Institute of Technology, 2022.

[141] J. Schaal. "Fabrication and characterization of superconducting coplanar waveguides for spin qubit control in diamond". Master's thesis. Karlsruhe Institute of Technology, 2024.

A. Appendix

A.1. Recipes for obtaining hBN samples

Cleaning and exfoliation steps

✓ **Chip Dicing**

- Dice a 2-inch intrinsic silicon wafer into 5 mm × 5 mm square chips. The wafer has a thickness of 500 µm and is coated with a 300 nm thermal oxide layer.

✓ **Alcohol Cleaning**

- Place the diced chips in boiling acetone at 90 °C for 6 minutes, followed by 2 minutes of ultrasonication.
- Transfer the chips into clean, cold acetone, rinse with isopropanol (IPA), and blow dry using nitrogen (N_2).

✓ **Plasma Cleaning**

- Perform weak plasma cleaning using 12.5 ml/min O_2 for 5 minutes. Pre-clean the plasma chamber with maximum power and oxygen before use.
- Heat the chips on a hotplate at 200 °C to eliminate dangling bonds, thus preventing charge traps that could alter the local electric field or induce strain in the hBN.
- While the chips are on the hotplate, cleave hBN crystals (from powder) several times using adhesive tape. Final exfoliation is performed directly onto the warm chip surface.

✓ **Exfoliation**

- Remove the chip from the hotplate. Immediately press the exfoliated tape onto the chip with uniform pressure and moderate force, then peel off the tape to complete the exfoliation.

Patterning holes into Si/SiO_2

✓ **Resist Deposition**

- Spin-coat AZ5214-E: 75 s at 6000 $r.min^{-1}$ with 500 $r.min^{-2}$ acceleration (final thickness: 1500 nm).
- Soft-bake (anneal) for 1 min 40 s at 100 °C.

✓ **Optical Lithography**

- Light intensity: 13
- Exposure time: 5 s
- Wafer Edge Control (WEC) distance: 45 µm

✓ **Development**

- Develop in MIF 726 for 40 s

✓ **Reactive Ion Etching (RIE)**

- Perform 5 BOSCH cycles with alternating SF_6 and C_4F_8 gases to achieve a depth of 2–3 µm.

✓ **Lift-Off**

- Immerse in NEP remover at 90 °C for 4 hrs.
- Ultrasonic bath: 10 s at 20 % power.
- Rinse with double-distilled water and dry with N_2 gas.

PDMS microdome and dry transfer

✓ **PDMS Microdome**

- Mix the base and curing agent of Sylgard 184 Silicone Elastomer in a 10:1 ratio thoroughly.
- Using a toothpick, form small droplets of the polymer mixture on one end of a glass slide. centre a copper wire (ø= 220 µm) and a tungsten needle (ø= 200 nm) vertically on each droplet.
- Cure each droplet at 150 °C for 10 minutes. This forms a Polydimethylsiloxane (PDMS) stamp with a microdome shape.

✓ **Flake Transfer**

- Wrap a clean PVC film over the PDMS microdome, pressing out any trapped air bubbles to ensure good surface contact. Clean the PVC surface with IPA.
- As illustrated in Figure 3.6, pick up the flake at 70 °C and drop it onto the target substrate at 120 °C.

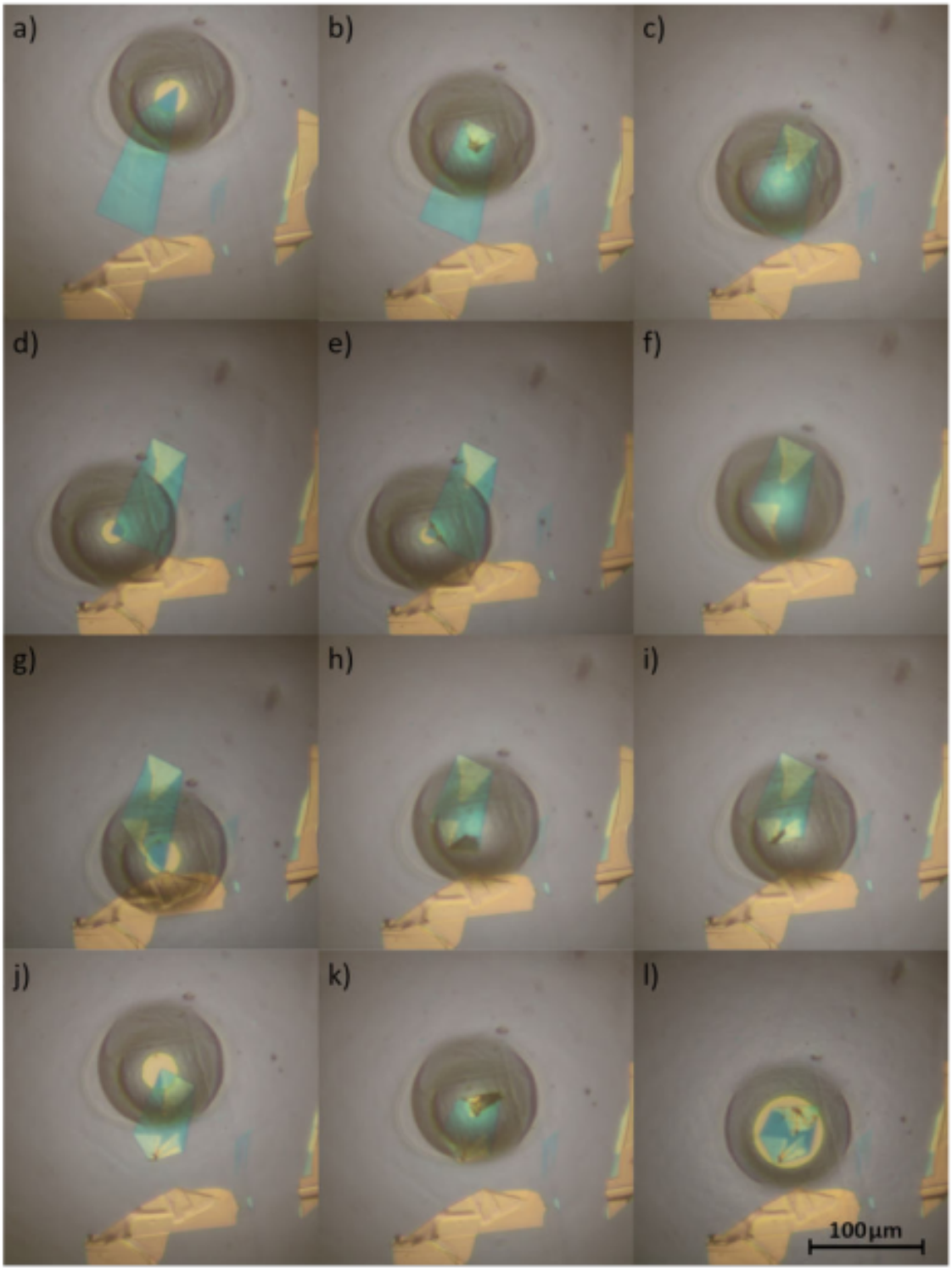

Figure A.1.: Folding operation: images (a)-(c) show first fold. Images (d)-(f) show second fold. Images (g)-(i) show third fold. Images (j)-(k) show fourth fold. Image (l) shows flake pick-up [138].

AFM nanoindentation

✓Characterize flake prior to indentation

- Scan the preselected flake in tapping mode to confirm a thickness between 40 nm and 100 nm, and ensure a clean surface topography.
  Tip used: *HQ:NSC15/Al BS* (8 nm tip, $k = 40$ N/m)

- If only minimal debris is present and no bubbles are visible, select regions for indentation. If necessary, perform contact-mode cleaning after changing the tip.
  Tip used: *Multi75DLC* (15 nm tip, $k = 3$ N/m)

✓Indentation

- Replace with the indentation tip. Scan the desired area and activate the *Point and Shoot* function to assign an array of marker points, where individual force curves will be executed. This can be performed in both tapping and contact modes. Use the *Engage* command to bring the tip into controlled contact with the flake; indentation is carried out in *relative displacement* mode.
  Parameters: trigger voltage = 1.6 V; dwell time = 2 s; Retract delay= 2s; spacing = 1.5 µm
  Tip used: *Tap300DLC* (15 nm tip, $k = 40$ N/m)

- Confirm indent size and position using a high-resolution tip.
  Tip used: *Hi'Res-C15/Cr-Au* (1 nm tip, $k = 40$ N/m)

CPW

✓**Spin Coating**

- 2-inch wafer, AZ5214-E single coat
- Approx. 1.5 µm thick resist coat

✓**Optical Lithography**

- Light intensity: 13
- 5 s exposure
- 50 µm WEC (Wafer Edge Control) distance

✓**Development**

- MIF 726 developer for 40 s

✓**Metallisation**

- Kaufmann cleaning with Ar:O_2 = 9:1
- Titanium wetting layer:5 nm, 0.1 nm/s, 65 mA
- Platinum 40 nm, rate of deposition: 0.14 nm/s, 235 mA

✓**Lift-off**

- NEP at 90°C

A.2. ZPL and Corresponding $g^{(2)}(\tau)$

Comparison of different SPEs and their corresponding second order correlation functions for the determination of the characteristic time. Each $g^{(2)}(\tau)$ is fit to the two level system mentioned in the main text. These are all class A emitters on the same flake. Figures A.2 and A.3 portray that despite similar emission energies, flake thickness and fabrication method, the local environment of the defect determines their lineshape and approximate lifetime. The lifetimes are not inversely proportional to the linewidth of the ZPL shown here. These are room temperature measurements where the linewidths have both homogeneous and inhomogeneous broadening.

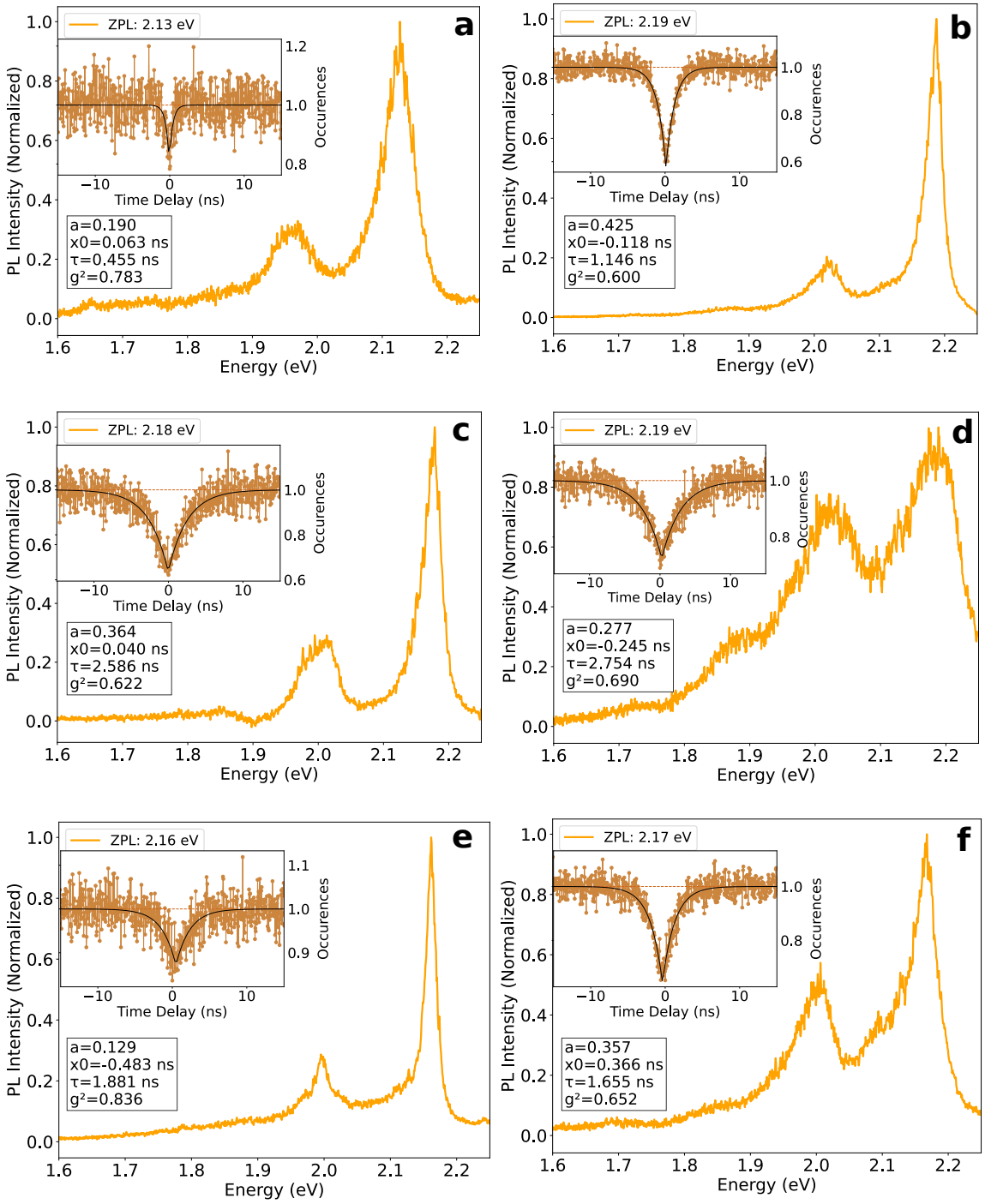

Figure A.2.: Fluorescence lineshape and $g^{(2)}(\tau)$ of class A emitter.

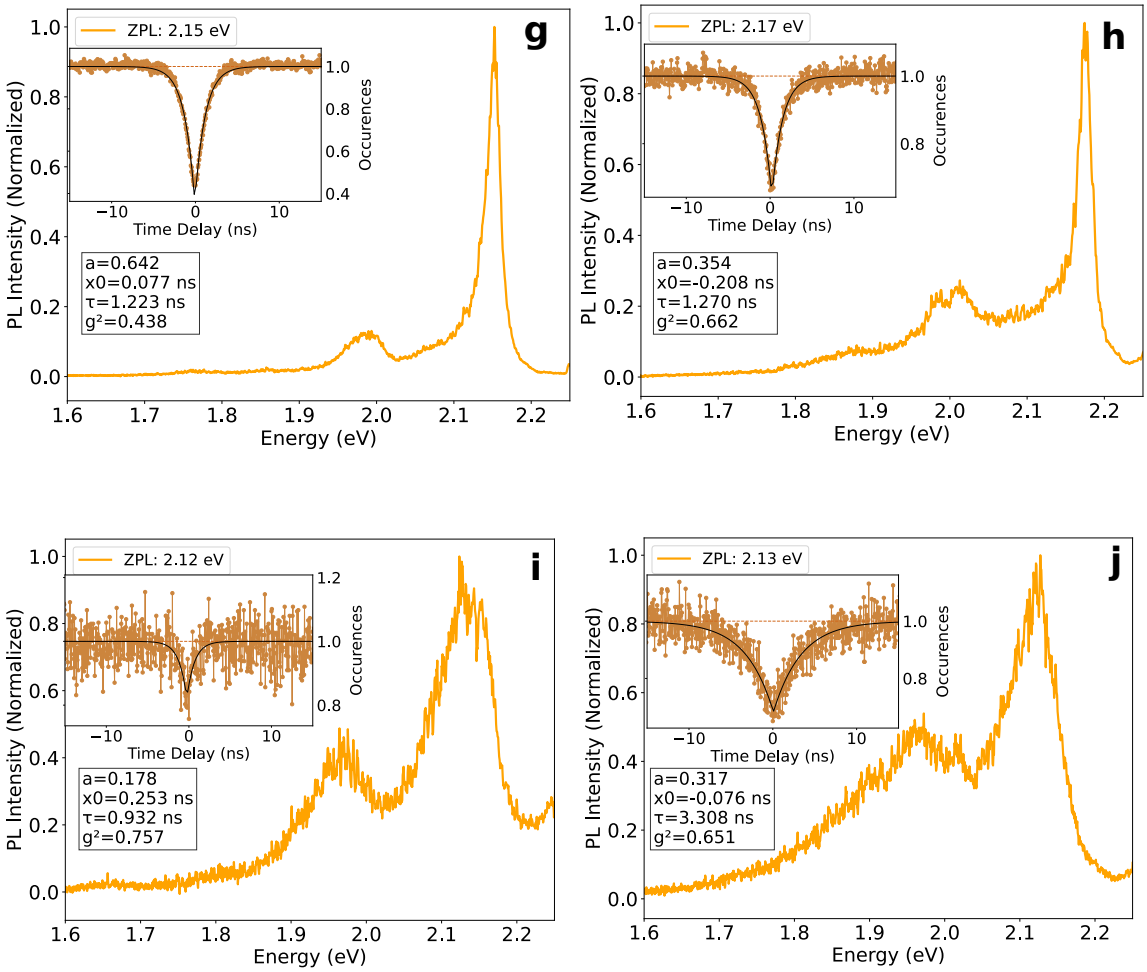

Figure A.3.: Fluorescence lineshape and $g^{(2)}(\tau)$ of class A emitter.

A.3. Fluorescence Measurements

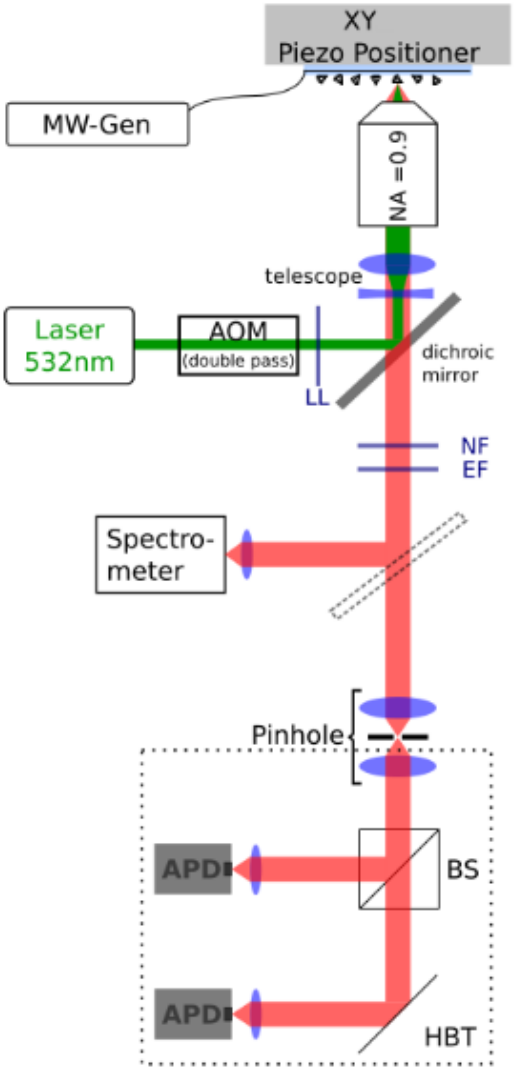

Figure A.4.: A green laser is used to optically excite the sample, which is mounted on a three-axis piezoelectric positioner for precise spatial scanning. The emitted red photoluminescence is collected through a high-numerical-aperture objective lens. To isolate the fluorescence signal, the collected light is passed through a dichroic mirror that reflects the excitation laser while transmitting the longer-wavelength emission. The confocal detection scheme involves a pinhole placed in the image plane, which blocks out-of-focus light and enhances spatial resolution by ensuring that only photons from the focal volume reach the detectors. This configuration allows for diffraction-limited optical sectioning of the sample. The filtered fluorescence is then directed either to a spectrometer for spectral analysis or to a Hanbury Brown and Twiss (HBT) interferometer, located in a light-tight enclosure (indicated by the dotted box), for photon correlation measurements. In the HBT setup, a 50/50 non-polarizing beam splitter equally divides the photoluminescence signal between two avalanche photodiodes (APDs), enabling the measurement of second-order photon correlation functions, $g^{(2)}(\tau)$, essential for identifying single-photon emission characteristics (Adapted from [139].

A.4. Molecule Deposition

Each figure corresponds to ZPL of emitters recorded in flake before and after deposition of molecules.

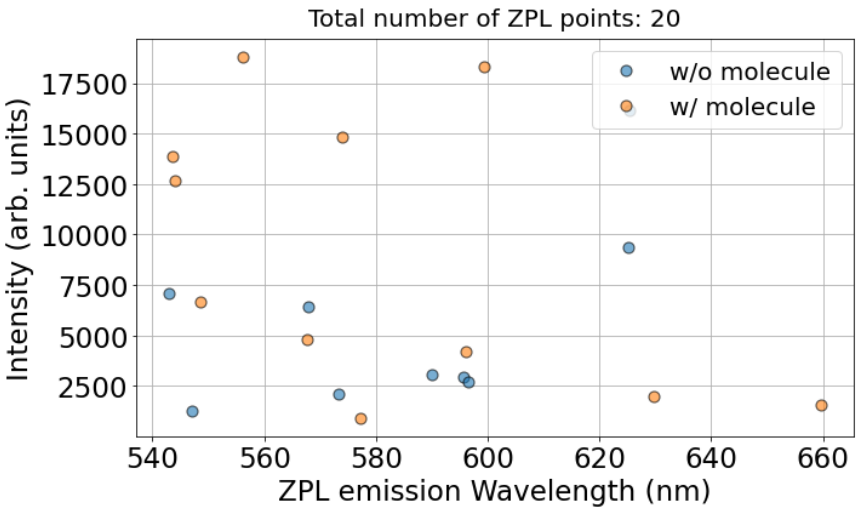

Figure A.5.: Flake#1 shows comparison of ZPL intensity and distribution of SPEs after 40 % of a monolayer evaporation of $TbPc_2$. There are more emitters with high brightness than for emitters without molecule.

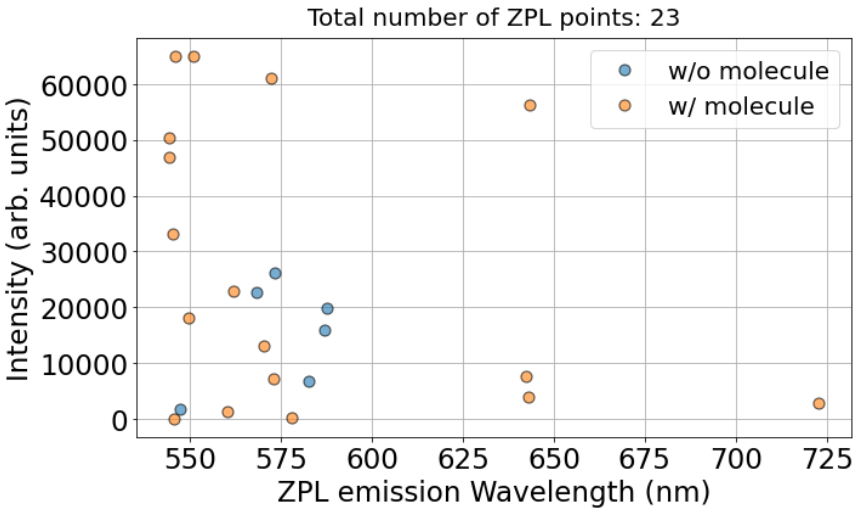

Figure A.6.: Flake 2 shows comparison of ZPL intensity and distribution of SPEs after 40 % of a monolayer of $TbPc_2$ evaporation, this is from the same set of sample as figure A.5. There are more emitters which are recorded after molecules are deposited and also evidently have higher spectral brightness after molecule deposition.

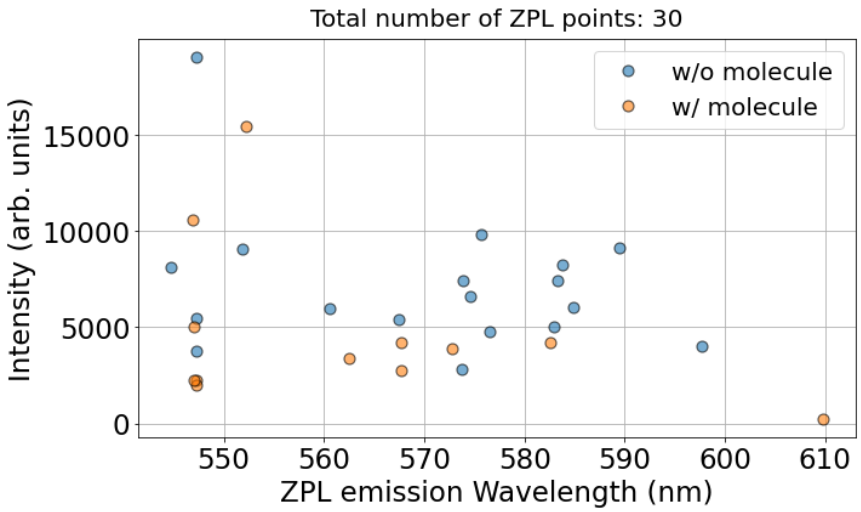

Figure A.7.: Flake 3 from the second set of evaporation with a higher coverage of 1 monolayer of molecular evaporation. Here the brightness of SPEs is not as evidently enhanced after molecular evaporation, but as mentioned in the main text, recurring spectral feature at around 680 nm consistently appears after molecule evaporation which was not there beforehand. Since only the highest ZPL for each confocal volume are shown in this distribution the some of the weaker peaks at around 680 nm are not shown in this plot.

A.5. RT ODMR

Room temperature (RT) ODMR measurements were performed using a green laser and sweeping the microwave frequency from 0.2 GHz to 3 GHz. An external magnetic field of approximately 15 mT was applied using small permanent magnets. The frequency sweeps were divided into 1 GHz segments, each with a resolution of 1 MHz. A microwave power of 40 dBm was used, and the radio frequency (RF) signal was initially delivered through a coplanar waveguide (CPW).

Measurements were conducted on several flakes, but only one emitter consistently showed an ODMR contrast that remained stable over several hours. To investigate the magnetic field dependence, the weak external magnetic field (15 mT) was rotated around the sample to observe any effect on the ODMR response. As shown in Figure A.9, a measurable ODMR contrast was observed when the magnetic field was aligned in-plane along a specific direction. Notably, during later measurements, the RF field was applied using an antenna

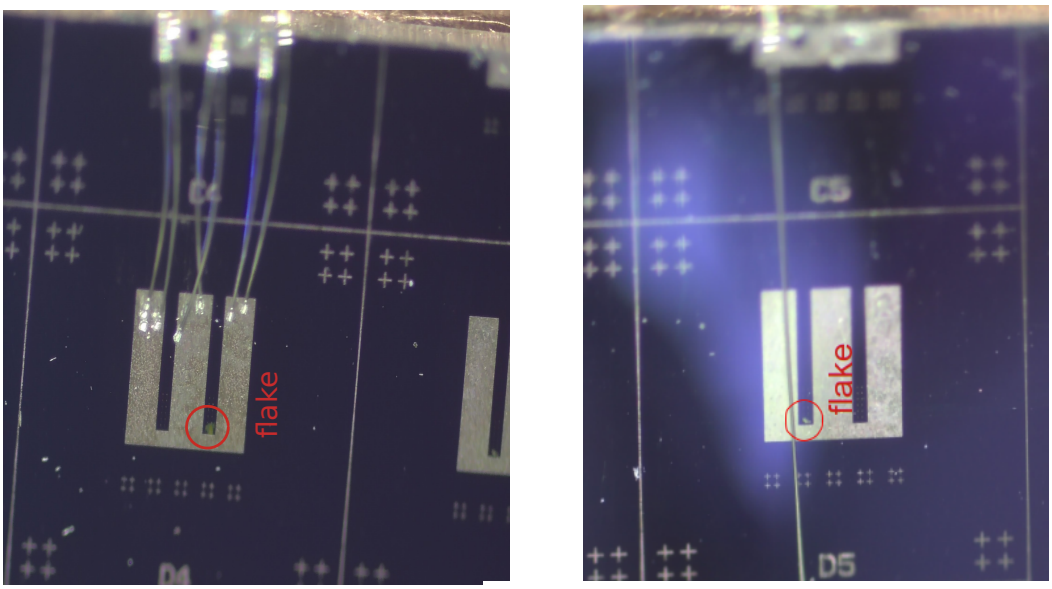

Figure A.8.: CPWs bonded for RT and LT ODMR measurements. Left shows the waveguide bonded to the the flex CPW glued to the sample holder which is the cold finger. Right shows an antennae through the waveguide because the CPW is likely destroyed from high temperature annealing. The sample on the right had emitter with RT ODMR contrast observed.

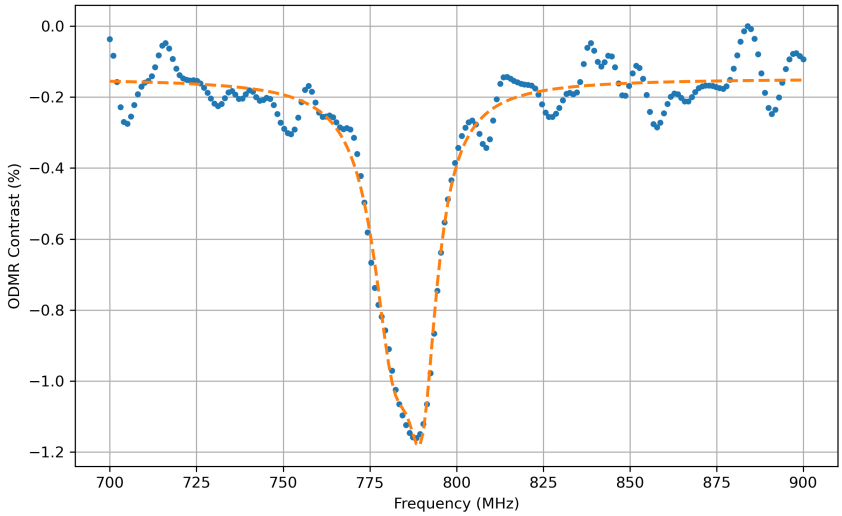

Figure A.9.: RT ODMR on an hBN emitter with ZPL around 577 nm.

instead of the CPW, as the CPW had sustained damage during the high-temperature annealing process used to activate the emitters.

A.6. Low Temperature Measurement

The low temperature measurements were conducted in a custom-built, table-top dilution refrigerator designed in an "inverted" configuration. Unlike conventional systems, this setup places the coldest stage—the millikelvin plate—at the top, enabling straightforward optical access through top-mounted windows. This design, originally developed by Alain Benoit and Wolfgang Wernsdorfer and later optimized by Marcel Schrodin to include optical integration at the mK stage, is illustrated schematically in figure A.10. The cryostat reaches base temperatures below 100 mK in under 6 hours and offers user-friendly access to internal components, including easy installation of 3D vector magnets without soldering.

The system comprises five vertically stacked thermal stages, each thermally isolated using stainless-steel supports and reflective shielding. Cooling is achieved through two closed-loop circuits: firstly, a ^{4}He pulse-tube stage for pre-cooling to 4 K, and a ^{3}He/^{4}He dilution unit for reaching sub-Kelvin temperatures. For further technical details on the principles and how the system operates please refer to [140]. The confocal setup operating with the dilution fridge has been setup and optimized by Ioannis Karapatzakis and more information on the vector magnets and the cold finger with incorporated flex-CPW (CPW) can be found in his PhD thesis [135].

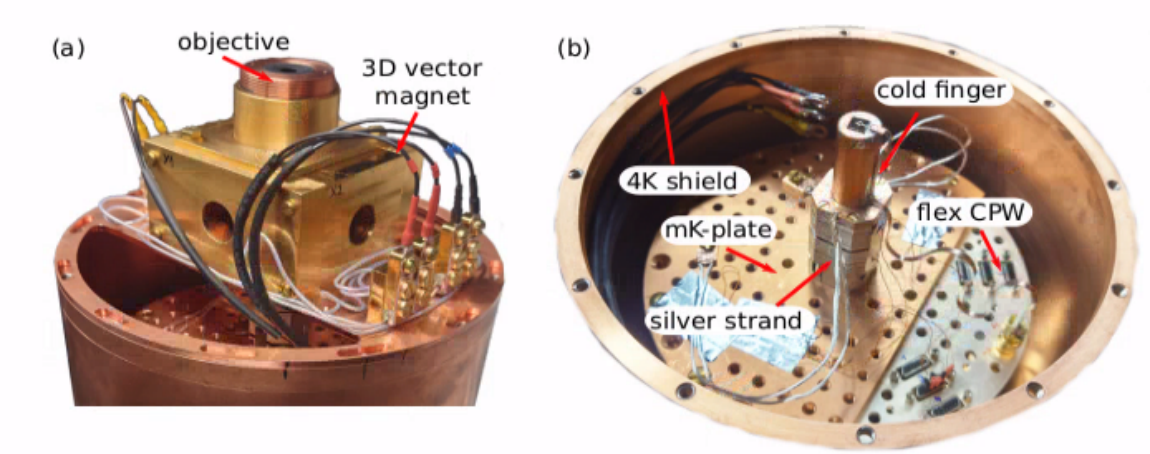

Figure A.11.: Adapted from [135]. (a) Shows the 4 K shield along with the 3D-vector magnets. (b) Presents the millikelvin plate of the cryostat. Microwaves are delivered to the sample on the cold finger via bonding wires that connect the flexible CPW to the on-chip NC-CPW/SC-CPW. The silver strands help thermalize the cold finger onto the millikelvin plate.

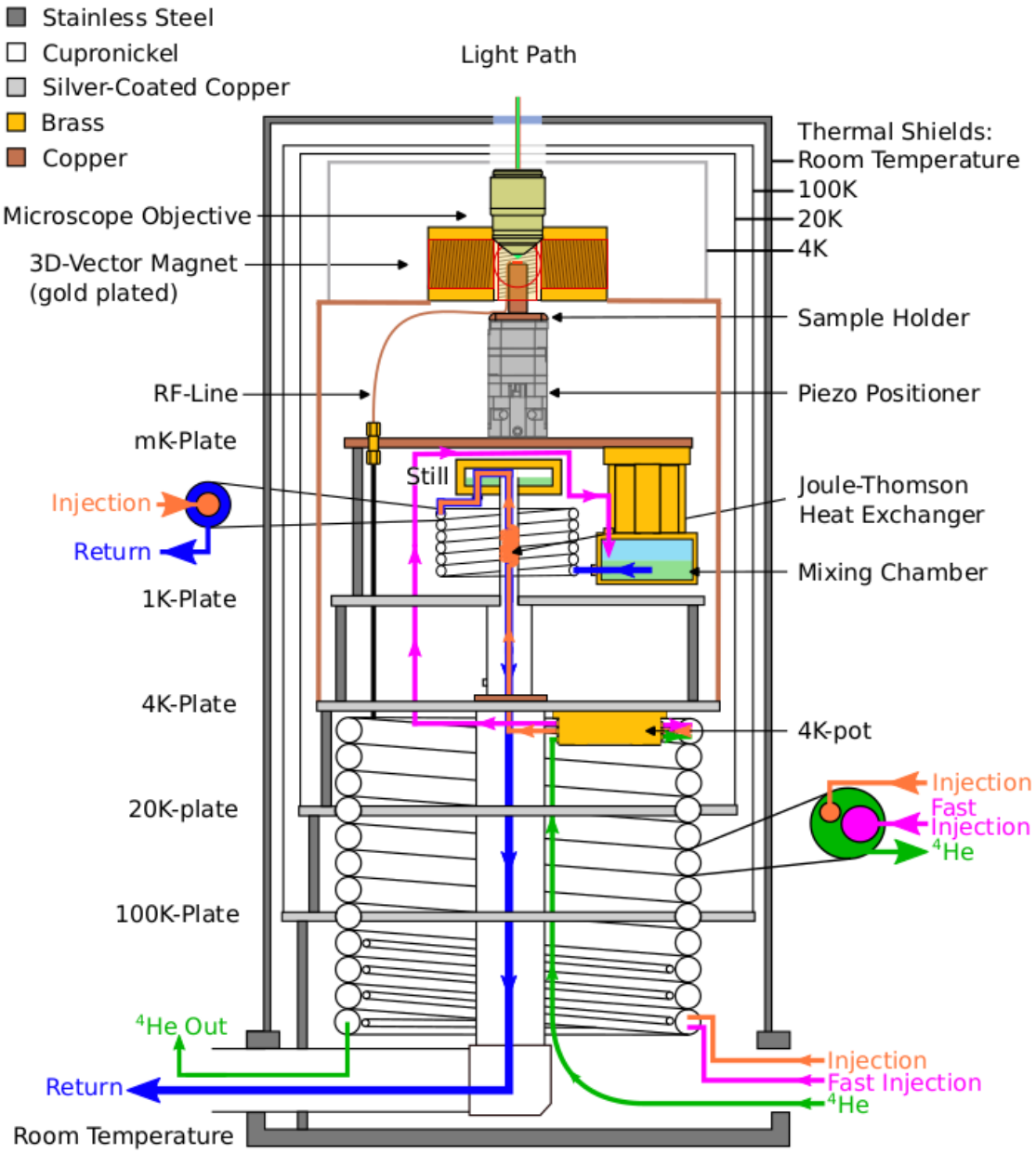

Figure A.10.: Schematic cross-section of the custom-built dilution refrigerator utilized in the experiment. The confocal optical path is introduced from the top of the apparatus, taking advantage of the inverted architecture for direct axial access. A high-numerical-aperture objective, rigidly thermally anchored to the 4 K stage, facilitates efficient photon collection while minimizing thermal load. The sample is mounted on an XYZ nanopositioning stage, enabling sub-micron spatial alignment with respect to the optical axis. The diagram delineates the hierarchical thermal architecture comprising four concentric radiation shields and five distinct temperature stages: 300 K (ambient), 100 K, 20 K, 4 K, 1 K, and the base millikelvin stage. A 3D vector magnet is integrated within the 4 K shield, which is machined from high-purity copper to ensure both mechanical rigidity and optimal thermal conductivity. Cryogenic fluid flow paths are indicated via color-coded channels: orange and magenta denote the injection and rapid injection lines of the ^{3}He/^{4}He dilution circuit, respectively, while green corresponds to the ^{4}He precooling loop. This figure is adapted from the master's thesis of Julian Schaal [141].

A.7. Laser Line

Figure A.12 shows the excitation laser at 517.3 THz used for PLE measurements. The spectrum is fitted to Gaussian and shows a linewidth of 50.59 GHz.

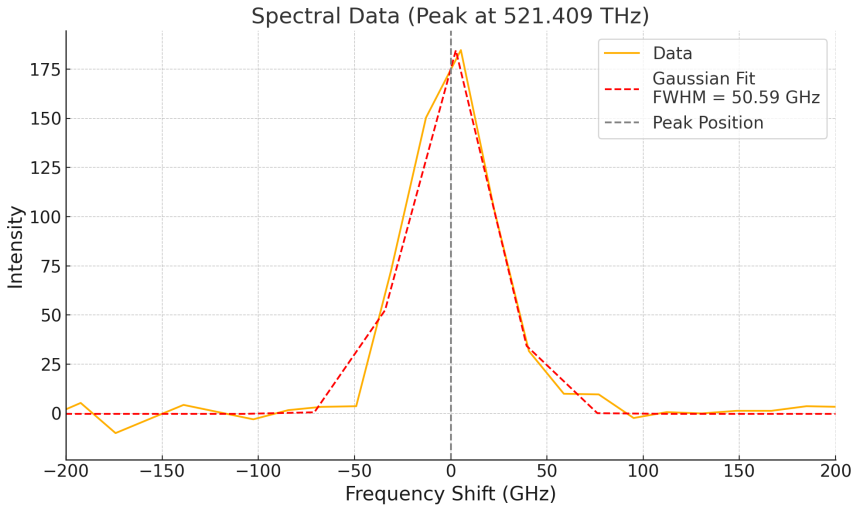

Figure A.12.: Spectral fit to the laser emission line used for resonant excitation of emitter in figure 4.33.

B. Acknowledgments

I would like to thank my supervisor Prof. Wolfgang Wernsdorfer for giving me the opportunity to work in his group under his supervision. I think the reason I could enjoy my research as much as I did, was thanks to Wolfgang's attitude towards science, in which he never restricted curiosity and encouraged us to do our science. His trust in me to allow me to have the freedom in my research work, gave me a huge sense of responsibility and motivation to push the research forward and trying to make things work, which would otherwise have not been possible. I also thank Wolfgang for teaching us to critically evaluate the soundness of our own research works. This instilled in me a healthy scientific attitude: question everything and ensure your results are irrefutable. His challenges motivated me to overcome obstacles and obtain greater efficiency. His remarkable work ethic also inspired this development. I am glad I met you as a supervisor, you have taught me to ask better questions and become a more resilient researcher.

Next, I would like to thank my second supervisor Prof. David Hunger for agreeing to be my second supervisor and always offering great insightful feedback for our optics group. Next I would like to thank Christoph Sürgers for his consistent help in helping me shape up the publication work and structure my write up. In addition, Christoph is a like a solid rock to the group, helping with anything and everything and always managing to pull out exactly what we need from one of his lab closets, much like Hermione from her bag. Thank you for being such a good sport, your strength is inspiring. I would also like to thank Prof. Philip Willke — without you, I would probably not be here. Thank you, Philip, for informing me about this Marie Curie position and, prior to that, for inviting Wolfgang to our conference at the Centre for Quantum Nanoscience (QNS) in Seoul during my time there as a master's student. You and Prof. Aparajita Singha have been role models for me since my time as an intern at QNS. I would like to thank Dr. Concepcion Molina Jiron de Moreno at institute of quantum materials and technology (IQMT) for taking the Raman data on YPc_2 and $TbPc_2$ crystals for me. I thank Richard Thelen from institute of microstructure and technology (IMT) for helpful discussions on AFM imaging and data

analysis. I thank the CFN team, especially Lucas Radtke for tending to cleanroom requests in a swift manner and being super helpful with discussions regarding fabrication.

I thank my group: simple words are not enough to express how much I like the lot of you. You are like a second family to me. The optics subgroup: thank you so much Ioannis, Luis and Jeremias for being so supportive and making the optics group work. I love how we are always there to help each other and that is the general attitude for the entire Wernsdorfer working group, former members included. Thank you Sagar, Eufemio, Thomas, Denis, Simon, Tajamul, Tim, Viktor, Lukas, Baby Daniel, Tino, Priyanchi, Sophie, Danilo and Janic for being such wonderful company and for discussions and all kinds of help. My students Lukas, Sandro and Csongor, thank you for being my students, I had the great pleasure of supervising you and learning things with you together, you were wonderful. Thank you Marcel for introducing me to the optics subgroup and Rainer for introducing me to hBN. I have learned a lot from both of you in my first years, please know that I am very grateful for your patience with me.

A very special thanks to my office mates Daniel, Luca and Appu who made me look forward to coming to work everyday. I love our banters and the motivation we try to give each other. I will really miss you guys very much, let's make sure we keep in touch, cause life might start feeling dull without all our precious enlightening banter.

I would like to thank the people I met through KSQM, especially Yu and Prof Markus Garst who made the PhD school possible. I have received a lot of help from the training sessions provided by this school as have many other peers.

I would like to thank my families in Bangladesh and in Germany for their unwavering support and encouragement. I draw immense strength simply from knowing that you exist and that you are always there for me, no matter what. It means the world to know that I can always turn to you—through both successes and the setbacks in life.

Lastly and most importantly I would like to thank you, my husband, Ekrem; for having more faith in my abilities than probably I did myself, and constantly reminding me that whatever happens it is going to be fine because we are in this together. Thank you for taking such good care of me, in all ways possible, especially in the last important phase of my PhD. I do not want to start writing a love letter here but know that you make life sweeter and I absolutely love sugar.